Leibniz-Institut für
Astrophysik Potsdam

Dynamical Modeling and Evolution of Simulated Galaxies: A Comparative Study Using Jeans Axisymmetric Models and N-Body Simulations.

A thesis submitted in partial fulfillment for the requirement of the degree of Master of Science in Astrophysics

Amrit Sedain

Universität Potsdam

Institut für Physik und Astronomie

Supervisor: Dr. Nikolay Kacharov

First Referee : Prof. Dr. Maria-Rosa Cioni

Second Referee : Dr. Martin Sparre

March 2024

STATEMENT OF DECLARATION

I thus certify that the Master's thesis I have submitted is entirely original work of mine, except the sources and materials that are listed and acknowledged to the best of my knowledge. I noted all quotes, citations, and references used in the thesis writing process, whether they were from published or unpublished books, journals, scholarly pieces, newspapers, reports, etc. Additionally, no portion of this thesis has been submitted elsewhere for consideration for any other degree or certification. The research presented in this thesis is based on work done at the Leibniz-Institut für Astrophysik Potsdam (AIP).

Acknowledgement

I express my profound gratitude to my esteemed mentor, Dr. Nikolay Kacharov, whose exceptional guidance, expertise, and unwavering encouragement have been the cornerstone of this research endeavor. Dr. Kacharov's visionary mentorship and passion for scholarly exploration have been a constant source of inspiration, shaping the trajectory of this dissertation.

My heartfelt thanks extend to Dr. Cardona-Barero Salvador for generously providing the invaluable dataset of the cosmological simulation, enabling the foundation of this study.

I am immensely grateful to the distinguished Prof. Dr. Maria-Rosa Cioni for her invaluable insights, scholarly wisdom, and unwavering encouragement throughout this research. Her guidance has significantly enriched the depth and quality of this work.

I extend my sincere appreciation to Dr. Yuves Revaz for his invaluable support and assistance in conducting the N-body simulations at the University of Geneva.

My deepest gratitude also goes to my parents and family members for their unwavering support, unwavering encouragement, and continuous inspiration throughout my academic journey.

I wish to acknowledge the insightful contributions of Dr. Daya Nidhi Chattkuli, Sonia Vaquero Suela, Elisabeth Steinhauser-Gleinser and all my friends and colleagues. Their invaluable insights, constructive feedback, and unceasing encouragement have immensely contributed to the refinement and development of this project.

Abstract

Prolate rotation is characterized by a significant rotation around the major axis of the galaxy which is in contrast to the more common oblate rotation. Prolate rotation is thought to be due to major mergers and thus studies of prolate-rotating systems can help us better understand the hierarchical process of galaxy evolution. Dynamical studies of such galaxies are important to find their gravitational potential profile, total mass, and dark matter fraction. Recently, it has been shown from the cosmological simulation that it is possible to form a prolate-rotating dwarf galaxy following a dwarf-dwarf merger event. The simulation also shows that the unusual prolate rotation can be time enduring. In this particular example, the galaxy started rotating around its major axis about 7.4 Gyr ago and it is continuing at present. In this project, we use mock observations of the hydro-dynamically simulated galaxy to fit various stages of its evolution with Jeans dynamical models. The Jeans model successfully fits the early oblate state before the major merger event, and also the late prolate stage of the simulated galaxy, recovering the anisotropy, mass distribution, velocity dispersion, and rotation of the simulated galaxy. This project also highlights the importance of hydrodynamic simulations in understanding the dynamics of galaxies, and how they can be used to make predictions and test hypotheses about real galaxies.

Zusammenfassung

Prolate Rotation ist durch eine signifikante Rotation um die Hauptachse der Galaxie gekennzeichnet, was im Gegensatz zur häufigeren oblaten Rotation steht. Man nimmt an, dass prolate Rotation durch größere Verschmelzungen verursacht wird, weshalb Studien von prolate-rotierenden Systemen dazu beitragen können, den hierarchischen Prozess der Galaxienentwicklung besser zu verstehen. Dynamische Studien solcher Galaxien sind wichtig, um ihr Gravitationspotenzialprofil, ihre Gesamtmasse und ihren Dunkle-Materie-Anteil zu ermitteln. Kürzlich wurde in einer kosmologischen Simulation gezeigt, dass es möglich ist, eine prolate-rotierende Zwerggalaxie nach einem Zwerg-Zwerg-Verschmelzungsereignis zu bilden. Die Simulation zeigt auch, dass die ungewöhnliche prolate Rotation über eine lange Zeit bestehen kann. In diesem speziellen Beispiel begann die Galaxie vor etwa 7,4 Milliarden Jahren, sich um ihre Hauptachse zu drehen, und dies setzt sich bis heute fort. In diesem Projekt verwenden wir Mock-Beobachtungen der hydrodynamisch simulierten Galaxie, um verschiedene Stadien ihrer Entwicklung mit Jeans-Dynamikmodellen zu fitten. Das Jeans-Modell passt erfolgreich den frühen oblaten Zustand vor dem größeren Verschmelzungsereignis und auch den späten prolaten Zustand der simulierten Galaxie an und ermittelt dabei die Anisotropie, die Massenverteilung, die Geschwindigkeitsdispersion und die Rotation der simulierten Galaxie. Dieses Projekt unterstreicht auch die Bedeutung hydrodynamischer Simulationen für das Verständnis der Dynamik von Galaxien und wie sie verwendet werden können, um Vorhersagen zu treffen und Hypothesen über reale Galaxien zu testen.

List of Figures

Contents

Chapter 1

Introduction

The challenge in astrophysics lies in deciphering the true nature of celestial objects since we can only observe their projected images in the sky. Galaxies, varying in size, shape, color, and brightness, present a wide spectrum of appearances, from majestic spirals to unassuming ellipticals, from massive cluster members to scarcely visible satellites nearby. Their appearance can change when observed from different angles and through various filters, such as optical and infrared imaging capturing starlight and far-infrared revealing dust emissions. While gravity is a fundamental force shaping galaxies, understanding their complete evolution involves the intricate interplay of radiation physics, hydrodynamics, nuclear fusion, and chemistry (Abraham et al., 1994; Abraham et al., 2003; Bovy & Rix, 2013; Bovy & Tremaine, 2012).

Dwarf galaxies, primarily consisting of dark matter, constitute the fundamental building blocks of larger galaxies, although they still elude complete comprehension. Dwarf galaxies, despite their smaller size and lower luminosity compared to larger galaxies, are subject to the same dynamic processes that shape the universe (Kado-Fong et al., 2020). They undergo major merger events, interact with other galaxies, and evolve over time, which also causes the galaxy to change its rotation axis (Cardona-Barrero et al., 2021).

Understanding the formation and evolution of galaxies remains a complex realm within extragalactic astrophysics (Cimatti et al., 2019). This encompasses comprehending the intrinsic nature of galaxies and exploring the distant universe. Key questions persist in deciphering the cosmic chronicle of star formation and black hole growth, especially their dependency on fundamental traits such as mass. The mechanics of star formation in the early universe are still unknown, but lots of new research is ongoing (Chaisson et al., 2014). Additionally, unraveling how galaxies procure and process their gas, alongside comprehending the influence of the environment on their evolutionary trajectories, poses significant challenges (Romano, 2022). Equally crucial is grasping the impact of feedback mechanisms arising from both stellar activities and black hole growth on the overall evolution of galaxies.

Galaxy rotation curves are another hot topic in astrophysics. Angular momentum plays a major role in galaxy formation and subsequent evolution. The majority of galaxies are found to be flat spinning disks (the Milky Way being no exception) (Hammer et al., 2007). However, it has been observed that galaxy shapes tend to be prolate at low mass and high redshifts and oblate at high mass and low redshifts (H. Zhang et al., 2019). This suggests that galaxies evolve from prolate to oblate, but the exact processes driving this evolution are not fully understood. Typically, prolate-shaped galaxies tend to be pressure-supported systems with very little angular momentum, if any (e.g. Tsatsi et al., 2017).

Most galaxies are generally assumed to exhibit oblate rotation due to the influence of gravity and centrifugal forces, there is also a possibility of prolate rotation in massive galaxies. Prolate rotation in galaxies is indeed a rare phenomenon and has been primarily observed in massive elliptical galaxies (Tsatsi et al., 2017) , but also rarely in dwarf galaxies like AND II(Amorisco et al., 2014) and Phoenix (Kacharov et al., 2017) within our Local group. This phenomenon is often attributed to major merger events during a galaxy's evolutionary history. While prolate rotation is more commonly associated with giant elliptical galaxies (Krajnović et al., 2018), its occurrence in dwarf galaxies is exceptionally rare, and the underlying mechanisms driving this phenomenon remain poorly understood (Ebrová & Łokas, 2017).

Deason et al. (2014) suggested that approximately $\sim 10\%$ of satellite dwarf galaxies experience merger events within the virial radius and the stellar mass ratio is close to 0.1. This finding aligns with previous studies in the field, such as the work by Klimentowski et al. (2010), which also suggested that such merger events were more prevalent in the early universe. But If we move further out from the virial radius, the frequency of the dwarf-dwarf merger events almost doubles. This suggests that we have frequent major mergers in the outskirts of the galaxy or galaxy clusters (Deason et al., 2014; Martin et al., 2021; Rodriguez-Gomez et al., 2015; Wetzel et al., 2015).

The presence of prolate rotation in dwarf galaxies is not a common phenomenon in cosmological simulations, as noted by Deason et al. (2014). However, idealized N-body simulations, exemplified by the work of Łokas et al. (2014), have illuminated scenarios where prolate rotation can manifest. For instance, their study focused on AND II, the remnant of a merger involving two disk dwarf galaxies. Through N-body simulations, they crafted an evolutionary model illustrating the emergence of prolate rotation in this unique context. Furthermore, in hydrodynamical cosmological simulations akin to the Local Group's environment, Cardona-Barrero et al. (2021) unearthed just two prolate-rotating dwarf galaxies resulting from major mergers. This implies that prolate rotation in dwarf galaxies is indeed a rare occurrence, necessitating specific conditions like mergers or interactions to take place.

The possibility of prolate motion in galaxies is widely supported in cosmological simulations, particularly in giant galaxies with masses exceeding $10^{12} M_{\odot}$. In the Illustris simulation, for instance, 9 out of 21 studied galaxies were found to exhibit prolate rotation (Li et al., 2018). Additionally, observations using ground-based integral field spectrophotometry, such as the CALFIA (Tsatsi et al., 2017), also provide support for the prolate motion in giant galaxies. According to the CALFIA survey, approximately 27% of massive galaxies with masses exceeding $2 \times 10^{11} M_{\odot}$ display prolate rotation. This strengthens the notion of a correlation between galaxy mass and the presence of prolate motion.

Due to observational limitations, researchers often rely on simulated data to study the dynamics of galaxies. Simulations provide a powerful tool for investigating the complex physical processes and interactions that govern galaxy evolution. They allow researchers to control various parameters, study different scenarios, and obtain detailed information that is not easily accessible through observations alone (Katz et al., 1995; Springel, 2005; Vogelsberger et al., 2014; Vogelsberger et al., 2020).

One particularly useful approach is zoom-in simulations, which focus on specific regions of interest, such as the Local Group, compact groups, or individual galaxies. By zooming in on these smaller scales, researchers can study the detailed dynamics and interactions occurring within these systems. This provides a more comprehensive understanding of the processes shaping their evolution. Zoom-in simulations offer the advantage of higher resolution and more accurate modeling of the physics at play. They allow for a detailed examination of the interplay between baryonic matter (such as gas and stars) and dark matter, as well as

the effects of various astrophysical processes, such as feedback from supernovae and black holes. This level of detail is crucial for understanding the formation and evolution of galaxies on small scales (Revaz & Jablonka, 2018; Revaz et al., 2009; Schaller et al., 2023; Vogelsberger et al., 2020).

Kinematics of the galaxy provides us with crucial information about its structure, internal dynamics, and gravitational interactions and allows us to reconstruct its formation histories, along with studying different substructures such as supermassive black holes (SMBH), dark matter halos, and baryonic physics (Bertin, 2014; Binney & Tremaine, 2011; Cappellari, 2008, 2016; Cimatti et al., 2019; Courteau et al., 2014; Gregory et al., 2019; Mo et al., 2010; Nevin et al., 2021; Schulze et al., 2018). One of the main problems in studying the kinematics of galaxies is obtaining accurate tracers, such as the 3D positions and velocities of individual stars within a galactic system (Binney & Tremaine, 2011; Cappellari, 2016). Thankfully, the GAIA mission has significantly contributed to overcoming the challenge of obtaining the positions and velocities of stars. It has provided extensive data on the positions and velocities of stars in the Milky Way galaxy, nearby dwarf galaxies, and even some stars in the Andromeda galaxy (Brown et al., 2021; Gaia et al., 2018).

Furthermore, in the case of galaxies that aren't perfectly edge-on, determining the intrinsic stellar luminosity density by de-projecting the observed star surface brightness becomes a mathematically non-unique task, even when assuming axisymmetry. This inherent ambiguity becomes more pronounced as the galaxy's inclination angle increases, adding an extra layer of complexity to the process of dynamical modeling for external galaxies. Detailed explanations will be provided in Chapter 3.

This study's fundamental aspect lies in its use of dynamical models fitted to mock observed stellar kinematics, obtained from a cosmological simulation. In most galaxies, the rotation will shift from prolate to oblate (H. Zhang et al., 2019), but in this particular system, we noticed the shifting of the rotation from oblate to prolate. Our primary objective is to assess the applicability of the Jeans axisymmetric model within the framework of a cosmological simulation. We have a specific focus on a dwarf galaxy that experienced a change in its axis of rotation over its evolutionary history. Additionally, we are exploring whether the core-cusp problem might explain the dynamics of this galaxy. Significantly, this research represents the first attempt to apply the Jeans model to a prolate rotator.

We chose this topic inspired by the Cardona-Barrero et al. (2021) work. They delved into 27 simulated dwarf galaxies within a stellar mass range similar to those in the Local Group. Remarkably, they uncovered a prolate rotator, an unusual finding in low-mass galaxies, with a total mass of $2.8 \times 10^9 M_\odot$ and a stellar mass of $1.4 \times 10^7 M_\odot$ at $z = 0$. Despite a low-amplitude velocity gradient, their analyses using mock datasets convincingly excluded the possibility of such a gradient arising from a non-rotating system. This discovery marks the first identification of a prolate rotating galaxy with such modest mass through non-idealized cosmological simulations.

The transformation from an oblate to a prolate rotator was primarily induced by a major merger event, occurring roughly 6 billion years ago, and subsequently stabilizing. Notably, the level of rotation observed in this galaxy at $z = 0$ is notably lower than that detected in known prolate rotating dwarfs within the Local Group. Their findings reveal a steep metallicity gradient akin to that observed in the Phoenix and AND II galaxies (Kacharov et al., 2017), primarily shaped by the merger event responsible for the prolate rotation and subsequent star formation processes concentrated in the inner regions.

This study stands out by examining the application of Jean models to a dwarf galaxy characterized as a prolate rotator in a cosmological simulation. This unique choice is motivated by recent findings, as

suggested by Cardona-Barrero et al. (2021), that prolate rotation can result from major mergers during the early stages of galaxy evolution, and this prolate rotation can persist for extended periods. This long-lasting prolate rotation prompted our investigation into the effectiveness of the Jeans model for such systems and its overall suitability in quasi-equilibrium.

Our main goal is to assess how well the Jeans model can determine the galaxy's mass in a prolate system. This is important because it allows us to uncover hidden components within the galaxy, like dark matter. Essentially, we're checking if our model's predictions match the actual mass distribution of the galaxy. It's worth noting that according to El-Badry et al. (2017), this can be especially challenging in low-mass dwarf galaxies, where the Jeans model may predict more mass than what's there. In this work, we are testing if the Jeans model can adequately reproduce the prolate rotation of the galaxy.

Furthermore, we are employing N-body simulations to forecast the future evolution of the galaxy. To achieve this, we've generated a mock dataset with a million stars, mirroring the projected surface brightness derived from the cosmological simulation, complete with spatial coordinates. We've assigned 3D velocities sampled from Gaussian distributions for each component, with a mean of $0\,\mathrm{km\,s^{-1}}$ and standard deviations measured in three distinct directions. This approach allows us to explore the potential trajectories and behaviors of the galaxy's components (Cardona-Barrero et al., 2021; Fouquet et al., 2017).

This step is essential to see if the prolate rotation we observed in the galaxy stays the same over a long time. We are using the Jeans equation to model a mock galaxy, and we predict the mass of the dark matter halo with this model. This helps us understand if the Jeans model works well for a long time.

Chapter 2

THEORETICAL BACKGROUND

2.1 Structure of galactic systems

The primary goal of this work is to comprehend the structure and characteristics of galaxies. To begin, it is essential to grasp the composition of galaxies. Galaxies mainly consist of stars, gas and DM. For example, our Milky Way hosts approximately 100 billion stars, with a combined mass of about $5 \times 10^{10} M_{\odot}$ solar masses. Most of these stars are concentrated in the central region of the galaxy and within a flat disk. Additionally, some stars are found in a spherical halo surrounding the disk, along with globular clusters.

Another significant component of galaxies is the interstellar medium, comprising gaseous and dust particles. Atomic and molecular hydrogen are its primary constituents. The mass of this interstellar medium is roughly 10% of the stellar mass. Although it does not contribute significantly to the galaxy's gravitational potential, it serves as a tracer of this potential.

Normal galaxies also contain a central supermassive black hole, which constitutes around 0.01% of the galaxy's total mass (Binney & Merrifield, 1998). The most substantial component of galaxies, however, is DM. The nature of DM remains elusive, but it is believed to consist of an undetected particle that interacts solely through gravity.

There is an alternative perspective proposing that DM does not exist, and instead, our understanding of gravity needs modification, as suggested by theories like Modified Newtonian Dynamics (MOND) (Milgrom, 2001, 2014).

2.1.1 Distribution of galactic components inside galaxy

As mentioned earlier, galaxies consist of various components, and here we delve into how these components are distributed within a galaxy. Stars within a galaxy are distributed exponentially concerning their distance from the galactic center. This distribution can be observed by examining the galaxy's light profile, a concept first elucidated by Freeman (1970). However, it's important to note that the distribution of light varies within the galaxy, with differences in the central region compared to the outer disk areas. Fig. 2.1 illustrates the Phoenix dwarf galaxy and the distribution of its stars.

Figure 2.1: The Phoenix dwarf galaxy. Credit: European Southern Observatory
https://www.eso.org/public/images/potw1838a/

Another crucial component of galaxies is gas, which constitutes all the baryonic matter in gaseous form. Gas exists within the galaxy in both atomic and molecular forms. However, quantifying the exact amount of gas in a galaxy is a challenging task. This difficulty is especially pronounced when attempting to determine the quantity of hot gas residing in the galactic halo (McKee et al., 2015; W. Zhang et al., 2009).

We have covered the distribution of stars and gas within a typical galaxy. However, a significant contributor to a galaxy's mass is its dark matter halo. Dark matter is a mysterious and abundant component of the universe, comprising nearly 5 times Ade et al. (2016) of the total matter content, vastly dominating the ordinary matter.

Another significant component of galaxies is star clusters, encompassing both open and globular clusters. Open clusters are loosely bound associations of stars confined within a relatively small region, typically around 10 pc in size. Thousands of open clusters have been identified in the Milky Way's galactic disk, as documented in studies such as Kharchenko et al. (2013).

In contrast, globular clusters are typically much denser and can contain anywhere from thousands to millions of stars, spanning a size range of a few to 10 parsecs. These clusters formed in the early stages of galaxy evolution, dating back almost to the age of the universe itself. Detailed catalogs of these globular clusters, like the one by Harris et al. (2013), provide valuable insights into their properties. Additionally, kinematic studies, such as those mentioned in Koch et al. (2018), contribute to our understanding of these fascinating cosmic structures.

Fig. 2.2 illustrates the mass contributions from different components of the galaxy, including the disk, bulge, dark matter, and the combined mass. It is evident that the mass of the dark matter component dominates over the other components, highlighting its significant influence on the overall dynamics of the galaxy.

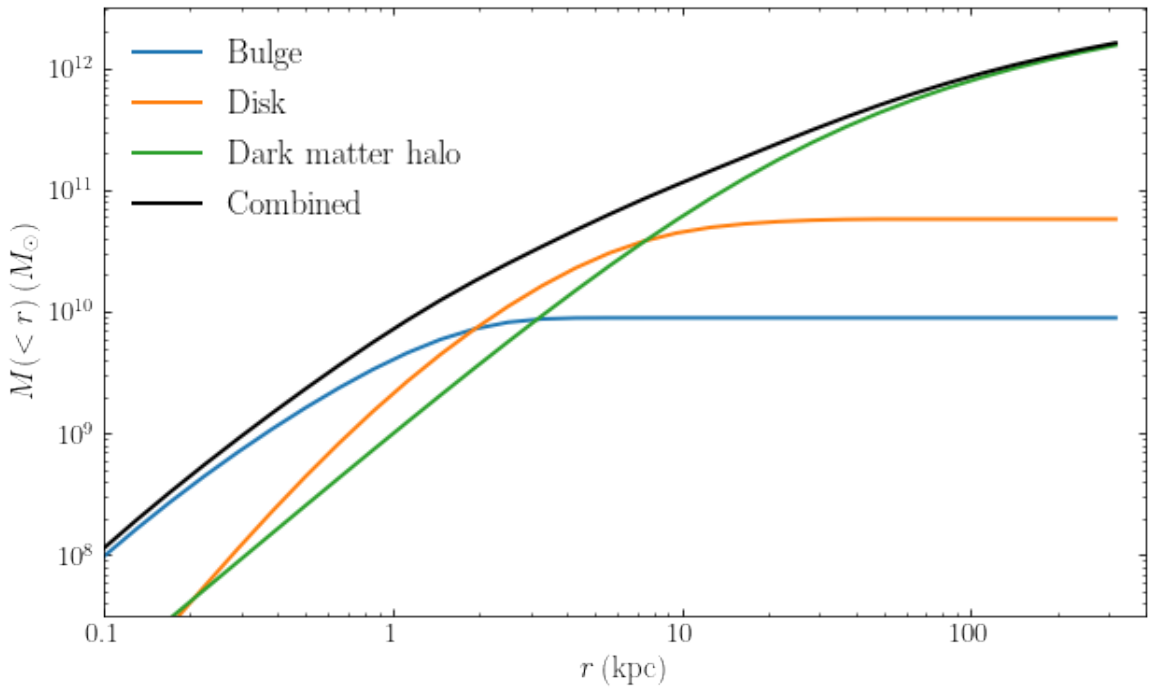

Figure 2.2: Mass of the each galactic components of the Milky way galaxy using the fitted models taken from (McMillan, 2016).

2.2 Dwarf Galaxies

Dwarf galaxies, with their diverse types based on factors like mass and gas content, are pivotal components in the formation of larger galaxies. They offer insights into galactic evolution, responding sensitively to factors like stellar feedback and heating. Moreover, these galaxies, submerged in dark matter, play a significant role in understanding the hierarchical evolution of galaxies (Crnojević & Mutlu-Pakdil, 2021; Lelli, 2022).

In particular, dwarf galaxies are crucial for comprehending the formation of galaxies in general, with the halos of more massive galaxies believed to form in part through the interaction and with accretion of the lower mass galaxies. Multi-billion particle N-body simulations have been instrumental in shedding light on the formation and evolution of dwarf galaxies, refining predictions made by the ΛCDM cosmology and enhancing our understanding of dark matter (Ebrová & Łokas, 2015, 2017; Łokas et al., 2014).

Studying dwarf galaxies within the Local Group is especially valuable due to their proximity, enabling detailed observations of their star formation processes and providing prototypical examples of galaxy evolution. These galaxies, potentially the building blocks of larger galaxies, are essential for unraveling the mysteries of dark matter and comprehending the processes that shape our Universe. By characterizing the composition and properties of dwarf galaxies, we gain insights into galactic chemical evolution and the mechanisms driving star formation (Fattahi et al., 2020; Mateo, 1998; Tolstoy et al., 2009).

Moreover, these studies shed light on the dynamics and evolution of this group of galaxies. The interactions between the Milky Way and its dwarf satellites offer insights into the mechanisms of galaxy formation. Dwarf galaxies play a pivotal role in advancing our understanding of structure formation, star formation processes, feedback mechanisms, and chemical evolution. Their simplicity and relatively undisturbed na-

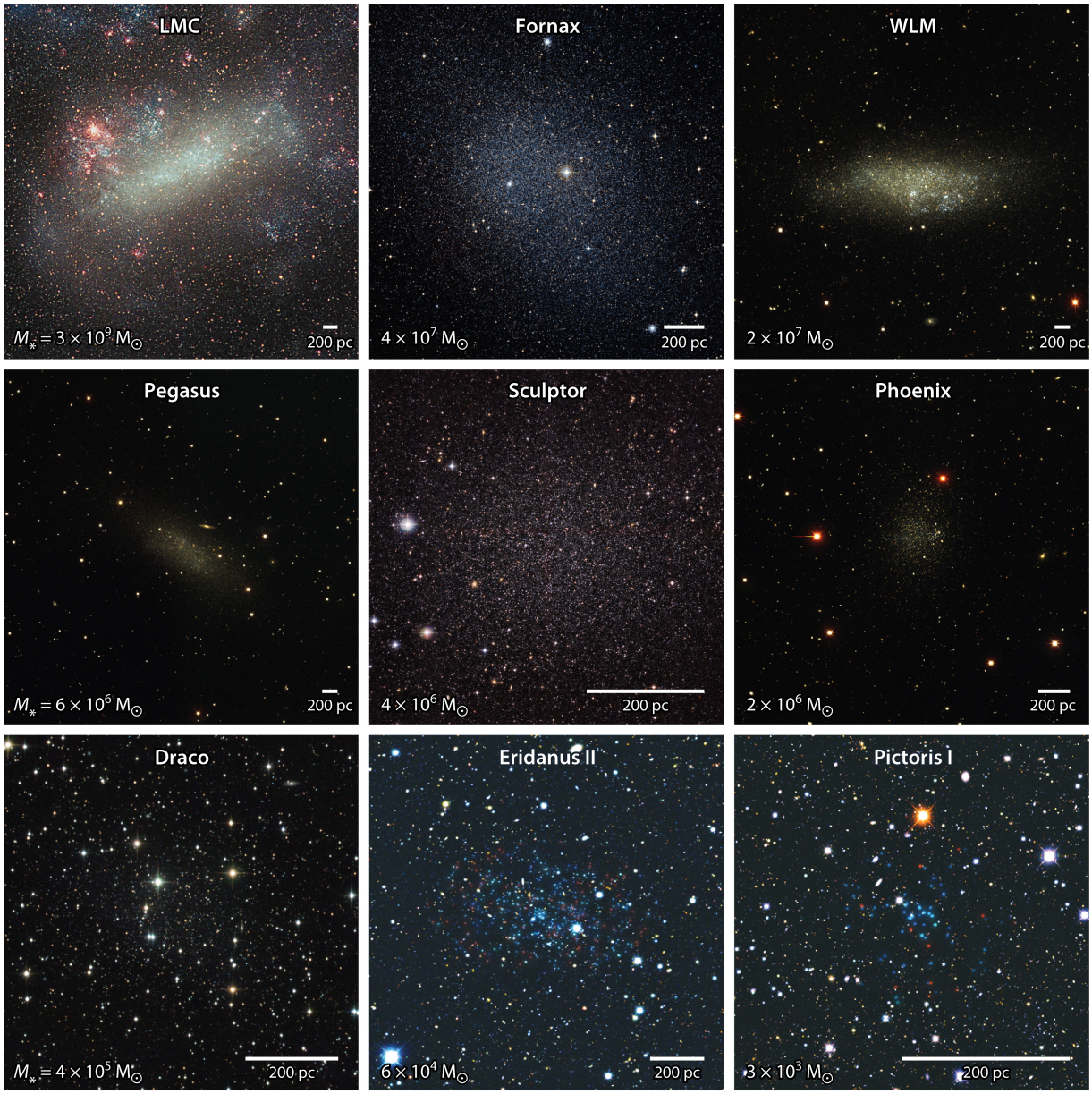

Bullock JS, Boylan-Kolchin M. 2017.
Annu. Rev. Astron. Astrophys. 55:343–87

Figure 2.3: Dwarfs spanning six orders of magnitude in stellar mass. The LMC, WLM, and Pegasus are dwarf irregular galaxies, with gas and ongoing star formation. Image credits: Eckhard Slawik (LMC); ESO/Digitized Sky Survey 2 (Fornax); Massey et al. (2007; WLM, Pegasus, Phoenix); ESO (Sculptor); Mischa Schirmer (Draco), Vasily Belokurov and Sergey Koposov (Eridanus II, Pictoris I). Abbreviations: LMC, Large Magellanic Cloud; WLM, Wolf–Lundmark–Melotte (Bullock & Boylan-Kolchin, 2017) .

ture make them ideal for studying these processes in isolation (Ricotti & Gnedin, 2005).

In summary, dwarf galaxies in the Local Group are essential testbeds for theoretical ideas related to cosmology, dark matter, and galaxy formation. Additionally, they serve as valuable laboratories for understanding the physical processes driving galaxy evolution, offering insights into these galactic clusters' dynamics and evolution. Simple comparision with the different dwarf galaxies with their internal masses and their photometric differences are shown in Fig. 2.3.

2.3 Cosmological Simulations

Cosmological simulations are powerful tools for studying the universe's fundamental questions, providing insights into cosmic formation and evolution. These simulations model physical processes like gravity and gas dynamics, allowing us to understand observable features and test theoretical models. They help researchers explore phenomena occurring over vast cosmic scales, complementing observations and enhancing our comprehension of the universe (Vogelsberger et al., 2013; Vogelsberger et al., 2020).

Two common types of cosmological simulations are dark matter-only and those including both baryonic matter and dark matter. These simulations are essential for studying processes within galaxies, like star formation and changes in metal content. By including baryonic matter, they capture the complex interplay of gas, stars, and dark matter, offering deeper insights into galaxy evolution and various physical processes (Springel et al., 2005; Vogelsberger et al., 2014).

Zoom-in simulations are specialized cosmological simulations that focus on smaller-scale processes within galaxies or galaxy clusters. They enable the study of detailed phenomena, such as galaxy interactions, star formation, and the effects of supernovae and black hole feedback. These simulations are invaluable for comprehending the universe's cosmic evolution and addressing significant questions in astrophysics and cosmology (Oñorbe et al., 2014; Sparre & Springel, 2016).

2.4 Jeans Equations

2.4.1 Collisionless system

We discussed above that galaxies are made of different components but one of their important properties is that they are collisionless stellar systems. Ideally, galaxies are not in the exact equilibrium state but keep being perturbed by infalling gas and small halos. However, collisionless is a good approximation to studying the dynamics of the galaxy on an evolutional timescale.

The gravitational force that acts between the stars in a galaxy is long-range. This means that stars in a galaxy are subject to a more constant gravitational force, unlike the violent and short-lived accelerations experienced by molecules in a diffuse gas as they collide with each other. The two-body relaxation time is way larger than the current age of the Universe for all galaxies (Binney & Tremaine, 2011).

Stellar systems are driven to equilibrium by non-collisional forces such as violent relaxation and phase mixing, which operate on the dynamical time scale rather than the two-body relaxation time scale. The

dynamical time for a typical galaxy is ~ 100 Myr, which means that galaxies reached a quasi-equilibrium state at present time. Dynamical time is roughly related to the velocity as $t_{dyn} = R/v$ dynamical time increases with increasing R, as for all galaxies $v \sim constant$ for large R. This suggests that dynamical time at the outer end (~ 100 kpc) of the galaxy is nearly equal to the age of the universe. This suggests that we can assume equilibrium for most of the places inside the galaxy (Binney & Merrifield, 1998; Binney & Tremaine, 2011).

2.4.2 Collisionless Boltzmann equation (CBE)

The most fundamental equation to discuss a collisionless system is the *Collisionless Boltzmann Equation*, in which the position and the velocity of a large systems of stars inside galaxy can be explained by the distribution function (DF) which is a phase space function of six variables (3 positional and 3 velocity components).

The DF of the stars in a steady-state gravitational system must fulfill the steady-state Boltzmann equation, which is the primary equation governing stellar dynamics. The Boltzmann equation describes the statistical behavior of many objects, including stars, when gravitational forces are present. In a steady-state system, the star's DF remains constant throughout time and the forces pulling on them are balanced, creating an equilibrium (Binney & Tremaine, 2011; Cappellari, 2008).

$$\frac{\partial f}{\partial t} + \sum_{i=1}^{3} (v_i \frac{\partial f}{\partial x_i} - \frac{\partial \phi}{\partial x_i} \frac{\partial f}{\partial v_i}) = 0 \tag{2.1}$$

where $i = x, y, z$ in Cartesian coordinate system.

f is the DF, so the above equation 2.1 can have infinite family of solutions. For a practical implementation of the equation, additional presumptions and simplifications are required. The problem can be severely constrained by investigating only the velocity moments of the DF, instead of reconstructing the DF as is usually done, which leads to the Jeans equations (Binney & Tremaine, 2011; Jeans, 1922).

2.4.3 The Jeans equations

As stated in the section above, equarion 2.1 takes a wide range of solutions depending upon the boundary conditions. We can solve 2.1 by, (i) by finding the equilibrium distribution function for a given potential and a given density, (ii) measuring the mass distribution from the observables (position and velocity) assuming the system is in equilibrium.

It is very difficult to get the distribution function of all the stars in a galaxy. So, it is not a easy task to solve the CBE. However, we can solve equation 2.1 by multiplying with x or v and integrating over a phase-space to obtain moment equations which are known as Jeans equations (Cappellari, 2008; Jeans, 1922).

Basically, the Jeans equations give us the moments of the distribution function. We do the astronomical observations at a fixed position on the sky, multiplying the collisionless Boltzmann equation by v and integrating over all the velocity components, it connects with the quantities which can be measured directly. The number density of the system is given by,

$$\rho(x) = \int df\, f(x,v) \tag{2.2}$$

And the mean velocity of the equilibrium system is,

$$\overline{v}(x) = \frac{1}{\rho(x)} \int v\, df\, f(x,v) \tag{2.3}$$

which has components of $\overline{v}_i$. where $i = 1, 2, 3$ for the three different axes.

We can describe the velocity dispersion tensor $\sigma(x)$ with components of $\sigma_{ij}(x)$, where $i, j = 1, 2, 3$

$$\sigma_{ij}(x) = \frac{1}{\rho(x)} \int \mathrm{d}v\, (v_i - \bar{v}_i)\, (v_j - \bar{v}_j)\, f(x,v) \tag{2.4}$$

We can also define the higher order moments in similar fashion but it will become more complicated.

Multiplying equation 2.1 by v^β (where $\beta = 0, 1, 2, 3...$) and integrating over v we can derive a set of Jeans equations that relate the above mentioned moments.

For simplicity , let us integrate equation 2.1 over v, we get,

$$\int dv\, \frac{\partial f}{\partial t} + \int dv\, \dot{x}\, \frac{\partial f}{\partial x} - \frac{\partial \phi}{\partial x} \int dv\, \frac{\partial f}{\partial v} \tag{2.5}$$

On simplification this equation takes the form,

$$\frac{\partial \rho(x)}{\partial t} + \nabla.[\rho(x)\, \overline{v}(x)] = 0 \tag{2.6}$$

This is the continuity equation for density. This equation contains both density and the 3D- mean velocity. Therefore, single equation is not sufficient to solve for the mean velocity.

Similarly we can multiply equation 2.1 by v and integrating over all v and substracting the $\overline{v}_j$ times the continuity equation leads the following equation (Binney & Merrifield, 1998; Jeans, 1922),

$$\rho \frac{\partial \overline{v}_j}{\partial t} + \rho\, \overline{v}_i\, \frac{\partial \overline{v}_j}{\partial x_i} + \rho\, \frac{\partial \phi}{\partial x_j} + \frac{\partial [\rho \sigma_{ij}^2]}{\partial x_i} = 0 \tag{2.7}$$

This Jeans equations relates density, mean velocity, velocity dispersion tensor and the gravitational potential. However, in this equation we have additional three equations (one for each direction), and we introduce six components of the velocity dispersion tensor. Therefore the system of the Jeans equations can't be solved directly and we need to make additional assumptions discussed in the next sections.

Continuing this process of multiplying higher powers of v and integrating over velocity gives us the Jeans equations involve higher moments of the DF.

Jeans equations are very powerful as they involve the quantities that can be easily observed such as the spatial density (can be traced through surface brightness or by counting stars), mean velocity and the velocity

dispersion.

The Jeans equations in cylindrical coordinates

The equation 2.1 can also be expressed in the standard cylindrical coordinate system (R, z, ϕ) under the assumption of axial symmetry, a common characteristic observed in many galaxies (Krajnović et al., 2011):

$$v_R \frac{\partial f}{\partial R} + v_z \frac{\partial f}{\partial z} + \left(\frac{v_\phi^2}{R} - \frac{\partial \Phi}{\partial R} \right) \frac{\partial f}{\partial v_R} - \frac{\partial \Phi}{\partial z} \frac{\partial f}{\partial v_z} - \frac{v_R v_\phi}{R} \frac{\partial f}{\partial v_\phi} \tag{2.8}$$

This approach simplifies the problem by considering that $(\partial\Phi/\partial\phi = \partial f/\partial\phi = 0)$ (Binney & Merrifield, 1998). However, it's important to note that while many galaxies exhibit axial symmetry, there are exceptions, and more complex models may be needed for those cases (Hofmeister & Criss, 2020).

We multiply equation 2.8, with the v_R and v_z we get two Jeans equations, (Binney & Merrifield, 1998; Jeans, 1922)

$$\frac{v\,\overline{v_R^2} - v\,\overline{v_\phi^2}}{R} + \frac{\partial(v\,\overline{v_R^2})}{\partial R} + \frac{v\,\overline{v_R\,v_z}}{\partial z} = -v\,\frac{\partial \Phi}{\partial R} \tag{2.9}$$

$$\frac{v\,\overline{v_R v_z}}{R} + \frac{\partial(v\,\overline{v_z^2})}{\partial z} + \frac{v\,\overline{v_R\,v_z}}{\partial R} = -v\,\frac{\partial \Phi}{\partial z} \tag{2.10}$$

The Jeans equations in spherical coordinates

We can solve the CBE 2.1 in spherical polar coordinates by assuming the axial symmetry, which will further simplifies the equation. On the assumption of axial symmetry, $\frac{\partial \Phi}{\partial \phi} = \frac{\partial f}{\partial \phi} = 0$ we get the CBE as,

$$v_r\ \frac{\partial f}{\partial v_\theta} + \frac{v_\theta}{r}\,\frac{\partial f}{\partial \theta} + \left(\frac{v_\theta^2 + v_\phi^2}{r^3} - \frac{\partial \Phi}{\partial r} \right) \frac{\partial f}{\partial v_r} + \frac{1}{r} \left(\frac{v_\phi^2}{\tan\theta} - v_r v_\theta - \frac{\partial \Phi}{\partial \theta} \right) \frac{\partial f}{\partial v_\theta} - \frac{v_\phi}{r} \left(v_r + \frac{v_\theta}{\tan\theta} \right) \frac{\partial f}{\partial v_\phi} = 0\,. \tag{2.11}$$

where $p_r = v_r, p_\theta = r v_\theta, p_\phi = r \sin\theta v_\phi$ are the conjugate momenta of the system.

Multiplying equation 2.11 by v_r, v_θ respectively and integrating over all (p_r, p_θ, p_ϕ) using $dp_r dp_\theta dp_\phi = r^2 \sin\theta dv_r dv_\theta dv_\phi$, we get the Jeans equations in spherical coordinates.

$$\frac{\partial(\rho\overline{v_r^2})}{\partial r} + \frac{1}{r} \left[\frac{\partial(\rho\overline{v_r\,v_\theta})}{\partial \theta} + 2\,\rho\,\overline{v_r^2} - \rho\,\overline{v_\theta^2} - \rho\,\overline{v_\phi^2} + \frac{\partial \rho\overline{v_r\,v_\theta}}{\tan\theta} \right] = -\rho \frac{\partial \Phi}{\partial r} \tag{2.12}$$

$$r \frac{\partial(\rho\overline{v_r\,v_\theta})}{\partial r} + \frac{\partial(\rho\overline{v_\theta^2})}{\partial \theta} + 3\,\rho\,\overline{v_r v_\theta} + \frac{\rho\overline{v_\theta^2} - \rho\overline{v_\phi^2}}{\tan\theta} = -\rho \frac{\partial \Phi}{\partial \theta} \tag{2.13}$$

As we explained before, this equation is solely derived from the CBE, and the assumption of the axisymmetry. These equations don't depend on the DF and also do not require self-consistency (In self-consistent systems the gravitational potential is determined by the luminous density distribution.) In the equation 2.9, 2.10, if we know the density and assume the potentials, we can solve the unknowns, $\overline{v_R^2}$, $\overline{v_\phi^2}$, $\overline{v_R v_\phi}$, $\overline{v_z^2}$, we can get the velocity moments of the galaxy. On the other hand, if we assume the potential also we see in both equation 2.12, 2.13 there are four unknowns, $\overline{v_r^2}, \overline{v_\theta^2}, \overline{v_\phi^2}, \overline{v_r\, v_\theta}$. So we don't have the unique solution of Jeans equations.

Velocity ellipsoid

To obtain the unique solution to the Jeans equations, one needs to assume a shape and orientation of the velocity ellipsoid. Orbit integration calculations have shown that the velocity ellipsoid has a prolate spheroidal alignment in most galaxies with axisymmetric potentials. However working within this formalism is computationally prohibitive. Viable approximations for the velocity ellipsoid are to assume that it is either spherically, or cylindrically aligned with the gravitational potential. For more details about the velocity ellipsoid and its importance, I strongly suggest to read Cappellari (2008).

2.4.4 Solution of the Jeans equations in cylindrical coordinates

To solve the cylindrical Jeans equations, we assume that the velocity ellipsoid is alligned with the cylindrical coordinate system and the anisotropy is constant, and quantified with some constant, $\overline{v_R^2} = b\,\overline{v_z^2}$, above equations 2.9, 2.10 reduce to,

$$\frac{b\,v\,\overline{v_z^2} - v\,\overline{v_\phi^2}}{R} + \frac{b\,\partial(v\,\overline{v_z^2})}{\partial R} = -v\,\frac{\partial \Phi}{\partial R} \tag{2.14}$$

$$\frac{\partial(v\,\overline{v_z^2})}{\partial z} = -v\,\frac{\partial \Phi}{\partial z} \tag{2.15}$$

$b = 1$ corresponds to the semi-isotropic case (two integral), with the boundary condition, $v\,\overline{v_z^2} = 0$ as $z \to \infty$ which gives the very general solution of above equations.

$$v\,\overline{v_z^2}(R,z) = \int_z^\infty v\,\frac{\partial \Phi}{\partial z} dz \tag{2.16}$$

$$v\,\overline{v_\phi^2}(R,z) = b\left[R\frac{\partial(v\,\overline{v_z^2})}{\partial R} + v\overline{v_z^2}\right] + Rv\,\frac{\partial \Phi}{\partial R} \tag{2.17}$$

To get the solutions of the Jeans equations, we choose the parametrization of the stellar density and the total density (in our case only the dark matter). In the JAM models, light and mass profiles are parameterized as MGEs following the method introduced by Emsellem et al. (1994). In this framework, the projected surface brightness (I) of the object is given by

$$I\left(x',y'\right)=\sum_{k=1}^{N}\frac{L_k}{2\pi\sigma_k^2 q'_k}\exp\left[-\frac{1}{2\sigma_k^2}\left(x'^2+\frac{y'^2}{q_k'^2}\right)\right], \tag{2.18}$$

In this equation, for each of the *N* Gaussian components, L_k represents the total luminosity, q_k ranges from 0 to 1 and signifies the observed (projected) axial ratio, while σ_k represents the dispersion along the major axis. x', y' and z' represents the projected major, minor and along the line of sight in the plane of sky.

The deprojection of the surface brightness to get the intrinsic luminosity density is not unique, as it depends on the viewing angle. The degeneracy becomes more problematic at low inclination angles (Magorrian, 1999). The MGE method has the benefit of being able to maintain the roundness of the model, as stated by (Cappellari, 2002). This leads to the creation of realistic densities that resemble actual galaxies when viewed from any perspective. However, the method is unable to remove the inherent ambiguity of the deprojection. This factor must be taken into account when analyzing the results of galaxies that are nearly viewed from the front (Cappellari, 2008).

$$\nu\left(R,z\right)=\sum_{k=1}^{N}\frac{L_k}{\left(2\pi\sigma_k^2\right)^{3/2}q_k}\exp\left[-\frac{1}{2\sigma_k^2}\left(R^2+\frac{z^2}{q_k^2}\right)\right] \tag{2.19}$$

where, the intrinsic axis ratio is related to the projected axis ratio via

$$q_k=\frac{\sqrt{q_k'^2-\cos^2 i}}{\sin i}. \tag{2.20}$$

where, i is the inclination angle of the system. For face-on system $i=0^\circ$ and for edge on systems, $i=90^\circ$

We also describe the mass of the system as the series of different set of gaussians similar to the light profile as,

$$\rho\left(R,z\right)=\sum_{j=1}^{M}\frac{M_j}{\left(2\pi\sigma_j^2\right)^{3/2}q_j}\exp\left[-\frac{1}{2\sigma_j^2}\left(R^2+\frac{z^2}{q_j^2}\right)\right] \tag{2.21}$$

In the self-consistent scenario, the Gaussians are identical to those in equation 2.19, and we have $M=N,\sigma_j=\sigma_k,q_j=q_k,\mathrm{and}Mj=\gamma_k L_k$ where γ_k represents the mass-to-light ratio (M/L), which can vary across different components. In the non-self-consistent scenario, the density can be expressed as the sum of two sets of Gaussians: the first set is derived by deprojecting the surface brightness using equation , and the second set is obtained, for instance, by fitting a one-dimensional MGE model to an adopted analytic parameterization for the dark matter, such as the one proposed by (Navarro et al., 1997).

The gravitational potential generated from above density equation 2.21 is given by, (Binney & Merrifield, 1998; Emsellem et al., 1994)

$$\Phi\left(R,z\right)=-\sqrt{\frac{2}{\pi}}G\int_0^1\sum_{k=1}^{N}\frac{M_j\mathcal{H}_j(u)}{\sigma_j}\mathcal{D}u \tag{2.22}$$

$$\mathcal{H}_j(u) = \frac{\exp\left[-\frac{u^2}{2\sigma_j^2}\left(R^2 + \frac{z^2}{1-(1-q_j^2)u^2}\right)\right]}{\sqrt{1-(1-q_j^2)u^2}}. \tag{2.23}$$

Furthermore, the mass of black holes can be incorporated by introducing the Keplerian potential into the equation described above. For further details we suggest to read (Cappellari, 2008).

Using the above equations we can find a solution for the cylindrical Jeans equations by solving the velocity moments analytically for each Gaussian component of the luminous and potential MGEs:

$$\left[v\,\overline{v_R^2}\right]_k = b_k \left[v\,\overline{v_z^2}\right]_k \tag{2.24}$$

$$\left[v\,\overline{v_z^2}\right]_k = 4\pi G \int_0^1 \sum_{j=1}^{1} \frac{\sigma_k^2\, q_k^2\, v_k\, q_j\, \rho_{0,j} H_j(u) u^2}{1 - Cu^2}\, du \tag{2.25}$$

$$\left[v\,\overline{v_\phi^2}\right]_k = b_k \left[v\,\overline{v_z^2}\right]_k + 4\pi G \int_0^1 \sum_{j=1}^{1} \frac{\sigma_k^2\, q_k^2\, v_k\, q_j\, \rho_{0,j} H_j(u) u^2}{1 - Cu^2}\, D\, R^2\, du \tag{2.26}$$

where, $v_k = v_k(R,z), \rho_{0,j} = \rho_0(0,0)$ and,

$$C = 1 - q_j^2 - \frac{\sigma_k^2 q_k^2}{\sigma_j^2} \tag{2.27}$$

$$D = 1 - b_k q_k^2 - \left[(1-b_k)C + (1-q_j^2)b_k\right] u^2 \tag{2.28}$$

In this solution, the index k refers to the luminous MGE components and the index j to the potential MGE components, as elaborated in 2.19 and 2.21, respectively (b_k is an anisotropy parameter Cappellari, 2008; Watkins et al., 2013).

If b_k is not same for the individual Gaussians, the total luminosity-weighted anisotropy at certain spatial location (R,z) of an MGE model is given by standard definition (Binney & Mamon, 1982):

$$\beta_z(R,z) = 1 - \frac{\overline{v_z^2}}{\overline{v_R^2}} = 1 - \frac{\sum_k \left[v\,\overline{v_z^2}\right]_k}{\sum_k b_k \left[v\,\overline{v_z^2}\right]_k} \simeq 1 - \frac{\sum_k v_k}{\sum_k b_k v_k} \tag{2.29}$$

The final approximation is derived from the fact that $\left[\overline{v_z^2}\right]_k$, which is primarily a function of the total MGE potential, exhibits minimal variation across different Gaussians. In contrast, v_k can differ significantly and can vary by several orders of magnitude for various luminous MGE components. This permits the global anisotropy of an MGE model at a specific spatial location in the meridional plane to be approximately calculated from a straightforward luminosity-weighted sum of b_k.

The inherent values must be integrated along the line-of-sight (LOS) to produce observable data that can be compared with the kinematics of the galaxy. For this purpose, we establish a system of sky coordinates where the z'-axis is along the LOS and the x'-axis is aligned with the projected major axis of the galaxy. The galaxy coordinates (x, y, z) are related to the plane of the sky as,

$$\begin{pmatrix} x \\ y \\ z \end{pmatrix} = \begin{pmatrix} 1 & 0 & 0 \\ 0 & -\cos i & \sin i \\ 0 & \sin i & \cos i \end{pmatrix} \begin{pmatrix} x' \\ y' \\ z' \end{pmatrix} \tag{2.30}$$

where the z-axis coincides with the galaxy symmetry axis and the cylindrical radius is defied by $R^2 = x^2 + y^2$.The projected second velocity moment along the LOS $v_{los}^2 \simeq \overline{v_{z'}^2}$ for one luminous Gaussian component is then given by:

$$\left[\sum \overline{v_{los}^2}\right]_k = \int_{-\infty}^{\infty} \left\{ \left[v\,\overline{v_z^2}\right]_k \cos^2 i + \left(\left[v\,\overline{v_R^2}\right]_k \sin^2 \phi + \left[v\,\overline{v_\phi^2}\right]_k \cos^2 \phi \right) \sin^2 i \right\} dz' \tag{2.31}$$

The total second moment for the whole MGE model is then:

$$\left[\sum \overline{v_{los}^2}\right] = \sum_{k=1}^{N} \left[\sum \overline{v_{los}^2}\right]_k \tag{2.32}$$

By substituting equations 2.24, 2.25, 2.26 in 2.31 we can get the second velocity moment of the galaxy.

The second moment obtained from the substitution serves as a good estimate for the observed quantity $V_{rms} = V^2 + \sigma^2$, where V represents the mean stellar velocity and σ denotes the velocity dispersion.

However, calculating the first velocity moment can be challenging. The projected first velocity moments, represented as $\overline{v_{los}} = \overline{v_{z'}}$ are given by the following equation,

$$\sum \overline{v_{los}} = \int_{-\infty}^{\infty} v\overline{v_\phi} \cos\phi \sin i \, dz' \tag{2.33}$$

The Jeans equations 2.14 and 2.15 only provide predictions for the second velocity moment $\overline{v_\phi^2}$. Therefore, it is necessary to consider how to separate the ordered motion from the random motion. This is a crucial step in understanding the dynamics of the system (Cappellari, 2008).

$$\overline{v_\phi^2} = \overline{v_\phi}^2 + \sigma_\phi^2 \tag{2.34}$$

To accomplish this, we require an additional parameter on the tangential anisotropy. This is a fundamental constraint of the first-moments equations, implying that we need a distinct parameter for the first moment V. This different parameter will enable us to solve the Jeans equation for both V and σ. This approach helps us to better understand the dynamics of the system by separating the ordered and random motions.

To quantify the rotation of the galaxy we need the first moment equation which can be done by two ways,

i) assuming the cobstant anisotropy for each of the Gaussian component, in the (v_R, v_ϕ) coordinates and analogously the equation 2.24 becomes,

$$\left[v\,\overline{v_\phi^2}\right]_k = C_k \left[v\,\overline{v_R^2}\right]_k \tag{2.35}$$

Which implies

$$[v\,\overline{v_\phi}]_k = \left(\left[\overline{v_\phi^2}\right]_k - C_k \left[\overline{v_R^2}\right]_k\right)^{1/2} \tag{2.36}$$

But the mean velocity depends in a non-linear way on C_k parameter. For this reason we adopted the semi-isotropic case, which consists of defining a constant κ which gives an idea about how much the model velocity field scaled with respect to the isotropic rotator.

Here, we used the anisotropic case, which gives the direct measurement of the amount of the rotation. We define for each of the Gaussian component,

$$[\overline{v_\phi}]_k = \kappa_k \left(\left[\overline{v_\phi^2}\right]_k - \left[\overline{v_R^2}\right]_k\right)^{1/2} \tag{2.37}$$

$\kappa_k = 0$: This indicates a non-rotating galaxy where random motions, rather than rotation, dominate the balance of forces.

$\kappa_k > 0$: As κ increases, rotational support becomes more significant, indicating that rotation plays a more prominent role in balancing the gravitational forces. The stars exhibit more ordered motion aligned with the rotation axis.

$\kappa_k = 1$: As κ The stars move predominantly along circular orbits aligned with the rotation axis, which means the velocity ellipsoid is a sphere everywhere. The upper limit of the κ_k is estimated by $\sigma_\phi^2 > 0$

For all the Gaussian MGEs, we can get the first velocity moment as

$$v\overline{v_\phi} = \left[v \sum_{k=1}^{N} \kappa_k^2 \left(\left[v\overline{v_\phi^2}\right]_k - \left[v\overline{v_R^2}\right]_k\right)\right]^{1/2} \tag{2.38}$$

We need to assume that the velocity ellipsoid is aligned with the spherical coordinate system in order to solve the above Jeans equations. In this case, the cross terms of the second velocity moment tensor vanishes and we get much simpler equations to solve.

2.4.5 Solution of the Jeans equations in spherical coordinates

Assuming that the velocity ellipsoid is aligned spherically, the Jeans equations reduces into,

$$\frac{\partial(\rho\overline{v_r^2})}{\partial r} + \frac{2\,\rho\,\overline{v_r^2} - \rho\,\overline{v_\theta^2} - \rho\,\overline{v_\phi^2}}{r} = -\rho\frac{\partial\Phi}{\partial r} \tag{2.39}$$

$$\frac{\partial(\rho\overline{v_\theta^2})}{\partial\theta} + \frac{\rho\overline{v_\theta^2} - \rho\overline{v_\phi^2}}{\tan\theta} = -\rho\frac{\partial\Phi}{\partial\theta} \tag{2.40}$$

One can solve the equation 2.40, as it does not contain the radial velocity dispersion. But for the global solution of the Jeans equations, we can relate the radial velocity dispersion and the angular velocity dispersion which is termed as anisotropy.

$$\beta = 1 - \frac{\overline{v_\theta^2}}{\overline{v_r^2}} = 1 - \frac{\sigma_\theta^2}{\sigma_r^2} \tag{2.41}$$

Using the so called velocity anisotropy, the Jeans equation becomes,

$$\frac{\partial(\rho\overline{v_r^2})}{\partial r} + \frac{(1+\beta)\,\rho\overline{v_r^2} - \rho\overline{v_\phi^2}}{r} = -\rho\frac{\partial\Phi}{\partial r} \tag{2.42}$$

$$(1-\beta)\frac{\partial(\rho\overline{v_r^2})}{\partial\theta} + \frac{(1-\beta)\rho\overline{v_r^2} - \rho\overline{v_\phi^2}}{\tan\theta} = -\rho\frac{\partial\Phi}{\partial\theta} \tag{2.43}$$

Now, let's consider the simplest Jeans equations for a spherically aligned velocity ellipsoid. By solving the aforementioned equations, we can obtain the solution for $\rho\overline{v_r^2}(r,\theta)$, which represents the second velocity moment along the radial direction. In a similar manner, we can derive the solutions for the other components of the second velocity moment tensor.

$$\overline{v_\theta^2} = (1-\beta)\overline{v_r^2} \tag{2.44}$$

$$\sigma_\phi^2 = (1-\gamma)\overline{v_r^2} \tag{2.45}$$

$$\overline{v_\phi}^2 = \sigma_\phi^2 - \overline{v_\phi^2} \tag{2.46}$$

When fitting velocity dispersion relations, we may encounter difficulties when galaxies exhibit counter-rotation of their stellar components. To account for this, we introduce a rotation parameter known as κ which is almost similar to the cylindrical case.

$$\overline{v_\phi} = \kappa\left[\left[\overline{v_\phi^2}\right] - (1-\beta)\left[\overline{v_r^2}\right]\right]^{1/2} \tag{2.47}$$

For further details about solving Jeans equations in Spherical coordinate system I will suggest to read Cappellari (2020).

Chapter 3

METHODOLOGY

Studying the motion of stars or gas within galaxies helps us map the galaxy's gravitational potential and, consequently, the total mass contained within a specific radius. (Leung et al., 2018) In dynamical models, we construct the distribution of stars in phase space based on the galactic potential, which is determined by the integral of motion. We assume that the distribution function is in a steady state and apply Jeans' theorem accordingly.

The Jeans dynamical models link the generally derived observations of stellar density and the kinematics of the modeled system to its gravitational potential. In this study, we utilized a cosmological simulation as an input parameter for the Jeans dynamical models.

In this study, we utilize the Python version of the axisymmetric JAM code developed by M. Cappellari (Cappellari, 2008). Our analysis relies on the 3D velocity map and velocity dispersion data for the transitioning dwarf galaxy, as specified in Cardona-Barrero et al. (2021). The JAM code incorporates a MGE to characterize both the surface luminosity density, obtained from the cosmological simulation, and the gravitational potential, including the contribution of dark matter.

From the simulation, we know the surface brightness profile of the galaxy and perform a simple Sérsic profile fit (equation 3.1) to obtain its total surface brightness given by equation 3.2, half-light radius, and Sérsic index.

$$I(R) = I_e \cdot \exp\left\{-b_n\left[\left(\frac{R}{R_e}\right)^{\frac{1}{n}} - 1\right]\right\} \tag{3.1}$$

In the Sérsic profile equation, R_e denotes the scale radius, and b_n represents a constant. The value of b_n is obtained from a numerical solution, while the Sérsic index n varies depending on the type of galaxy. (Sérsic, 1963) For Sérsic index n=4, value for the Sérsic constant is 7.66924944 from the numerical solution (Ciotti & Bertin, 1999).

For elliptical galaxies, the Sérsic index typically ranges from 2 to 10, while disk galaxies have a value of around 1. Disky bulge-type galaxies have a Sérsic index between 1 and 2. Fitting the surface brightness profile using a single Sérsic index can be challenging. To improve the fit, it is common to fit the outer and inner surface brightness with two different Sérsic indexes and then combine the fits to obtain a single fit that

yields lower errors. However, given the spatial resolution of the cosmological simulation, we use a single Sérsic model in this work.

Integrating equation 3.1 over the radial component while assuming an ellipticity (ϵ) yields the total intensity of the galaxy,

$$L = 2\pi(1-\epsilon)R_{\rm e}^2 I_{\rm e} \times \frac{n\, {\rm e}^{b_n}}{(b_n)^{2n}} \times \Gamma(2n) \tag{3.2}$$

Solving the Jeans equations using Equation 3.2, which provides the total surface brightness of the galaxy, is significantly more computationally intensive and approximately an order of magnitude slower. To streamline the process, we represent the resulting total luminosity with a MGE of the galaxy's surface brightness, utilizing the desired Gaussian profiles. This approach greatly enhances the efficiency of solving the Jeans equations and simplifies the deprojection of the density profile, as detailed in Cappellari (Cappellari, 2002).

We determined the system's potential according to the equation 2.22, employing a mass density representation composed of a series of Gaussians. Importantly, it's worth noting that the mass Gaussians are separate from the luminous Gaussians, and the two are independent of each other.

On applying these inputs in the Jeans' equations in the cylindrical polar coordinate system, we can finally get the unique solution for the second moment. In doing that we further assume that the velocity ellipsoid is aligned with the cylindrical coordinate system which makes it easier to solve the equations.

In this study, we are investigating the evolutionary journey of a dwarf galaxy, specifically focusing on its transition from oblate rotation to prolate rotation. We have gathered approximately 200 snapshots of the galaxy's evolution, ranging from its early stages at redshift 6.4 to its current state at redshift 0. We selected three significant stages in the galaxy's evolution for detailed analysis. The first stage represents the early period when stars within the galaxy exhibit oblate rotation. The second stage corresponds to a significant event where the galaxy collides with a satellite galaxy. Lastly, we examine the final stage, where the galaxy changes its axis of rotation, transforming into a prolate rotator.

We utilized Voronoi binning data provided by Cardona-Barrero et al. (2021), with each bin containing 200 stars. We calculated the mean values of the surface brightness, and velocity moments for the stars within each bin. These binned values were subsequently employed in solving the Jeans' equation.

We have also created Voronoi maps (Cappellari & Copin, 2003) of the line of sight velocity (v_{los}) and velocity dispersion (σ) at different snapshots from the simulation. We assigned uncertainties to these values based on the local surface brightness (uncertainties increase with decreasing surface brightness).

In our dynamical model, the gravitational potential is driven by DM only. We used a generalized Herenquist (see equation 4.1) density profile to represent the gravitational potential to solve the Jeans equations.

In our analysis, we explored various dark matter profiles, including the cored NFW profile with ($\alpha = 1, \beta = 3, \gamma = 0$), the cusped NFW profile with ($\alpha = 1, \beta = 3, \gamma = 1$), and the generalized Hernquist profile. Our objective was to determine which of these models provides the best fit for the kinematic data derived from the cosmological simulation.

Our goal is to model the Voronoi binned dataset, where the number of bins varies with each snapshot based

on the simulated star points. This involves comparing models against the binned dataset using maximum-likelihood analysis. We calculate the maximum likelihood function by comparing the model obtained from the assumed parameter sets. Let Θ_j represent the parameter set for a particular model; then, the likelihood of observing bin i have given model j is given by (Watkins et al., 2013)

$$\mathcal{L}_{ij} = p\left(\boldsymbol{v}_i\, \boldsymbol{x}_i\, \boldsymbol{\sigma}_i\, \boldsymbol{\epsilon}_{v_i}\, \boldsymbol{\epsilon}_{\sigma_i} \,|\boldsymbol{\Theta}_j\right). \tag{3.3}$$

Where $\boldsymbol{x}'_i = (x'_i, y'_i)$ represents the binned position on the image plane which has observed velocity, $\boldsymbol{v_i} = (0, 0, v_(z, i)')$ (along the line-of-sight) and the error matrix of,

$$\boldsymbol{S^2}_i = \begin{pmatrix} 0 & 0 & 0 \\ 0 & 0 & 0 \\ 0 & 0 & \epsilon^2_{v_{z'},i} \end{pmatrix} \tag{3.4}$$

The best model is the set of parameters Θ_j that maximizes $\mathcal{L}_{ij}$. We should be very careful to select the starting parameters.

We employed the emcee Goodman and Weare (2010) Python package to implement the affine invariant Markov Chain Monte Carlo (MCMC) method for obtaining the maximum likelihood of the fitted parameters. The parameters we fit for include the central density (ρ_0) and scale radius (r_0) of the dark matter profile, along with the velocity anisotropy ($\beta_z = 1 - \frac{v_z^2}{v_r^2}$) and rotation amplitude (κ) of the galaxy. Our MCMC setup involved 98 random walkers and 1000 steps, providing sufficient iterations for the fit to converge.

With the obtained parameters from the fit, the JAM model predicts the velocity moments, first ($\overline{v}$) and second ($\overline{v^2}$) for each of the binned points in the dataset. Additionally, we calculate the volume mass density of the galaxy to estimate its total mass based on the fitted parameters.

Furthermore, we also calculate the mass of the galaxy using the Wolf mass estimator (Wolf et al., 2010) using the line-of-sight velocity dispersion and the half-light radius. The method is applicable to globular cluster, dwarf galaxies and the elliptical galaxies.

$$M_{1/2} = 3G^{-1} \left\langle \sigma^2_{los} \right\rangle r_{1/2} \simeq 4G^{-1} \left\langle \sigma^2_{los} \right\rangle R_e \tag{3.5}$$

where $\left\langle \sigma^2_{los} \right\rangle$ is the luminosity-weighted square of the line-of-sight velocity dispersion and the R_e is the 2D projected half-light radius (Wolf et al., 2010).

Performing the Jeans model is crucial for comprehensive dynamical modeling of the system. This allows us to create a mock dwarf galaxy that aligns with our predicted velocity moments. To achieve this, we implement inverse transverse sampling. By 3D deprojecting the fitted Sérsic profile of our galaxy, we obtain the positions of the star particles. Subsequently, using the JAM model, we derive the individual 3D velocities for our mock galaxy.

Now, armed with a complete galaxy model, including the desired number of points with the 3D positions and 3D velocities of the star particles, we conduct *N*-body simulations. This step allows us to explore and understand the future dynamics of the galaxy.

Chapter 4

RESULTS AND DISCUSSION

In this project, our objective was to assess the viability of Jeans models in capturing the kinematic evolution of prolate rotating systems using a well-established cosmological simulation. We analyse the evolution of the simulated galaxy at different cosmological times using the JAM model. We fit JAM model to predict the line-of-sight velocity and velocity dispersion of the galaxy and compared with the cosmological simulation. We aim to thoroughly investigate and analyze the simulation results to gain a deeper understanding of the evolution of rotation in merging galaxies.

Typically, low-mass dwarf galaxies exhibit intricate rotation patterns. As demonstrated by H. Zhang et al. (2019), a comprehensive analysis of galaxy shape and size distributions revealed that low-mass dwarf galaxies tend to have elongated shapes, while higher-mass galaxies exhibit a disc-like morphology. However, our current study, focused on a simulated galaxy, presents a distinctive scenario. Initially, the simulated galaxy rotates in an oblate manner, but subsequent to a merger event with a satellite halo, its rotation undergoes a significant transformation, as detailed in Cardona-Barrero et al. (2021). This departure from the typical behavior observed in low-mass dwarfs underscores the complexity and diversity of galactic evolution processes.

Previous studies have extensively tested the Jeans equations in galactic systems, primarily focusing on oblate rotation scenarios. However, our present study marks a notable departure by undertaking the first attempt to rigorously test the applicability of the Jeans equations in systems exhibiting prolate rotation. Moreover, our analysis encompasses the entire spectrum of the galaxy's evolutionary phases, providing a comprehensive examination of its rotational dynamics.

To study the kinematics of the simulated galaxy, we created mock observations that mimic the data obtained from Integral Field Units (IFUs). These mock observations allowed us to derive spatially resolved velocity and velocity dispersion maps, as well as surface brightness distributions. By analyzing these simulated observations, we were able to gain insights into the internal dynamics and structure of the galaxy.

On doing so, we solved the Jeans equations using the density obtained from the surface brightness MGE and the kinematics from the cosmological simulations. which we will briefly describe in the coming sections.

A crucial aspect to consider in solving the Jeans equations is the concept of velocity ellipsoids, which characterize the velocity dispersion along each axis of the galaxy. However, for the purpose of solving the Jeans equations, we made the assumption that the velocity ellipsoids are aligned with the chosen coordinate

system representing the orientation of the galaxy (Cappellari, 2008, 2020).

Another important criteria on doing the JAM model is angle of inclination. It's noteworthy that we employed an inclination angle of $i = 90^\circ$ (i.e., edge-on) to measure the galaxy's rotation accurately. The distance to the galaxy is another important factor for calculating its kinematics. In our analysis, we set the distance to the galaxy such that the angular size of 1 pc is $1''$, i.e. 206265 pc.

This thesis systematically presents our JAM model applied to three distinct stages of the galaxy evolution: the oblate rotation phase, representing the early stage of evolution; the early prolate rotation phase, occurring after the merger with the halo; and the late prolate rotation phase, representing the present stage of the galaxy's evolution. This comprehensive approach allows for a thorough examination of the galaxy's kinematics across various evolutionary states.

4.1 Initial inputs for JAM modeling

4.1.1 Surface Brightness

We only see the galaxy as a projected image in the sky. Studying the properties of the galaxy is still a complicated topic, especially the mass of the galaxy. For that, we first need to get more information from the image of the galaxy. More massive galaxies tend to have more stars and, therefore, emit more light. However, the relationship between mass and luminosity is not always straightforward, and different types of galaxies can have different mass-to-light ratios.

The surface brightness of the galaxy is the measurement of the light emitted by the individual stars inside the galaxy per unit area. As we discussed earlier, the brightness profile of the galaxy drops exponentially from the inner to the outer part (de Vaucouleurs, 1948).

From the observed surface brightness of a galaxy, one can construct isophotes, which represent the contours of equal brightness. These isophotes provide valuable information about the shape, structure, and orientation of the galaxy. Additionally, by analyzing the distribution of surface brightness, one can determine the half-light radius, which is a measure of the radius within which half of the galaxy's total light is emitted.

We can model the emitted surface brightness from a galaxy using various profiles, such as an exponential profile. However, the most accurate way to model it is using the Sérsic profile using the equation 3.1. The Sérsic profile provides a better representation of the photometric structure of the galaxy, capturing important features such as the central concentration and outer profile shape. This profile is widely used in analyzing galaxy photometry to study their properties and understand their formation and evolution.

In this study, we used the surface brightness profile obtained from the cosmological simulation, considering that the galaxy is in a state of quasi-equilibrium. We then fit the amplitude of the surface brightness $I(0)$, the half-light radius $r_{\frac{1}{2}}$, the Sérsic index n, and perform background corrections to obtain a more accurate representation of the galaxy's surface brightness distribution. The fitted parameters can be seen in Fig. 4.1.

In our simulations, we maintain a fixed projected ellipticity, a value derived from the simulation, and a constant total luminosity calculated using Equation 3.2, also based on simulation data. This ensures consistency with the known characteristics of the galaxy from our simulated model.

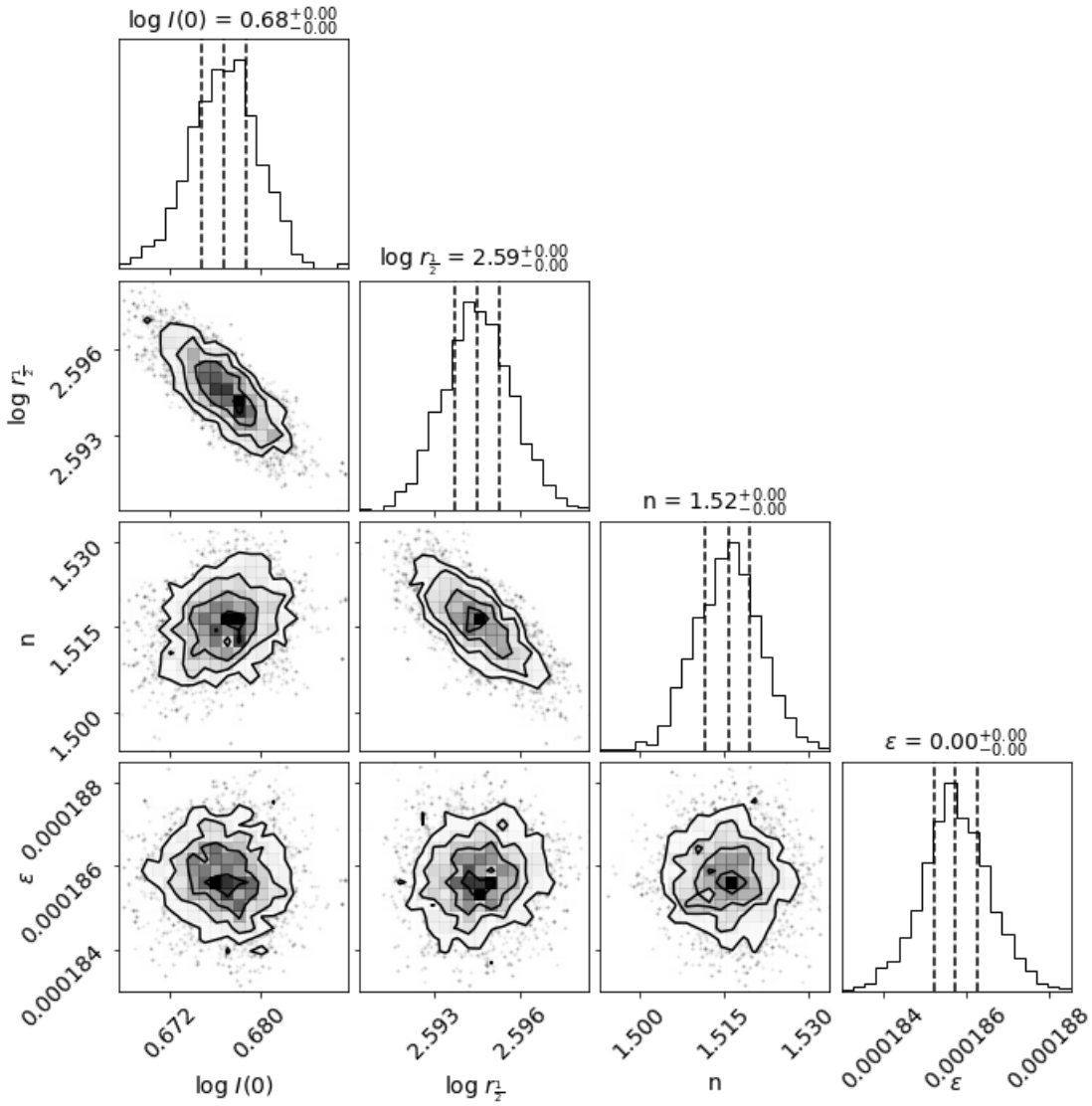

Figure 4.1: MCMC post-burn distributions depict the results of fitting a Sérsic model to the surface brightness profile of an oblate galaxy obtained from a cosmological simulation. The scatter plot shows the projected two-dimensional distributions and the solid lines show $1\,\sigma$, $2\,\sigma$, and $3\,\sigma$ regions of the projected covariance matrix. The fitted parameters are logarithmic central brightness $\log\, I(0)$, logarithmic half-light radius $\log\, \left(r_{\frac{1}{2}}\right)$, Sérsic index n, and the background level ϵ.

We utilized the fitted parameters to employ the Sérsic profile, to model the surface brightness of the galaxy derived from our cosmological simulation. Through the process of fitting the Sérsic profile to the observed surface brightness data, we were able to estimate crucial structural properties of the galaxy, including its size, shape, and luminosity.

As seen in the right panel of Fig. 4.2, the brightness profile produced from the Sérsic modeling has an excellent similarity to the one obtained from the cosmological simulation (the left panel). This visual agreement increases our trust in the Sérsic model's capacity to precisely and reliably represent the fundamental properties of the galaxy's surface brightness distribution.

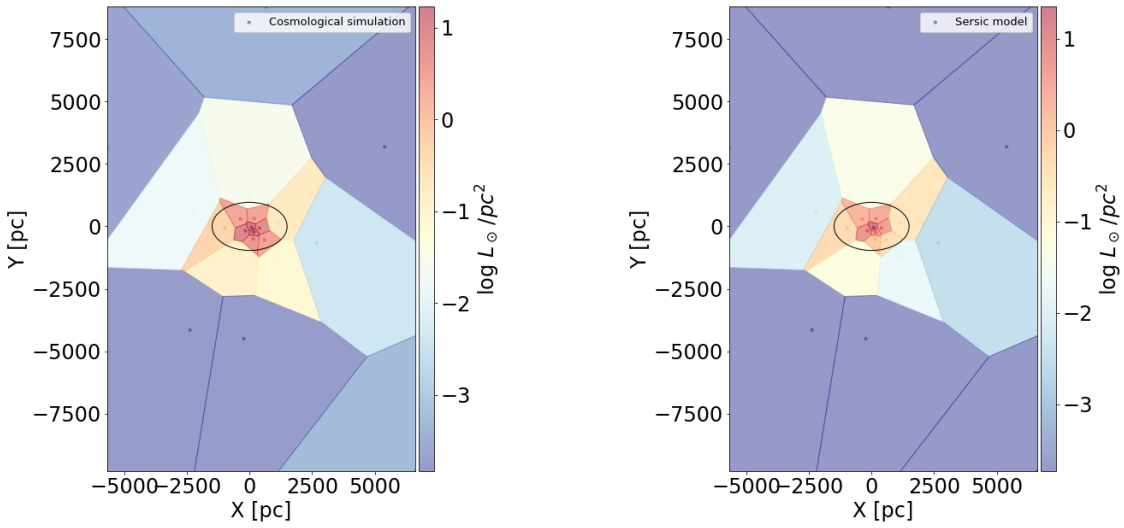

Figure 4.2: Comparision of the surface brightness profile from the cosmological simulation and the fitted Sérsic profile. The black ellipse represents the half-light radius of the galaxy.

Multi-Gaussian expansion (MGE)

We utilized the MGE approach to deproject the observed surface brightness of the galaxy. This method involves representing the stellar density distribution using a sequence of Gaussian functions. In our study, we specifically employed the Sérsic MGE model as a representative of the projected stellar density distribution (Emsellem et al., 1994).

In Fig. 4.3, the left panel showcases the one-dimensional Sérsic profile of the galaxy, incorporating the background correction, represented by the solid line. The blue dots correspond to the fitted Sérsic points obtained from the modeling process, while the red dots represent the data points derived from the cosmological simulations. It is important to note that the 1D Sérsic model shows the surface brightness profile along the major axis, while the dots are the individual Voronoi bins. Owing to the ellipticity and varying polar angles, the data points consistently fall below the solid line in our analysis.

Indeed, for the dynamical modeling, we utilize the surface brightness profile without the background correction. This decision is made under the assumption that the galaxy is in a state of perfect isolation, where external factors such as background noise or contamination are negligible. Consequently, we consider the galaxy to strictly adhere to the idealized Sérsic profile, as demonstrated in the right panel of Fig. 4.3, which shows the MGE. This simplified representation allows us to focus specifically on the intrinsic properties and dynamics of the galaxy itself.

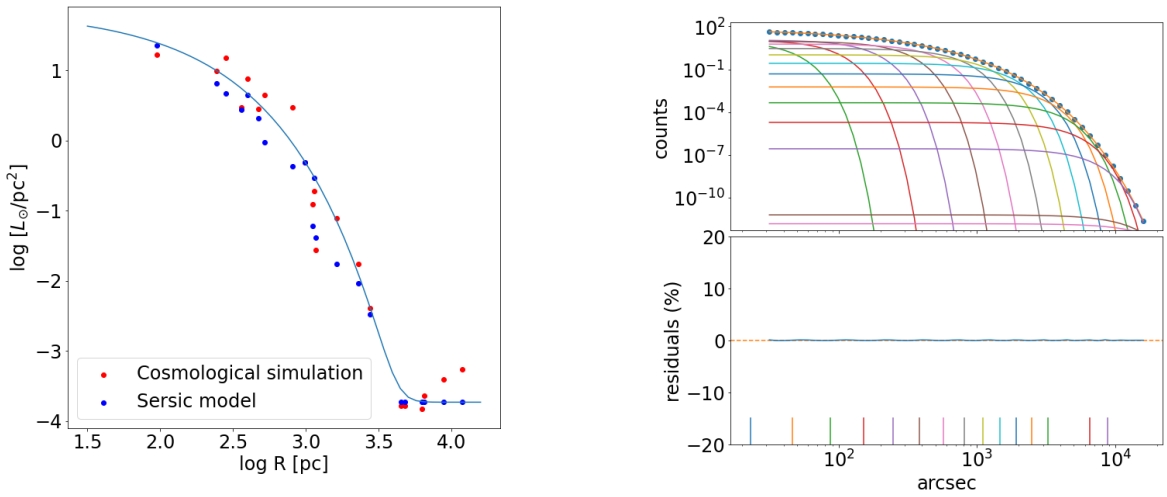

Figure 4.3: The left panel of the figure displays a side-by-side comparison between the surface brightness profiles derived from the cosmological simulation and the fitted Sérsic profile of the galaxy. The red dots represent the data points, whereas the blue points are representative of the the Sérsic fit in the same Voronoi bins. The solid line is along the major axis. In the right panel, we present the fitted MGE to the Sérsic model. Each of the colored lines represents an individual Gaussian components. The bottom panel shows their combined residuals.

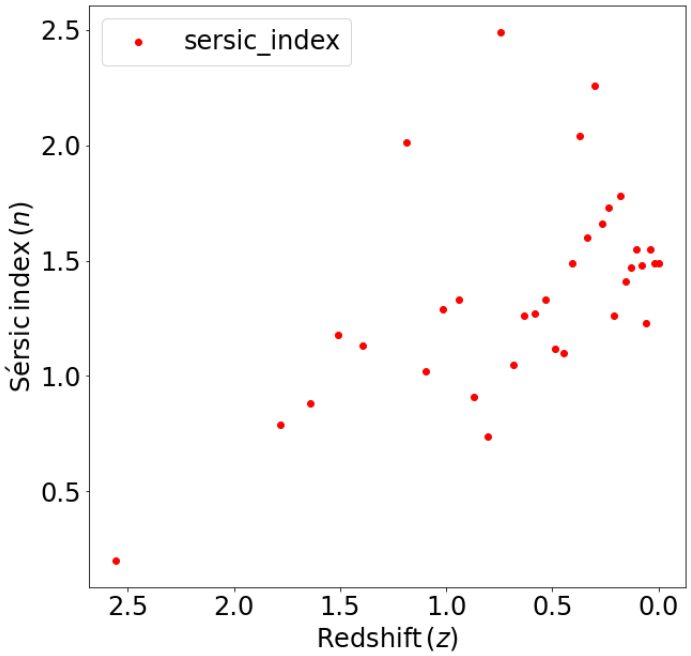

Figure 4.4: Evolution of the Sérsic index of the galaxy across different redshifts in the cosmological simulation.

Fig. 4.4 illustrates the dynamic evolution of the Sérsic index throughout various stages of the galaxy's evolution. The varying Sérsic index indicates the continuous transformation of the galaxy's shape over time. Notably, the Sérsic index predominantly falls within the range of $1 < n < 2$ indicative of a predominantly disk-like structure for the galaxy throughout its evolutionary phases. However, the specific morphology can depend on other factors as well, so it's always good to consider additional information when classifying

galaxies (Vika et al., 2015; Zahid & Geller, 2017).

4.1.2 Kinematics of the Galaxy

As previously mentioned, an essential component for the dynamical modeling of the galaxy is its kinematic data. In Cardona-Barrero et al. (2021), the line-of-sight velocity and velocity dispersion of the galaxy were mapped using Voronoi binning, as illustrated in Fig. 4.5. This approach is crucial as it involves binning the final dataset, enabling the calculation of velocity moments within each bin for a comprehensive kinematic analysis.

4.1.3 Jeans Anisotropic Multi-Gaussian Expansion (JAM) model

The JAM model is a powerful tool used to study the dynamics of galaxies. It relies on three main components: i) the density distribution ii) the gravitational potential and iii) kinematics of the system. In order to accurately solve the Jeans equations and derive meaningful results, it is crucial to have information about both the density and potential.

In this study, we utilize the density distribution derived from the Sérsic MGE, which provides a representative representation of the stellar density in the galaxy. Additionally, we obtain the gravitational potential from the mass distribution derived using the NFW MGE. By combining the density and potential information, we can effectively model and analyze the kinematics and dynamics of the galaxy using the Jeans equations.

Here in our models, we used the generalised Herniquist profile, which is defined as follows. (Hernquist, 1990)

$$\rho(r) = \frac{\rho_s}{\left(\frac{r}{r_s}\right)^{\gamma}\left[1+\left(\frac{r}{r_s}\right)^{\alpha}\right]^{(\beta-\gamma)/\alpha}} \tag{4.1}$$

In this context, ρ_s denotes the central density, r_s stands for the scale radius, and α represents the sharpness parameter governing the transition from the inner slope γ to the outer slope β.

The parameters (α, β, γ) in Equation 4.1 determine the specific DM profile. For instance, when (α, β, γ) equals (1, 3, 0), it corresponds to the cored NFW profile, while (α, β, γ) equal to (1, 3, 1) represents the cusped NFW profile. By considering these different DM profiles, we explored their impact on our dynamical models and their implications for the galactic dynamics.

Comparing the results of the two models which are crucial to evaluate their fit to the kinematics and mass profile of the galaxy. We can compare the predicted kinematic properties, such as line-of-sight velocity and velocity dispersion, from each model with the observed values to determine the best fit. Additionally, comparing the mass profiles from each model with the simulated mass will help assess their accuracy in capturing the mass distribution. Analyzing the deviations between the models and observed data will identify discrepancies and strengths/weaknesses. This comparison will determine the most reliable model for fitting the kinematics and mass profile of the galaxy.

The corner plots (Figs. 4.6 and 4.7) depict the fitted parameters and their correlations for each of the models, offering a comprehensive view of the parameter space exploration. In our model, the free parameters include

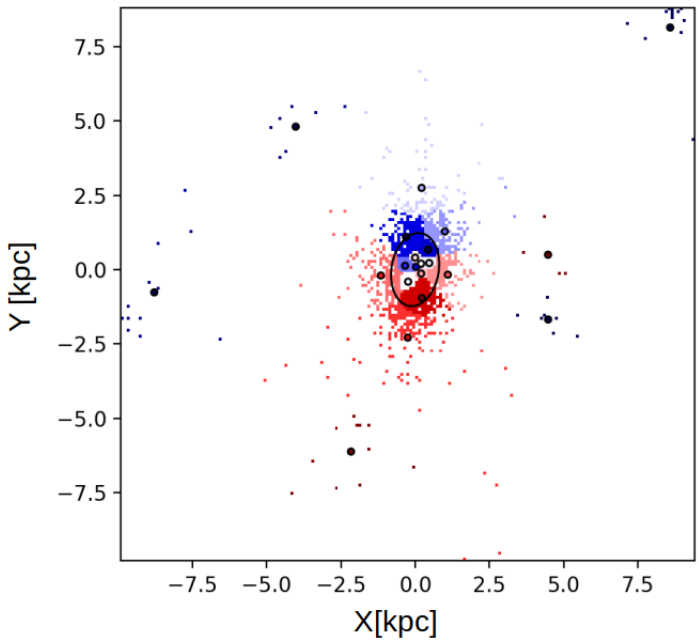

Figure 4.5: The presented image displays a velocity map of the galaxy at a redshift of $z = 1.58$. Notably, the map showcases a distinct rotational motion occurring along the galaxy's minor axis. The small points are particles from the simulation, while the larger dots are the surface brightness Voronoi bins, where the radial velocity is derived.

the central density and scale radius of the NFW profile, the velocity anisotropy, and the rotation of the galaxy. By examining the corner plots, we can gain insights into the relationships between these parameters and better understand their impact on the model's predictions.

4.2 Oblate rotation

We would like to remind readers that prior to the major merger event, which occurred approximately 7 Gyrs, the galaxy exhibited oblate rotation. The initial phase of the galaxy is important as the JAM model was successfully applied to such systems before which will be our point of reference for the further evolution of the galaxy.

4.2.1 Dynamical model of the galaxy at $z = 1.58$

In the simulation, the galaxy was initially an oblate rotator until redshift $z \simeq 1.58$. We chose to fit the Jeans Anisotropic MGE (JAM) model to this early stage because fitting the JAM model to oblate galaxies has been extensively studied. However, fitting the JAM model to prolate systems is not done before. Therefore, we used the oblate case as a benchmark to test the applicability of the JAM model to prolate systems. Fig. 4.5 shows the velocity map of the galaxy at redshift $z \simeq 1.58$, obtained from the cosmological simulation.

The selection of the DM halo profile continues to be a subject of active discussion, particularly when applied to galactic systems. The ΛCDM model predicts a cusped DM profile, while observational evidence often supports a cored DM profile for galaxies and dwarf galaxies (Hayashi et al., 2020; Wang et al., 2022). In this study, we aimed to reconcile this disparity by incorporating both cusped and cored DM profiles in our

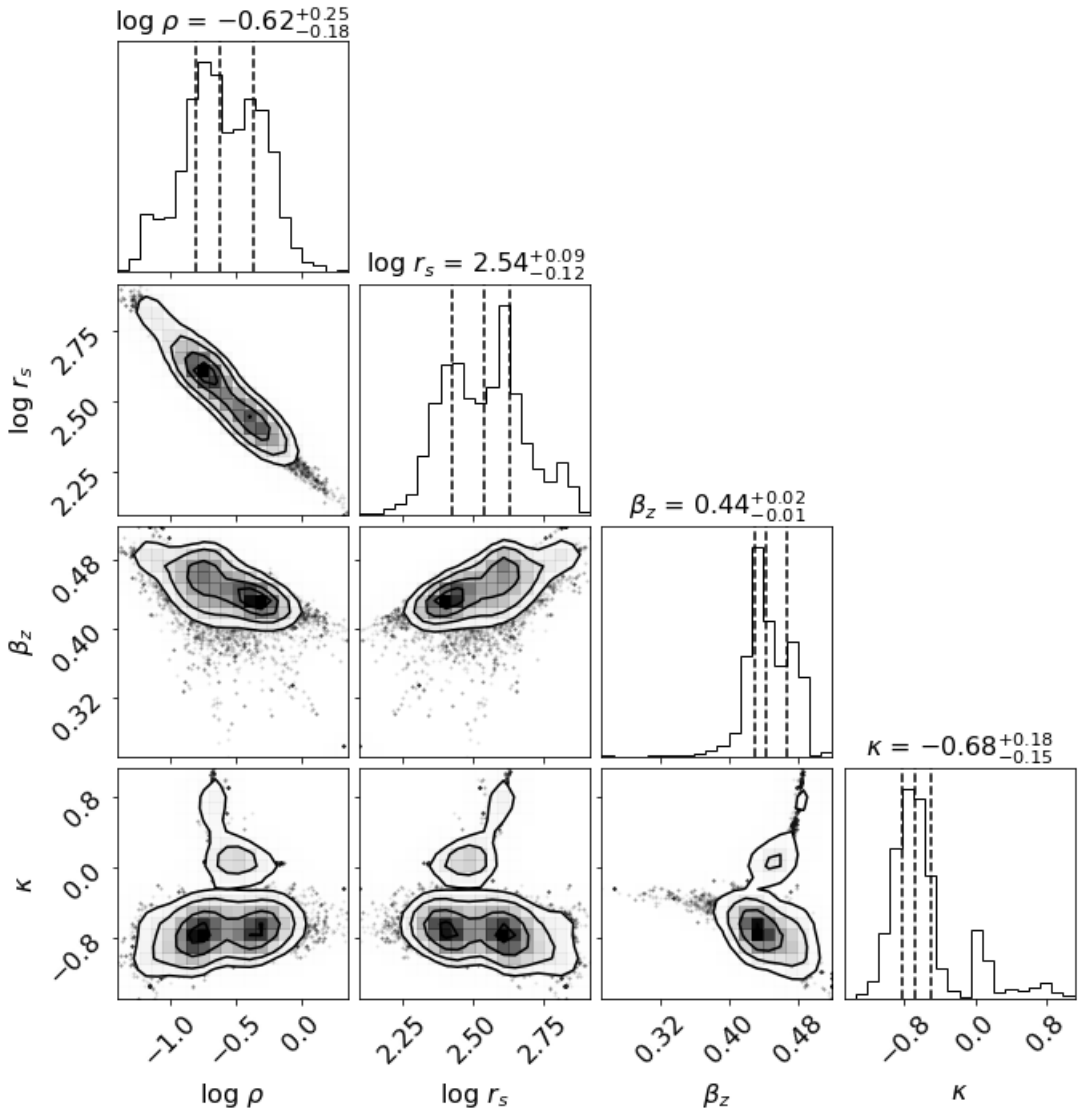

Figure 4.6: MCMC post-burn distributions depict the results of fitting a JAM model of the cored DM profile, and the solid lines show $1\,\sigma$, $2\,\sigma$, and $3\,\sigma$ regions of the projected covariance matrix. The fitted parameters are central density ($\log\,\rho$), scaled radius ($\log\,r_s$) for the DM halo and anisotropy (β_z), rotation (κ) for explaining the dynamics of the galaxy.

dynamical model. Through a thorough comparison of the results and fitting parameters obtained from these two profiles with the observed kinematics and mass profiles, we endeavored to discern which profile more accurately characterizes the underlying dynamics of the galaxy.

In the model shown in Fig. 4.6, we utilized a cored spherical DM profile. The corner plot showcases the fitted parameters for the dynamical models, including the rotation parameter κ and anisotropy β_z. The analysis indicates that our model exhibits anisotropy, with positive values for κ suggesting that the galaxy has an oblate velocity ellipsoid. This signifies that the galaxy's random motion is not uniform in all directions, but rather elongated along a major axis. The inclusion of the rotation parameter κ in our dynamical model allows us to capture and quantify the rotational behavior of the galaxy, providing further insights into its intrinsic structure and dynamics.

The MCMC post-burn distributions in Fig. 4.7 depict the results of fitting a JAM model of the cusped DM profile. The fitted parameters are central density ($\log\,\rho$), scaled radius ($\log\,r_s$) for the DM halo and

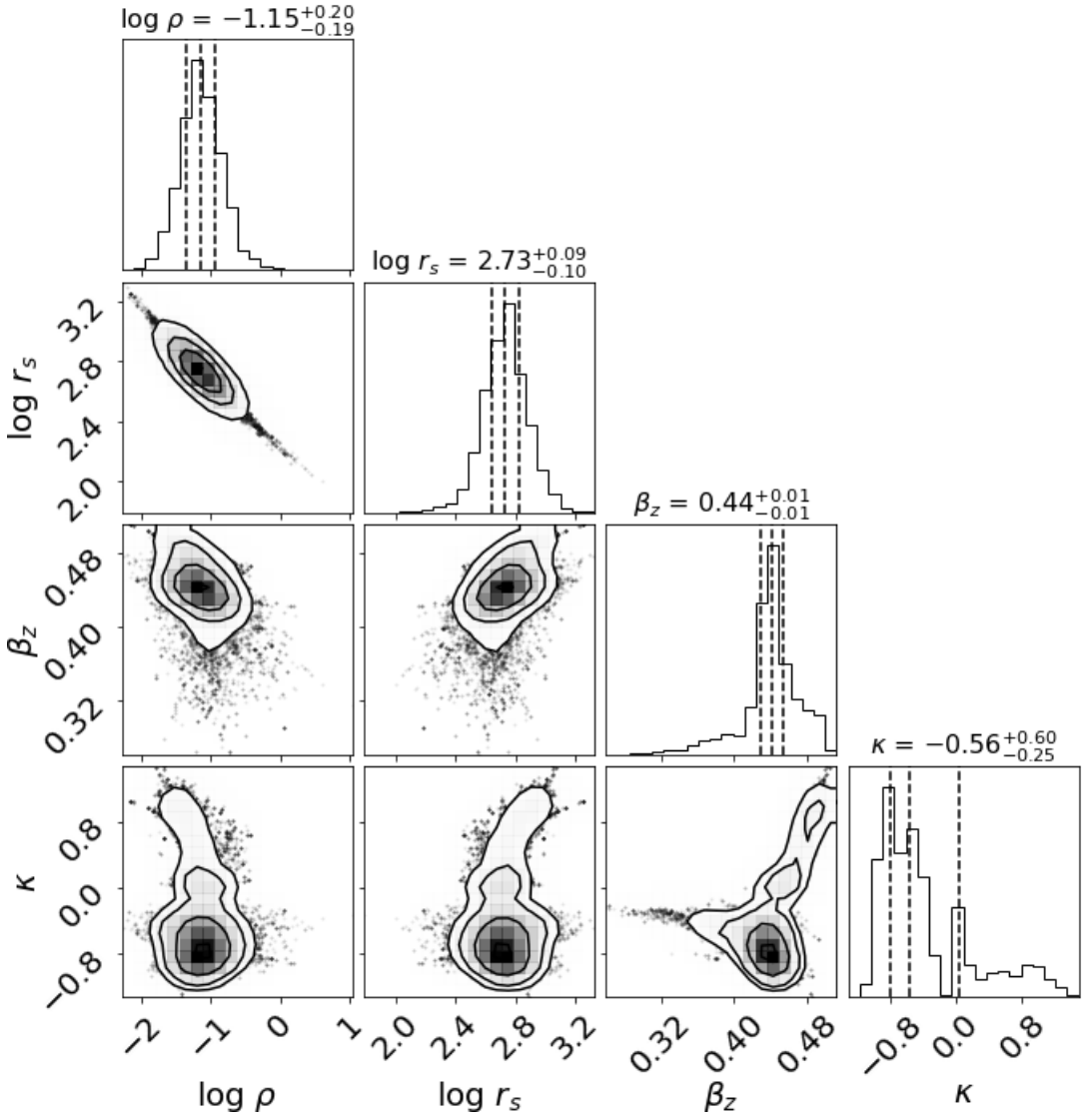

Figure 4.7: The same as Fig. 4.6, but for a cuspy NFW DM profile.

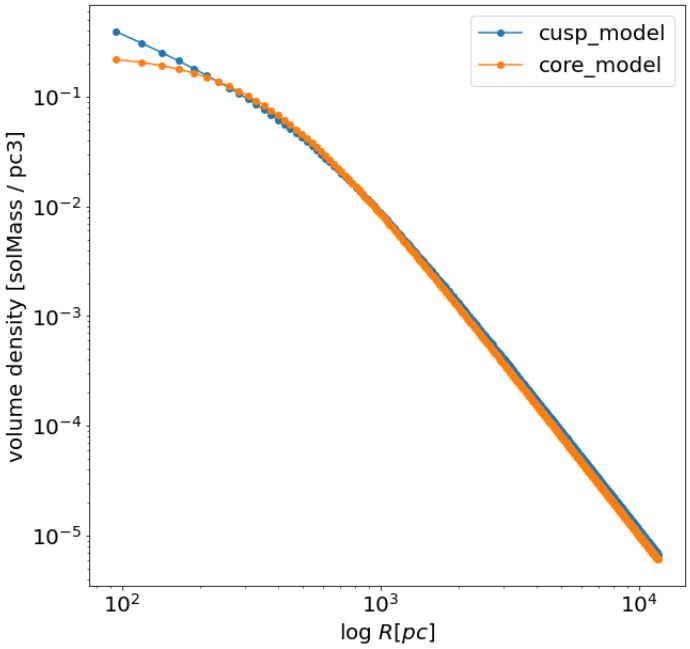

Figure 4.8: Density comparison of the fitted NFW profiles using the parameters obtained from the dynamical modeling, for both the cored and cusped density models.

anisotropy (β_z), rotation (κ) for explaining the kinematics of the galaxy.

Similarly, for the cusp model, the fitted parameters can be visualized in Fig. 4.7. This corner plot provides an overview of the parameter values obtained from the dynamical models using the cusp DM profile.

In the analysis of the two different DM halo profiles, we observed a remarkably close approximation of the rotation and velocity anisotropy (β_z), as well as the scale radius of the halo. However, a significant difference was evident in the density profile of the two fitted models. The core model exhibited a flattened density profile at the center, while the cusp model displayed a steeper density slope, as expected. This discrepancy in the density profiles highlights the impact of the different halo profiles on the overall mass distribution and kinematics of the galaxy shown in Fig. 4.8.

The top panel of Fig. 4.9 compares the line-of-sight velocities obtained from the cosmological simulation with the velocities predicted by the two different DM profiles used as gravitational potentials in the JAM model. This comparison allows us to evaluate the agreement between the simulated and modeled velocities, providing valuable insights into the accuracy of the JAM model in capturing the galaxy's kinematics.

In the upper panel of Fig 4.9 (middle), we see the results of the JAM model with the cored DM profile. It is evident that at the outer skirts of the galaxy, where the uncertainties are higher, we observe a larger mismatch. This indicates that the JAM model's performance is relatively less accurate in those regions. However, within the half-light radius of the galaxy, the JAM model demonstrates a remarkable level of accuracy in predicting the line-of-sight velocities. The closely clustered data points and the small error bars reflect the strong agreement between the modeled and simulated velocities in this region (see Fig 4.5).

The JAM model, particularly with the cored DM profile, effectively captures the galaxy's kinematics, pro-

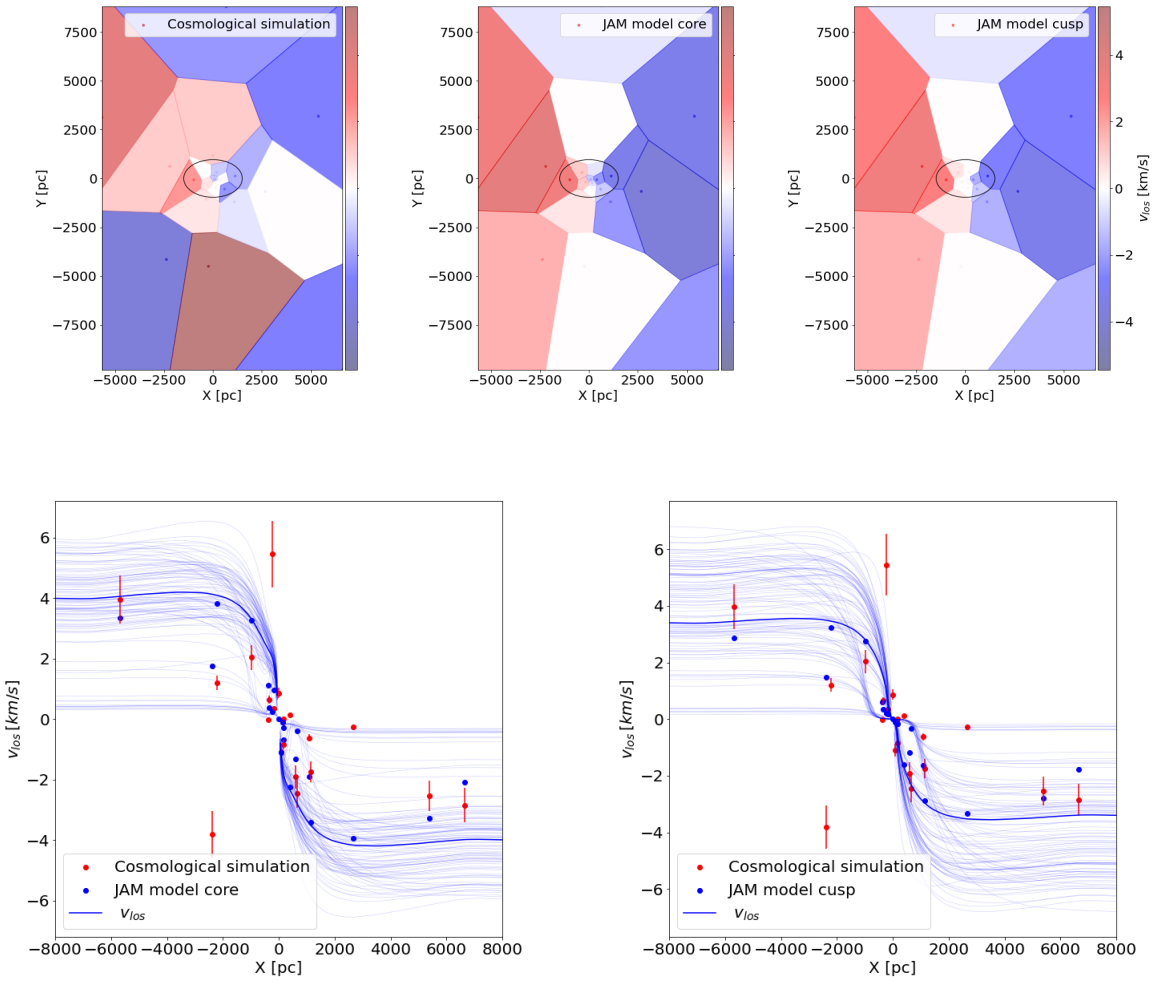

Figure 4.9: The upper panel displays the 2D line-of-sight velocity of the galaxy from three sources: the cosmological simulation (top left), the JAM model with a cored DM profile (top middle), and the JAM model with a cusped DM profile (top right). The lower panel shows the 1D line-of-sight velocity for both models. Red dots represent the location of the Voronoi bins, while blue dots indicate the corresponding line-of-sight velocities from the model. Blue solid lines show the rotation profile along the major axis obtained from the JAM model.

viding reliable predictions for line-of-sight velocities within the half-light radius. Discrepancies in the outer regions may stem from limited data points and complex dynamics. Overall, this comparison allows us to assess the JAM model's performance. Interestingly, the cusped DM profile predicts almost the same line-of-sight velocity as the cored profile, suggesting minimal differences in the first velocity moment. Both models offer a good match to observed velocities, showcasing their reliability in reproducing the galaxy's kinematics.

It is evident from the lower panel of Fig. 4.9 that the galaxy is rotating around its minor axis at the given time. The plot displays the distribution of data points, which exhibit a dispersion indicative of the expected range of velocities. This observation is further supported by the spread of the posterior distribution, indicating that our model accurately captures the variability and predicted behavior of the galaxy's rotational motion.

Similarly, in Fig. 4.10, we compare the velocity dispersion of the galaxy with the fitted JAM model. The upper panel of the plot displays the comparison of the velocity dispersion plot with the cosmological simulation and the fitted JAM models.

Upon examination of the plots, we observe that both models predict relatively similar velocity dispersion profiles for the galaxy. This indicates that the choice of the DM profile, whether cored or cusped, has a minimal impact on the overall velocity dispersion predictions.

In the lower panel of Fig. 4.10, the velocity dispersion profile is well revealed by the JAM model. The plot showcases the distribution of velocity dispersion values as a function of radial distance from the galactic center. The JAM model effectively captures the trends and variations in the velocity dispersion, providing a comprehensive understanding of how the dispersion changes across different regions of the galaxy.

Furthermore, it is worth noting that the v_{los}/σ ratio in our model is very low see in Fig. 4.11. This suggests that the galaxy is mostly pressure-dominated, with a limited amount of ordered motion.

Additionally, we also fitted the anisotropy parameter for the galaxy in both the cored and cusped gravitational potential models. The results indicate the presence of anisotropy in the second velocity moment, which corresponds to the velocity dispersion tensor. This suggests that the galaxy exhibits unequal velocity dispersions in different directions, indicating a non-spherical distribution of velocities.

Furthermore, the increasing anisotropy parameter indicates that the galaxy is more flattened (oblate) (Cappellari et al., 2007) implying that the galaxy's velocity distribution is elongated along the major axis, resulting in a flattened shape. This observation suggests that velocity anisotropy plays a significant role in providing dynamic support to the galaxy.

The presence of velocity anisotropy implies that the velocities of stars or other celestial objects within the galaxy are not randomly distributed, but exhibit preferential motions in certain directions. This anisotropy in the velocity distribution influences the overall dynamics of the galaxy, affecting its stability, shape, and mass distribution.

The dynamics of the galaxy plays a crucial role as it allows us to estimate the mass of the galaxy, which is a fundamental quantity in astrophysics. Utilizing the fitted dynamical parameters obtained from our analysis, we can predict the mass of the galaxy at a given time. This predicted mass can then be compared with the mass derived from the cosmological simulation, enabling us to assess the consistency and accuracy of

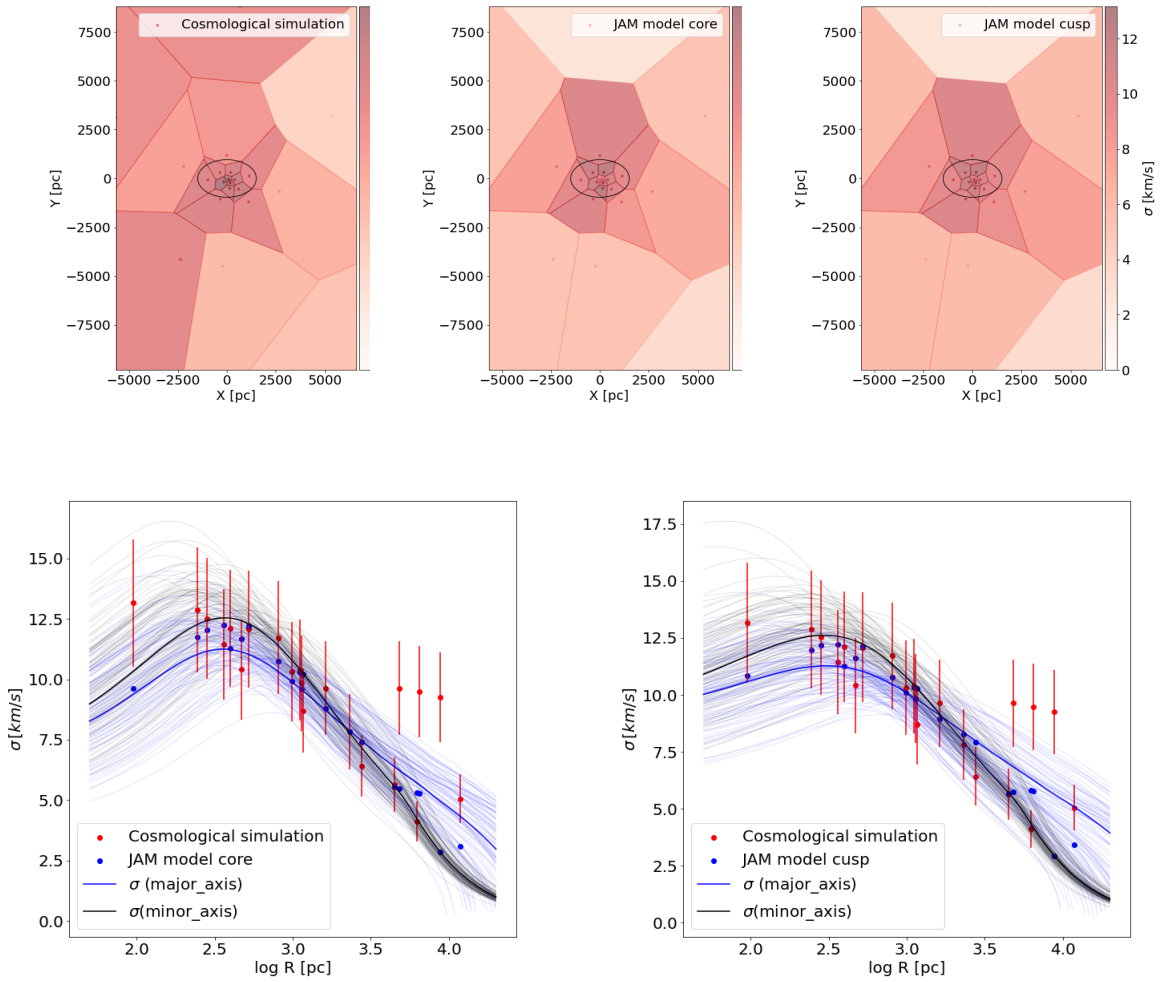

Figure 4.10: The figures above illustrate the galaxy's velocity dispersion: the top-left panel displays estimates from the cosmological simulation, the middle panel depicts the line-of-sight velocity dispersion predicted by the JAM model with a cored DM profile, and the top-right panel presents predictions with a cusped DM profile. The bottom panels show velocity dispersion along the major (blue lines) and minor (black lines) axes obtained from the posterior distribution, with thick solid lines representing the median model.

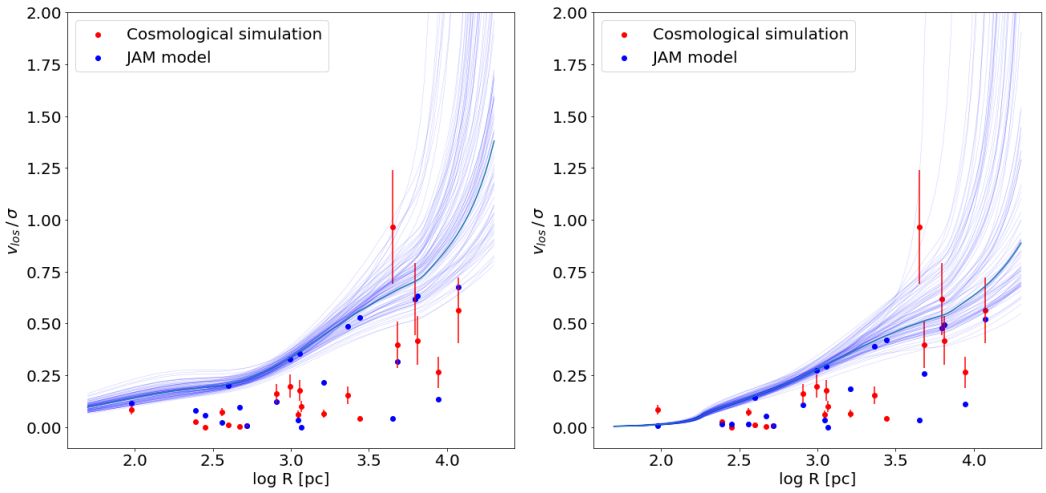

Figure 4.11: v_{los}/σ diagram of the galaxy at its oblate rotation phase from the JAM models: core (left), cusp (right). Red and blue dots represent the observed and modeled values in the respective Voronoi bins. The blue lines show the posterior distribution of the v_{los}/σ along the major axis.

our model in capturing the galactic mass. Fig. 4.12 highlights the comparison between the predicted mass from the JAM model and the mass obtained from the cosmological simulation. Notably, the JAM model demonstrates good agreement with the simulated mass within the half-light radius of the galaxy. However, discrepancies become apparent in the outer regions.

The discrepancies observed in the outer regions of the galaxy between the predicted and simulated masses could indeed be attributed to multiple collisions between the galaxy and its satellite halos during the considered time period. These collisions may have led to an increase in the galaxy's mass, influencing its dynamics. Comparisons between modeled and simulated masses provide valuable insights into the validity of dynamical modeling approaches and their ability to accurately reproduce the fundamental properties of galaxies.

In Fig. 4.12, we have plotted and compared the predicted mass profiles from two different models that were fitted for this stage of the galaxy. We observe that the mass predicted by the core model shows a more promising agreement with the observed mass distribution in the inner core of the galaxy. On the other hand, the cusped model fails to accurately predict the total mass of the galaxy, even in the inner regions. The cusped model predicts slightly higher mass at the half-light than the cored model.

The comparison between the modeled mass profiles and the mass derived from the cosmological simulation provides insights into the accuracy and validity of our models in capturing the galactic mass. While the core model performs relatively better in reproducing the mass distribution within the inner core, both models show discrepancies in predicting the total mass of the galaxy at larger radii.

These findings highlight the complexity and challenges associated with modeling the mass profile of galaxies. It suggests that alternative models or additional physical processes may need to be considered to improve the accuracy of mass predictions, particularly in the outer regions of the galaxy.

Indeed, further investigations and refinements in the models are essential to better understand the underlying physics and to develop more accurate representations of the mass distribution in galaxies. The study of galaxy formation and evolution is a complex and evolving field, and continuous efforts are necessary to advance our knowledge. By gaining deeper insights into the fundamental properties of galaxies, we can

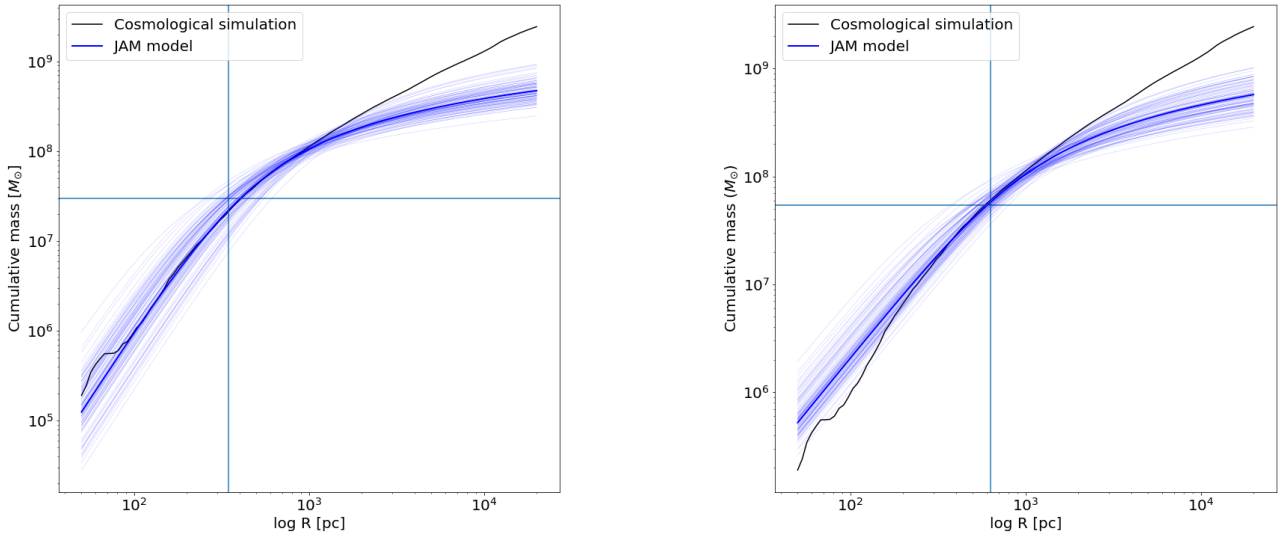

Figure 4.12: Comparison of the best-fitted mass profiles obtained from the JAM model with the cosmological simulation. The figures show the cored DM density profile (left) and cusped DM density profile (right) models. The blue horizontal and vertical line represents the half-light radius and virial mass of the system calculated from the modeled line-of-sight velocity dispersion and the half-light radius, following the method outlined in (Wolf et al., 2010).

uncover the very complicated processes that shape their dynamics and evolution. Such research not only contributes to our understanding of the universe but also has implications for broader cosmological and astrophysical studies.

4.3 Prolate Rotation

During the evolutionary process of the galaxy, significant mergers occur between the host galaxy and its satellite galaxies. These mergers involve the transfer of angular momentum, which can result in the galaxy rotating around its major axis (Amorisco et al., 2014). This particular stage of the galaxy's evolution presents an intriguing opportunity to test the effectiveness of dynamical models.

Approximately 7.5 billion years ago in the simulation ($z \simeq 0.86$), the galaxy experienced a significant merger event with a halo that had a mass approximately one-fifth that of the galaxy. This massive merger had a profound impact on the kinematic properties of the galaxy, resulting in a notable alteration. Specifically, the galaxy transformed into a prolate rotator, indicating that its rotation became around its major axis as a consequence of this merger event (Cardona-Barrero et al., 2021).

What is particularly intriguing is that after the alteration of the galaxy's rotation axis, it exhibits remarkable stability and continues to rotate predominantly around its major axis. This stable rotation suggests that the dynamics of the galaxy have settled into a state where the major axis serves as the primary axis of rotation (see in Fig. 4.13). The angle (θ) between the stellar angular momentum vector and the orientation of the principal axes of the ellipsoid provides insights into the evolution of the galaxy's rotation. When observing the blue curve, representing the angle between the stellar angular momentum and the principal minor axis,

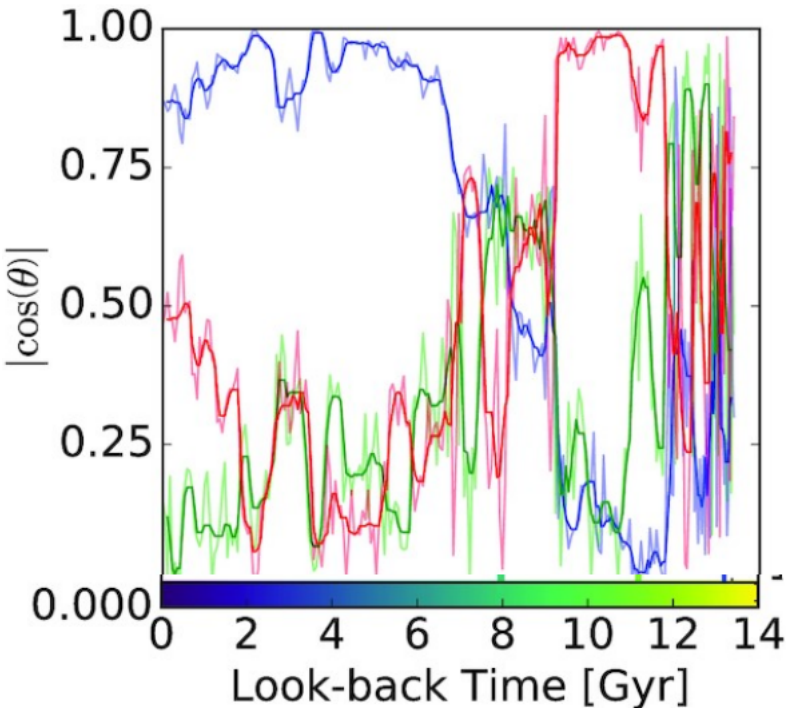

Figure 4.13: Principal axes orientation concerning the stellar angular momentum as a function of look-back time. Major, minor, and intermediate axes are represented by blue, red, and green, respectively. Thin lines indicate values from individual snapshots, while thick lines show the running average using a window of six snapshots ($\sim$ 0.34 Gyr) Cardona-Barrero et al., 2021.

it shows the galaxy initially rotating along the major axis, evidenced by a cosine of angle approaches to 0, indicating perpendicular alignment. However, approximately 8 Gyr ago, this angle began to change, coinciding with a merger event involving a satellite halo. Subsequently, the cosine of the angle approaches 1, signifying that these axes become parallel. This alignment indicates that the rotation axis is now parallel to the major axis of the galaxy and it continues to the present day.

This persistence of rotational behavior around the major axis highlights the long-term stability and quasi-dynamical equilibrium achieved by the galaxy following the significant merger event.

4.3.1 Dynamical Model of the galaxy at $z \simeq 0.58$

We applied the Jeans dynamical model to the galaxy shortly after the merger event, specifically at a redshift of $z \simeq 0.58$ (see in Fig. 4.14). During this phase, the galaxy was assumed to be in a quasi-equilibrium state, indicating that its dynamical properties had reached a relatively stable configuration following the merger.

In this phase of the galaxy's evolution, we explored both cored and cusped DM profiles as possible options for the potential in our models. But in addition we also introduced a model variation by considering different values of α, β, and γ (outer, intermediate and the inner slope) of the generalised Herniquist DM profile described in Equation 4.1 to determine the best-fitted mass profile obtained from the cosmological simulation. This approach allowed us to explore the sensitivity of the mass profile to variations in the DM halo parameters and assess the model's capability to accurately capture the galaxy's mass distribution.

The JAM modelling technique is analogous to the one described in section (4.2). The fitted parameters utilizing the cored NFW central density, scale radius, velocity anisotropy, and rotation of the galaxy, are

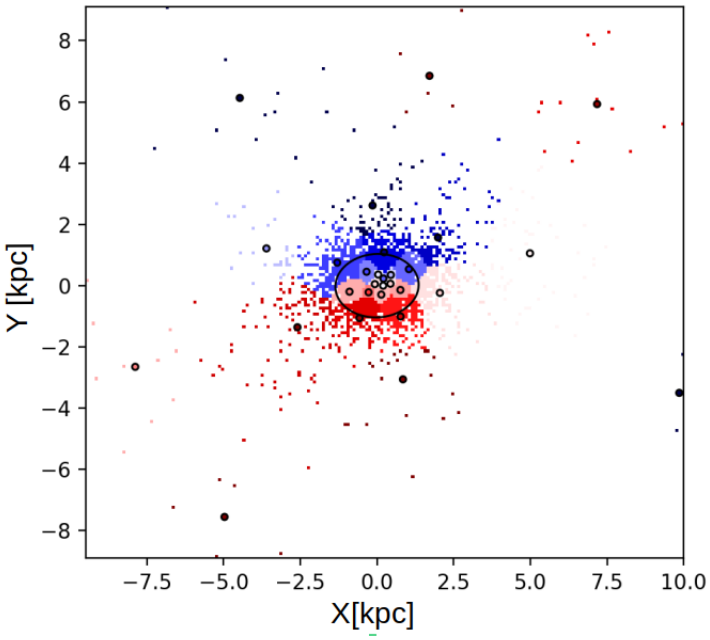

Figure 4.14: The image depicts a velocity map of the galaxy captured at a redshift of $z = 0.58$. Notably, the map illustrates a noticeable rotational motion aligned with the galaxy's major axis. In the visualization, smaller dots denote the particle positions derived from the cosmological simulation, while larger dots represent the Voronoi binned data points.

displayed in Fig. 4.15. These parameters provide valuable insights into the dynamics of the galaxy and its DM distribution.

In contrast to the previous scenario of oblate rotation, in this case, we observed a negative anisotropy (β_z) in the galaxy's dynamics, indicating a prolate velocity ellipsoid. This suggests that the galaxy's random motion is elongated along its major axis. Despite attempts to solve the Jeans equations using an oblate velocity ellipsoid, we were unable to obtain such solutions for the second velocity moments of the galaxy. This highlights the novelty of our findings, as it suggests that only a prolate velocity ellipsoid is feasible in this scenario, a hypothesis that has not been previously tested.

Our second model employs the cusped DM profile, using the same kinematics as above, to solve the Jeans equations. The corresponding fitted parameters are displayed in the corner plot (Fig. 4.16). This model exhibits similar values for the galaxy's anisotropy and rotation parameters, but the scale radius and central density of the galaxy are slightly higher compared to the cored model.

For our last dynamical model, we attempted to fit the generalized Hernquist profile as the DM profile to assess which profile best describes the dynamics of the galaxy. We employed Equation 4.1 and utilized the mass profile obtained from the cosmological simulation to constrain the parameters describing the DM profile, including the intermediate and outer slopes α, β, and γ, as well as the central density r_0 and the scale radius r. The fitted parameters are displayed in Fig. 4.18. This approach allowed us to directly incorporate the specific mass distribution derived from the cosmological simulation, providing a more accurate representation of the galaxy's mass profile in our dynamical modeling (see the fitted mass profile in Fig. 4.17).

Using the fitted DM profile, we once again utilized the kinematics obtained from the cosmological simulation to solve the Jeans equations. We fitted the central density of the galaxy, its scale radius, velocity

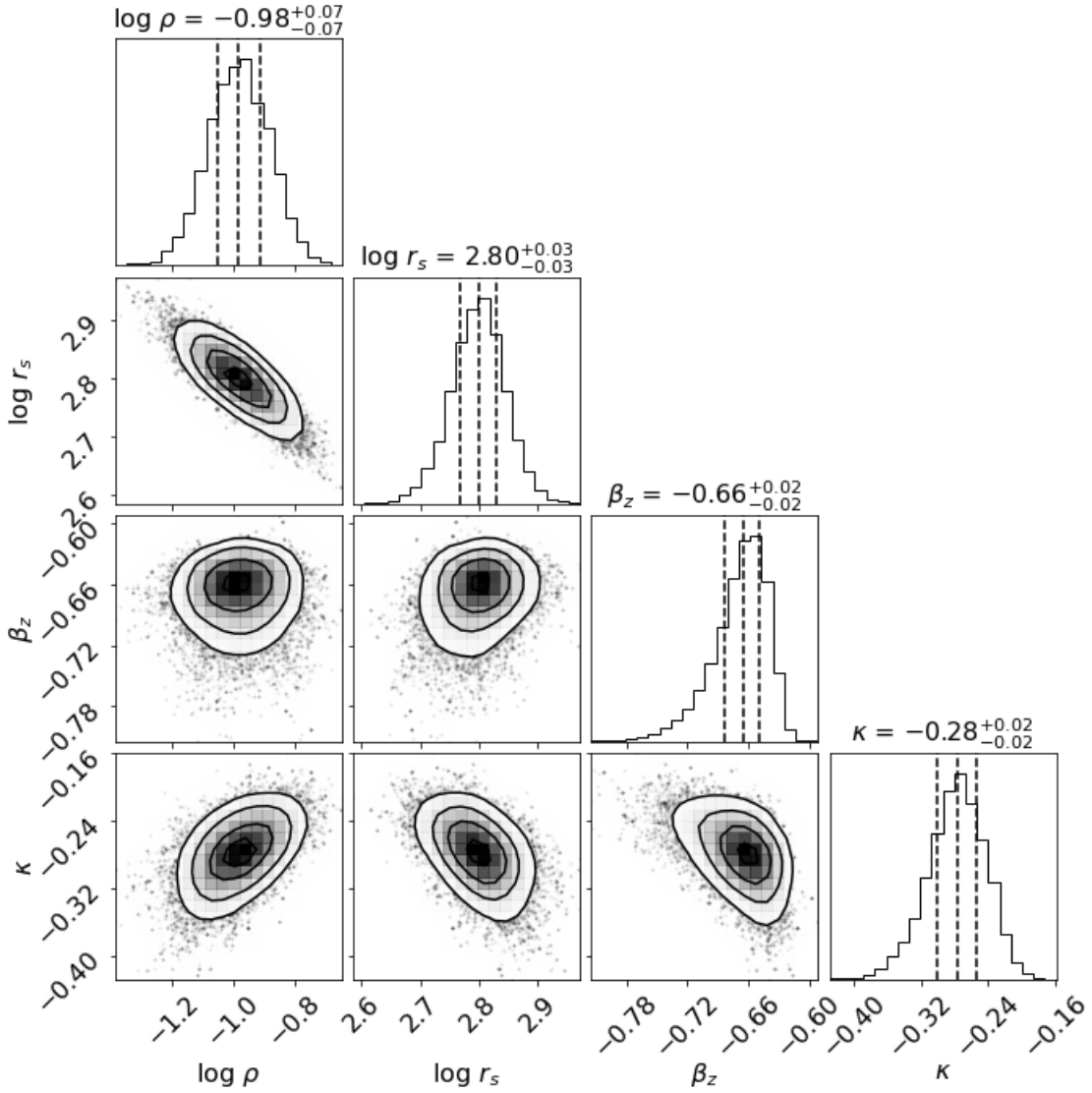

Figure 4.15: Posterior distributions and covariance matrices are obtained from our MCMC analysis, derived for the parameters employed in fitting the JAM model using a cored NFW profile. These parameters comprise the logarithm of the central density and scale radius ($\log \rho$) and ($\log r_s$) for the DM halo, as well as the anisotropy (β_z) and rotation (κ) factors governing the galaxy's dynamics. The contours illustrate the 1, 2, and 3σ constraints for each parameter.

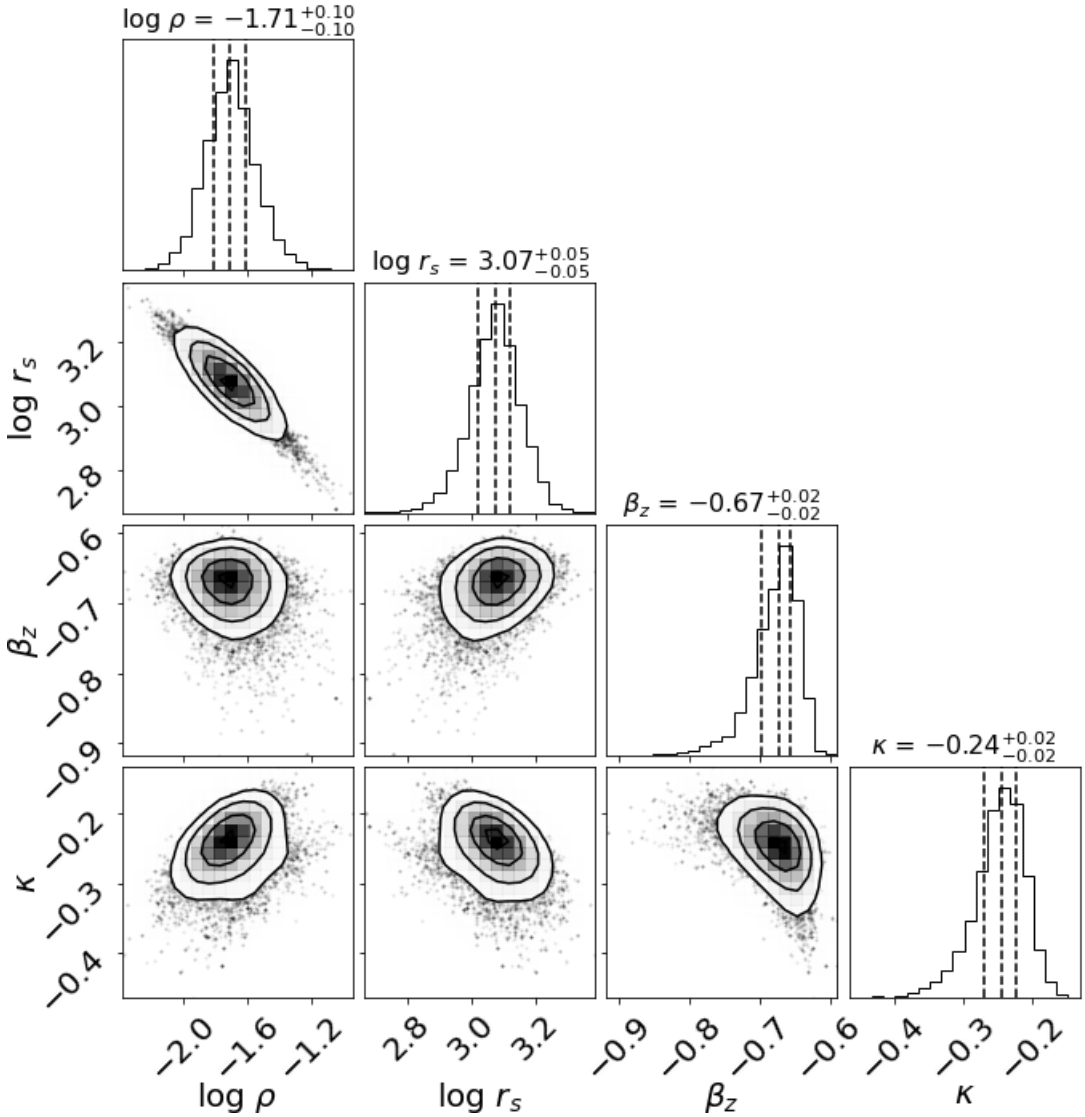

Figure 4.16: The same as Fig. 4.15, however, for the cusped NFW DM profile.

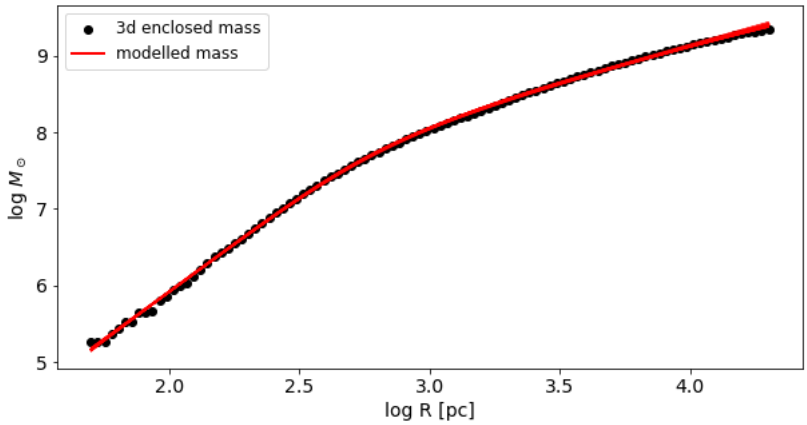

Figure 4.17: Cosmological mass vs modelled mass using equation 4.1, using the fitted parameters shown in Fig. 4.28.

anisotropy, and rotation parameters, as shown in the corner plot (Fig. 4.19). The JAM model incorporated these fitted parameters to calculate the line-of-sight velocity and velocity dispersion profiles of the galaxy.

In all these three different density profiles, only negative anisotropy (β_z) gave the feasible solution to the Jeans equations, which means the velocity ellipsoid of the galaxy is prolate.

In Fig. 4.20, we present a comparison of the fitted density profiles of the galaxy using the JAM model. The differences between the three different density profiles are evident, particularly in the inner and outer regions of the galaxy. While the cored and cusped DM profiles exhibit similar density profiles in the outer regions, the generalized Hernquist profile predicts a slightly higher density. However, in the inner region of the galaxy, all three models predict significantly different densities, which can have a significant impact on the dynamics of the galaxy.

In Fig. 4.21, we present a comparison of the line-of-sight velocity v_{los} obtained from three different JAM models using different DM profiles. The top two rows show the 2D histogram for the first velocity moment calculated from the JAM code. The v_{los} values from the three models are almost identical, with only slight discrepancies observed at the outskirts of the galaxy.

The analysis of the line-of-sight velocity along the X-axis (minor axis) in the last row of Fig. 4.21 provides further confirmation. The plot shows a clear rotation of the stellar particles along the minor axis, indicating prolate rotation. The solid line represents the median v_{los} profile of the galaxy, while the thin curves represent random draws from the posterior distribution. This prolate rotation pattern aligns with our previous study done by Cardona-Barrero et al. (2021) and contributes to a better understanding of the dynamics of the galaxy.

Using the fitted parameters, the second velocity moment, directly related to the velocity dispersion of the galaxy, can be calculated. The velocity dispersion obtained with different potentials in solving the Jeans equations is then compared with reference data derived from the cosmological simulation to determine which model best describes the velocity dispersion of the galaxy. (see in Fig. 4.22)

In Fig. 4.22, we present the comparison of the velocity dispersion obtained from the cored, cusped, and generalized DM halo profiles with the reference data from the cosmological simulation. The 2D projection plot of the velocity dispersion along the minor and major axes reveals that the cored and cusped DM pro-

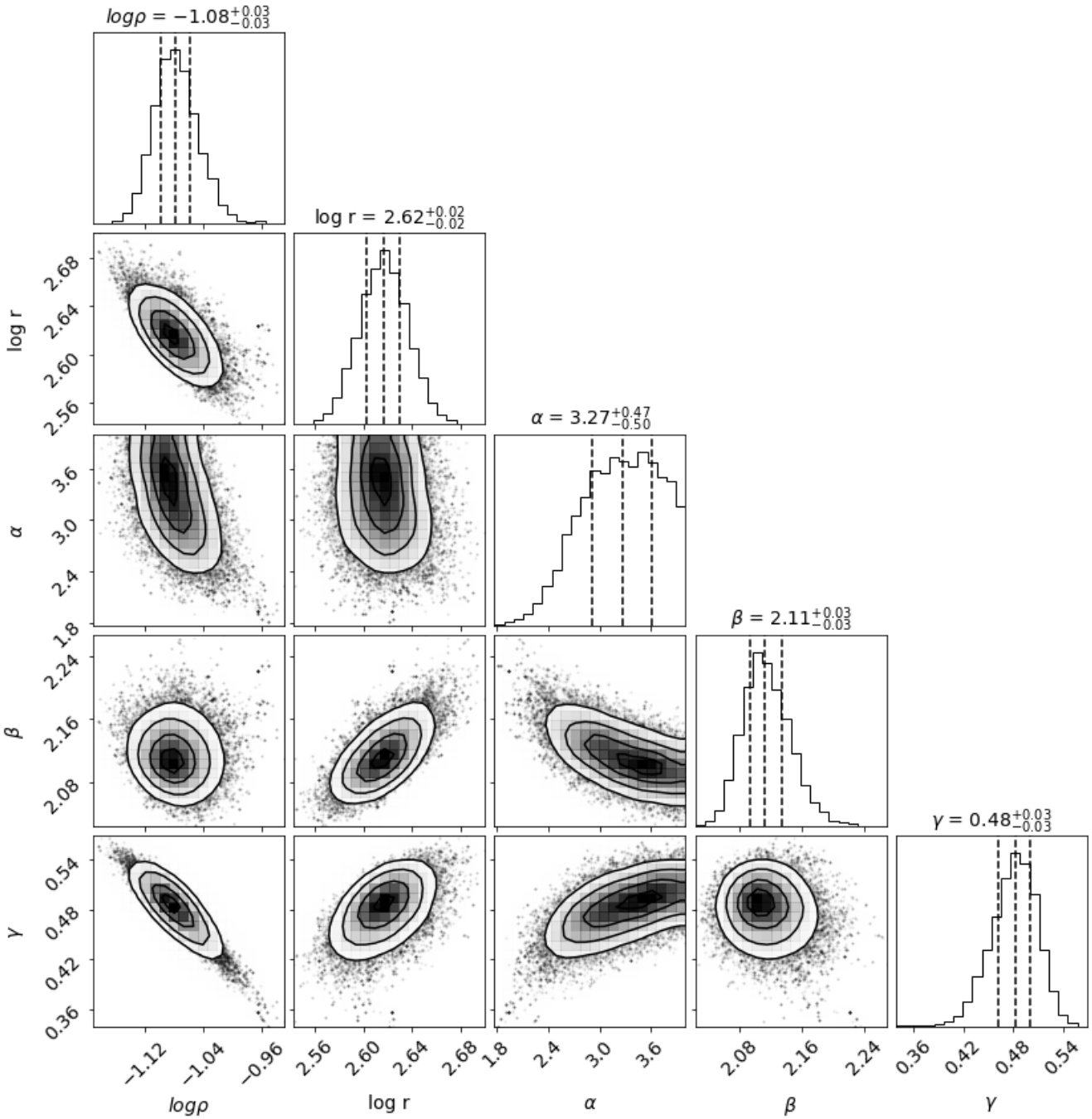

Figure 4.18: Corner plot displaying the posterior distributions of the fitted density profile parameters for the galaxy, obtained through MCMC analysis. The fitted parameters include the logarithmic central density ($\log \rho$), logarithmic scale radius ($\log r_s$), and the slopes of the density profile (α, β, γ) outlined in Equation 4.1. The contours represent the 1σ, 2σ, and 3σ constraints of the fitted parameters.

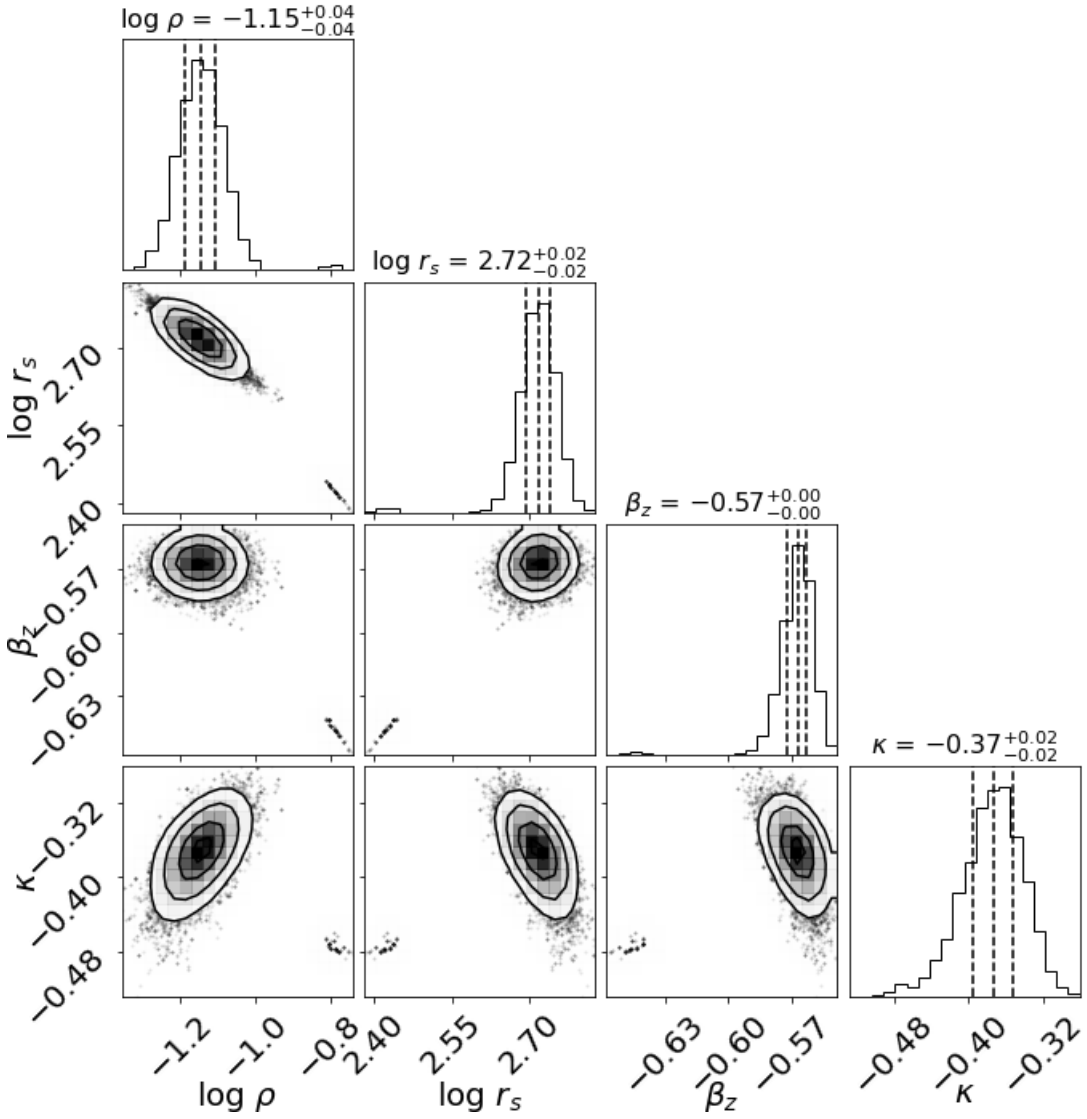

Figure 4.19: We apply a generalized Herniquist profile, using above-fitted parameters shown in Fig. 4.18, to fit the JAM model, and the results of our MCMC analysis yield posterior distributions and covariance matrices. Together with the anisotropy (β_z) and rotation (κ) factors controlling the galaxy's dynamics, these parameters include the logarithm of the central density and scale radius ($\log \rho$) and ($\log r_s$) for the DM halo. The 1, 2, and 3σ restrictions for each parameter are depicted by the outlines.

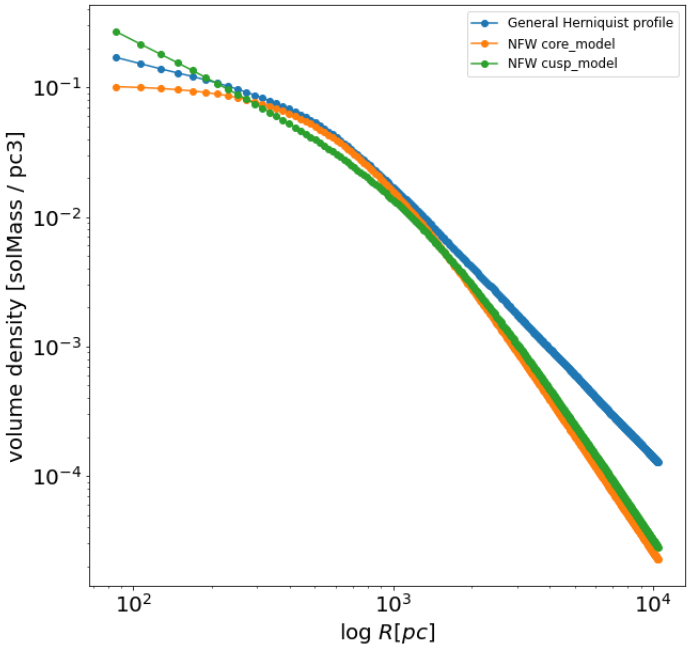

Figure 4.20: Comparison of the density profiles modeled with fitted parameters derived from dynamical modeling, representing the cored, cusped NFW DM models, and the generalized Hernquist model.

files produce almost identical velocity dispersion, while the generalized DM halo predicts a lower velocity dispersion for the galaxy. This analysis allows us to assess the accuracy of each model in describing the velocity dispersion of the galaxy.

The rotational velocity of the galaxy is relatively low compared to the velocity dispersion. This indicates that the galaxy is primarily supported by pressure rather than ordered motion along a specific axis. The presence of significant random velocities along different axes contributes to the pressure support and makes the system against the gravitational collapse. In the context of galaxies, pressure support can come from the random motion of gas and stars, which creates pressure that counteracts the gravitational pull of the galaxy's mass. This can be an important factor in determining the overall dynamics and stability of a galaxy.

Pressure support in galaxies can be maintained over long timescales because when gas is converted into stars, any reduction in support is balanced by an inward flow of gas (Dalcanton & Stilp, 2010). This continuous cycle of gas inflow and star formation helps to sustain the overall pressure within the galaxy, allowing it to maintain its structural integrity and stability over time.

Indeed, all three models successfully reproduce the line-of-sight velocity distribution of the galaxy. However, when it comes to the velocity dispersion, the cored and cusped models perform relatively well, while the generalized DM halo model predicts a lower velocity dispersion. This suggests that the generalized DM potential might not be able to fully capture the dynamics of the galaxy, and the cored and cusped models provide a better fit to the observed velocity dispersion data.

In this stage of the galaxy's evolution, we achieved a significantly improved fit for the line-of-sight velocity and velocity dispersion when compared to the previous case of oblate rotation. The dynamical model employed was able to accurately reproduce the observed data, indicating a better agreement between the model

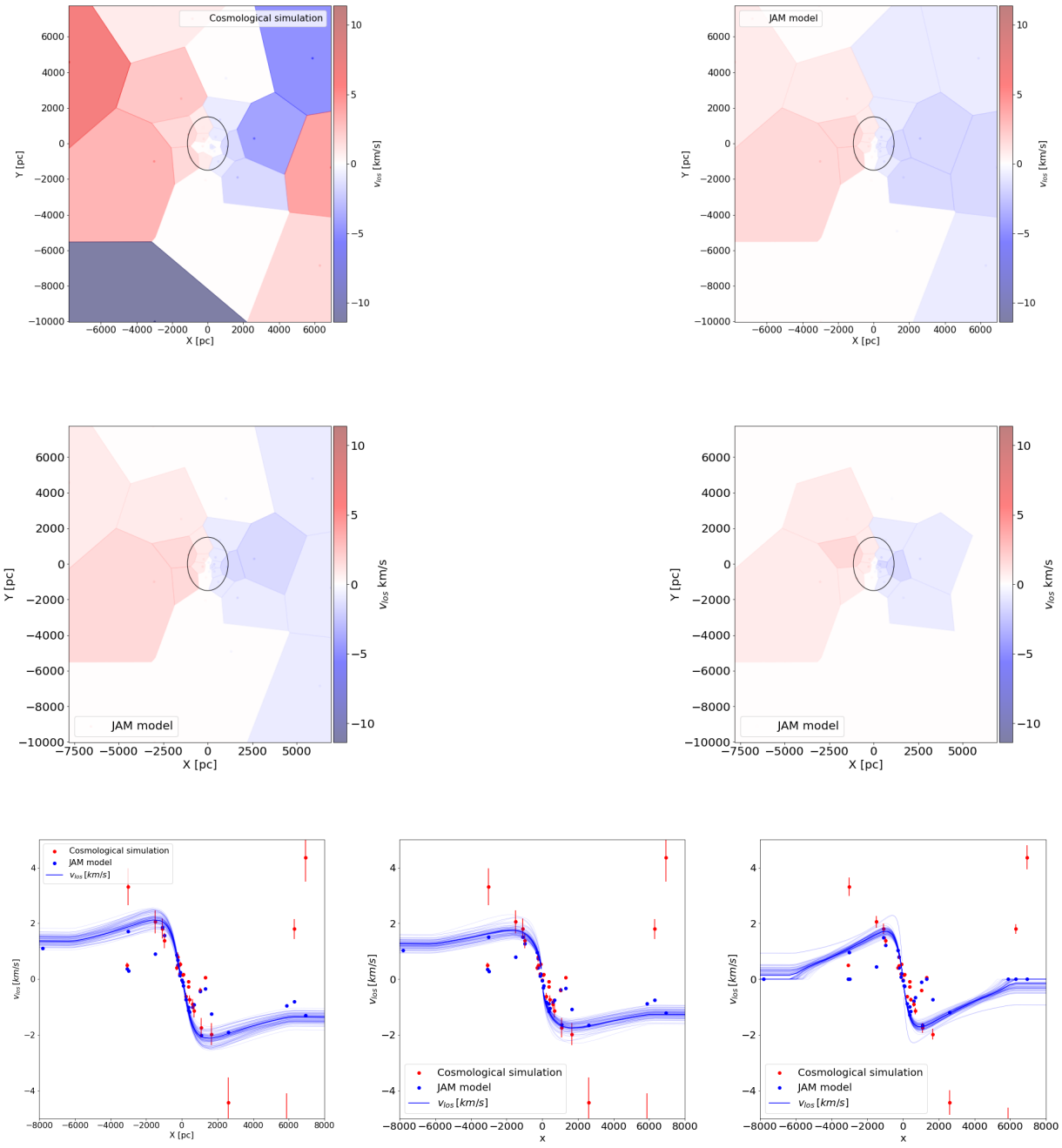

Figure 4.21: Comparison of the 2D line-of-sight velocity of the galaxy obtained from the cosmological simulation (top left) and the line-of-sight velocity dispersion predicted by the JAM model using different DM profiles, including cored (top right), cusped (middle left), and generalized DM halos (middle right). The black ellipses represent the half-light radius of the galaxy. The lower panel displays the 1D line-of-sight velocity profiles for all three models.

predictions and the actual kinematic properties of the galaxy, both in the inner core and in the outskirts.

As seen in Fig. 4.23, the $v_{\rm los}/\sigma$ ratio is notably lower compared to the oblate rotation phase depicted in Fig. 4.11. This suggests that, at this stage, the galaxy was primarily influenced by pressure forces, leading to an increase in randomness. This effect is observed for both cored and cusped NFW dark matter profiles, compared to the generalized NFW dark matter profile.

The effect of a merger is a plausible explanation for these observations. Mergers can significantly disrupt the structure and dynamics of galaxies, often leading to an increase in random motion and pressure forces that can dominate over rotational motion, especially in the central regions. This can result in a more pressure-dominated, spheroidal structure (Nipoti et al., 2003).

The distribution of matter in cosmological structures plays a crucial role in shaping the evolution and dynamics of galaxies and galaxy clusters. Mass is a fundamental property of these systems, and it strongly influences their formation, growth, and interactions. Understanding the mass distribution within these structures is essential for studying their evolution, the processes of star formation, the growth of black holes, and the overall large-scale structure of the universe (Courteau et al., 2014).

Based on the dynamical model discussed above, we can estimate the mass profile of the entire galaxy. The results indicate that the mass predictions from the JAM model are generally in good agreement with the mass profile obtained from the cosmological simulation, particularly within the inner regions of the galaxy.

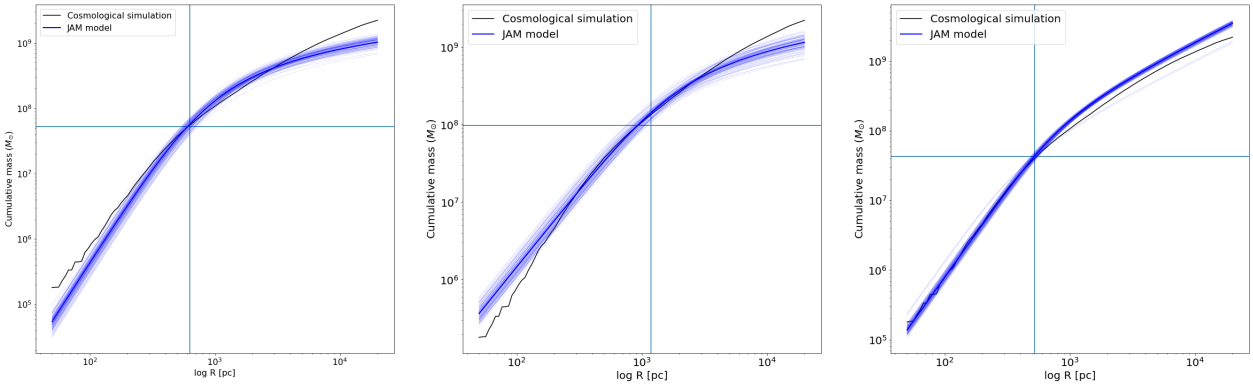

Figure 4.24: Comparison of dynamical mass estimates derived from JAM models with observations obtained from the cosmological simulation. Shown are the cored density profile (left), cusped density profile (middle), and a generalized Hernquist halo (right). The blue lines indicate the virial mass (calculated according to the method detailed in Wolf et al. (2010)), while the vertical lines represent the half-light radius of the modeled system.

The plots in Fig. 4.24 provide interesting insights into the mass distribution of the galaxy as predicted by different models. The core model shows a slight deviation in the very inner core of the galaxy compared to the simulated mass, but it closely matches the simulated mass at the half-light radius. In contrast, the cusped profile predicts a slightly higher mass in the inner core. However, despite these differences in the inner regions, both models yield similar total mass estimates for the galaxy. This suggests that while there may be some variations in the mass distribution within the galaxy, the overall mass content remains consistent between the models and the cosmological simulation. These findings are crucial for understanding the dynamics and evolution of galaxies and provide valuable insights into the reliability of the models used in

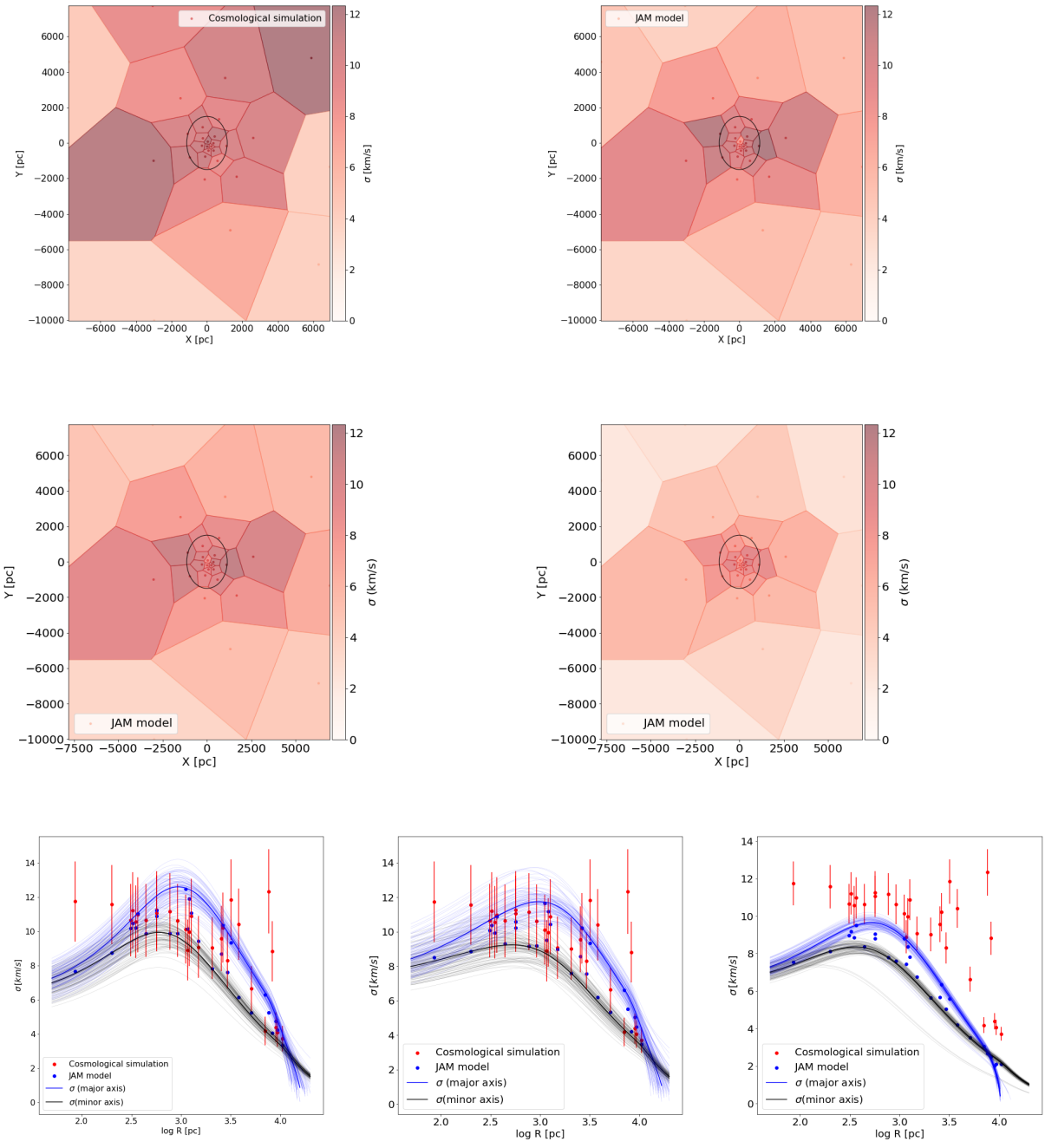

Figure 4.22: The figures present the 2D velocity dispersion estimates obtained from different models and simulations: the cosmological simulation (top left), the line-of-sight velocity dispersion predicted by the JAM model using a cored DM profile (top right), a cusped DM profile (middle), and a generalized Hernquist density profile (bottom). The lower panel illustrates the 1D velocity dispersion along both the major and minor axes.

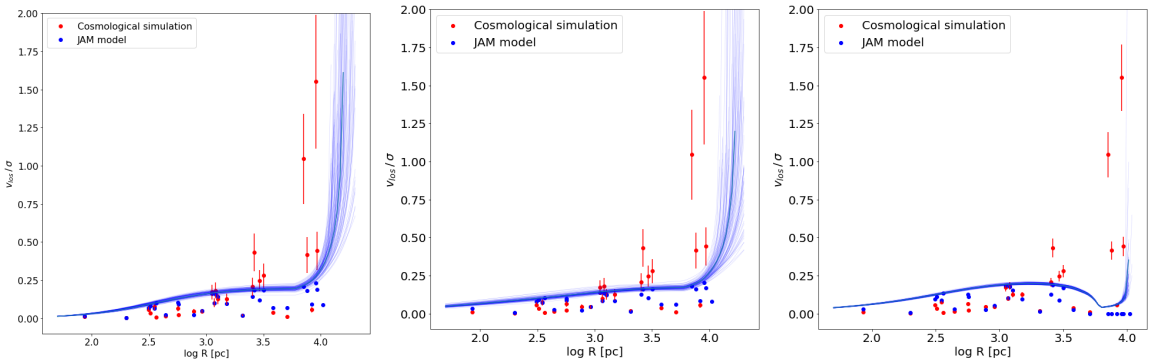

Figure 4.23: v_{los}/σ diagram of the galaxy at $z = 0.58$ calculated from the JAM models: cored DM (left), cusped DM (middle), and generalised DM (right) . Red and blue dots represent the observed and modeled values in the respective Voronoi bins. The blue lines show the posterior distribution of the v_{los}/σ along the minor axis.

our study.

Indeed, the generalised DM halo model shows promising results in predicting the mass of the galaxy, as it closely matches the simulated mass from the cosmological simulation. However, it falls short in reproducing the kinematics of the galaxy, despite using the kinematics as the initial condition for our model. This discrepancy indicates that the generalised DM halo model may not be suitable for accurately describing the dynamics of the galaxy. It highlights the importance of carefully choosing the appropriate DM halo profile to capture the complex dynamics and evolution of galaxies.

4.3.2 Dynamical Model of the galaxy at $z \simeq 0.00$

Studying the present stage of a galaxy is crucial for understanding its dynamics and evolution. By comparing the observations of the present stage of a galaxy with theoretical models, scientists can validate and refine their models, and gain insights into the physical processes that shape galaxies.

In addition, studying the present stage of a galaxy can provide important information about its past and future evolution. By constraining different models with observations, scientists can learn about the distribution and properties of DM, which plays a key role in shaping the structure of galaxies. This information can also be used to compare real galaxies and to validate the simulation.

The present time ($z = 0.00$) is indeed the most significant stage in galaxy evolution. As mentioned earlier, at a lookback time of 7 Gyrs, the galaxy has already transformed its axis of rotation, aligning itself predominantly with the major axis (see in Fig 4.13). This shift in the rotation axis indicates a change in the galaxy's dynamics. Furthermore, even at present, the galaxy continues to exhibit prolate rotation, maintaining a rotational motion that is elongated along its major axis which can also be seen from the velocity map of the galaxy (see Fig. 4.25). The galaxy's pressure support ensures long-term stability, leading to its prolate rotation at the present stage.

We employed the photometry and kinematics acquired from the cosmological simulation as the input for our JAM model. Subsequently, we conducted three distinct JAM models, each assuming different gravitational potentials for the galaxy: i) cored DM, ii) cusped DM, and iii) generalised DM gravitational potential. Using these three different models, we analyzed and described the kinematics of the galaxy, as well as pre-

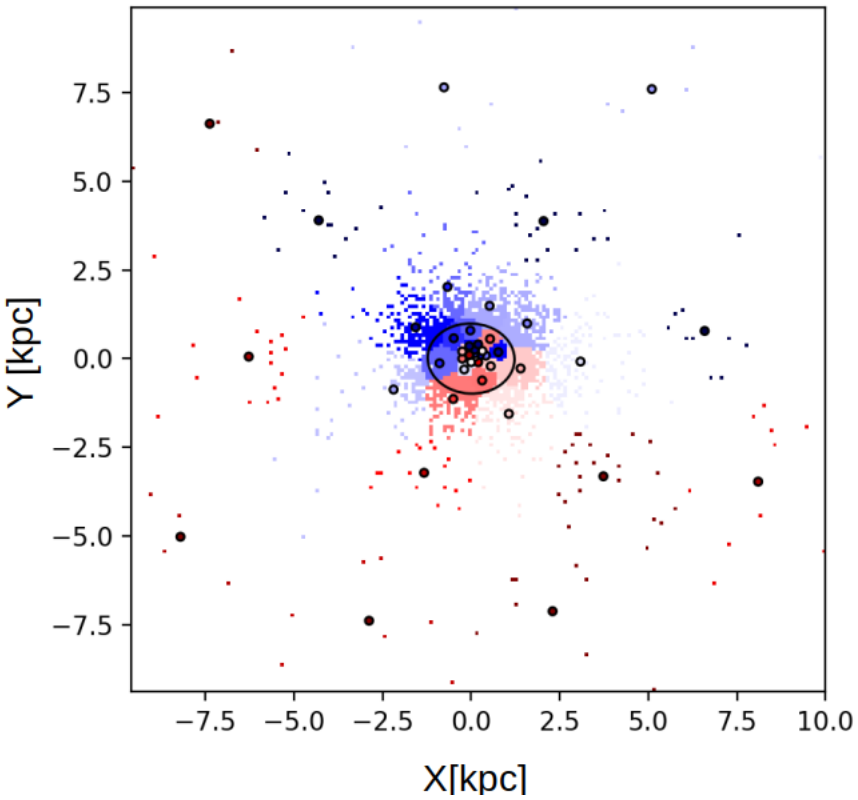

Figure 4.25: The image illustrates a velocity map of the galaxy at a redshift approximately $z \sim 0.00$. Notably, the map reveals a noticeable rotational movement along the galaxy's major axis. Smaller dots represent particle positions obtained from the cosmological simulation, while larger dots denote the Voronoi binned data points.

dicted its mass profile. By comparing the results of the three JAM models with the observed data from the cosmological simulation, we aimed to gain deeper insights into the dynamics and mass distribution of the galaxy and to understand the role of different DM halo profiles in shaping its properties.

Continuing our analysis, we extended the Jeans modeling to explore the dynamics of the galaxy at different stages in its evolution. After investigating the galaxy's behavior before and just after a major merger, we now examine its state several billion years post-merger. In all cases, we maintain the assumption that the galaxy is in a quasi-equilibrium state (where the galaxy is not undergoing any major changes on a short time scale), allowing us to further understand its current behavior and dynamics.

To conduct the dynamical modeling of the galaxy's present stage, we utilize input files derived from the cosmological simulation. These files provide us with essential data, including the galaxy's density distribution obtained from its surface brightness profile. Additionally, we obtain the mean line-of-sight velocity and velocity dispersion of the galaxy through Voronoi binning, as illustrated in Fig. 4.25, where the larger dots represent the Voronoi bins.

By analyzing the line-of-sight velocity and velocity dispersion, we were able to gain a better understanding of the galaxy's internal kinematics. The fitted models successfully reproduced the observed velocity distributions, indicating that they captured the underlying dynamics of the galaxy.

Building upon the aforementioned methodology, we have employed three distinct DM profiles to conduct the dynamical analysis of the galaxy at its current stage. Of particular significance is the cored DM profile,

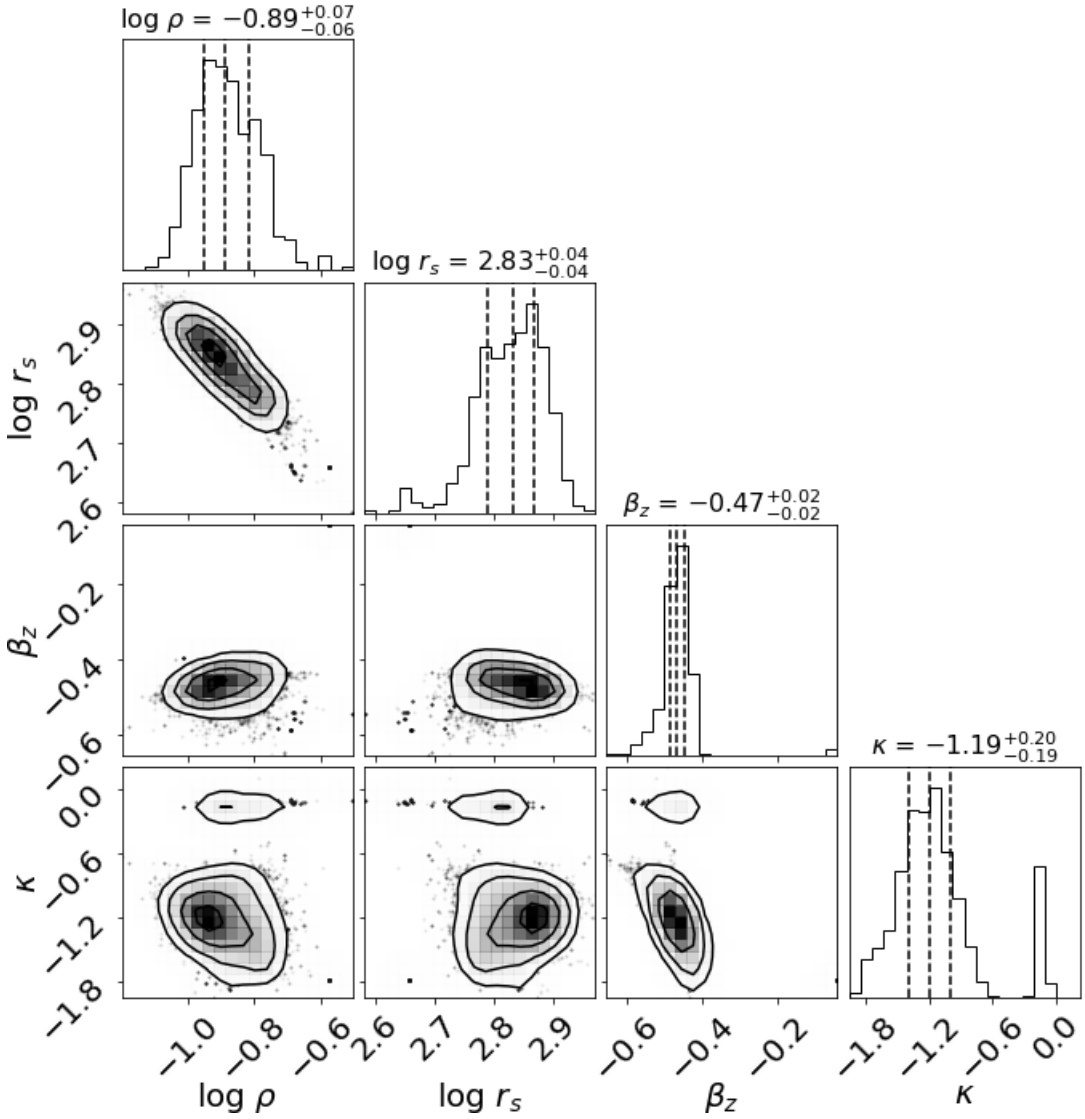

Figure 4.26: MCMC post-burn distributions depict the results of fitting a JAM model of the cored DM profile, and the solid lines show $1\,\sigma$, $2\,\sigma$, and $3\,\sigma$ regions of the projected covariance matrix. The fitted parameters are central density ($\log\,\rho$), scaled radius ($\log\,r_0$) for the DM halo and anisotropy (β_z), rotation (κ) for explaining the dynamics of the galaxy.

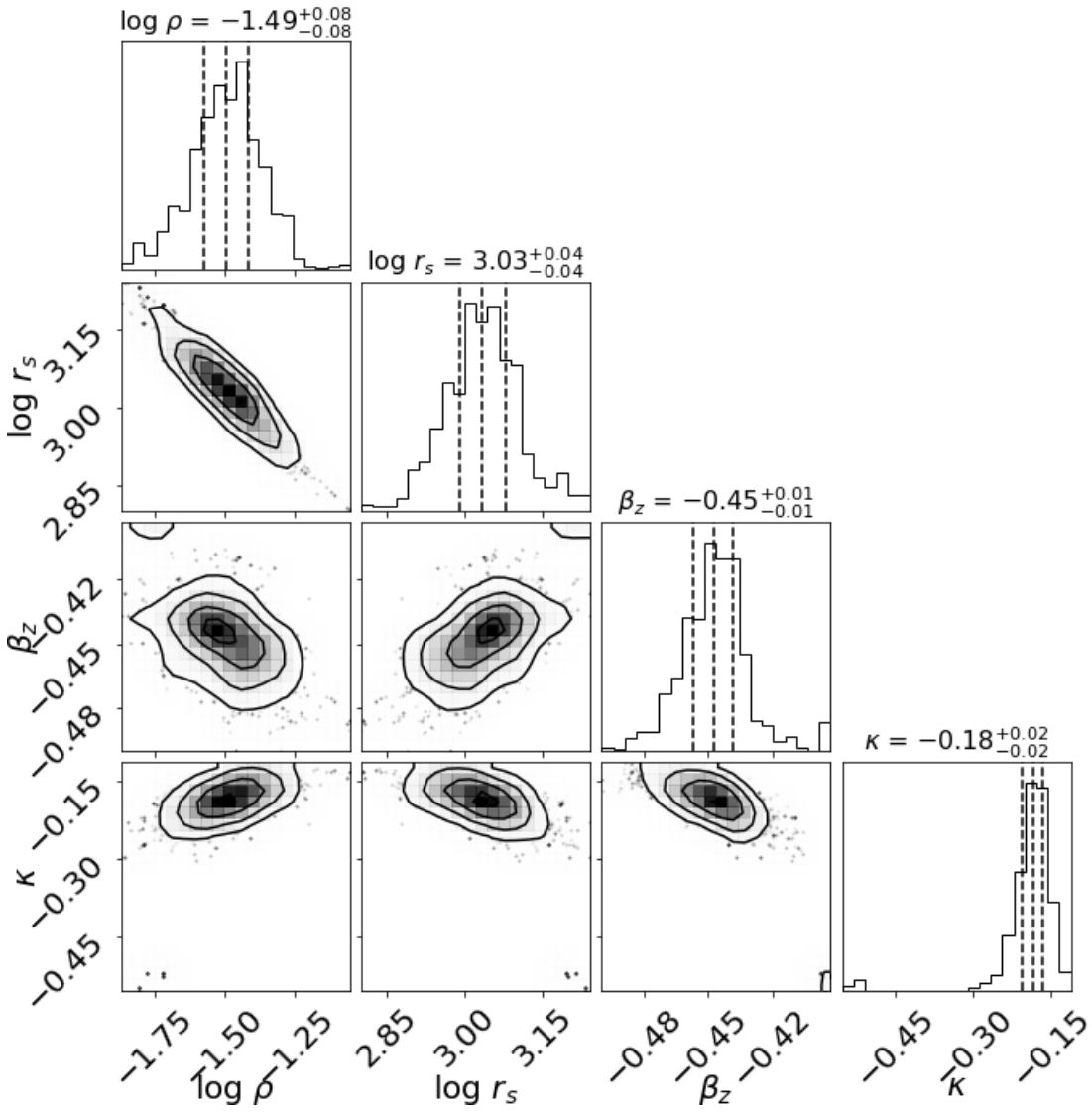

Figure 4.27: The same as Fig. 4.26, but for the cusped NFW DM profile.

with its corresponding fitted parameters illustrated in Fig. 4.26. It's noteworthy that we obtained a negative anisotropy for the galaxy, which signifies that the prolate rotation of the galaxy persists even at this stage. This finding provides valuable insights into the persistent rotational motion of the galaxy's stars.

Likewise, the fitted parameters derived from the dynamic modeling of the galaxy utilizing the cusped DM profile are presented in Fig. 4.27. Notably, this model exhibits a nearly identical anisotropy parameter for the galaxy. However, the rotation parameter is relatively smaller in comparison to the cored DM profile, indicating potential differences in the rotational motion of the galaxy's stars between the two profiles.

In this scenario, even after 7 Gyr, the velocity anisotropy (β_z) of the galaxy remains negative and shows little variation. This consistent negativity suggests that the velocity ellipsoid maintains its prolate nature, and only a prolate velocity ellipsoid yields viable Jeans models. This stability in the velocity anisotropy post-merger indicates a relatively stable system, with minimal changes in the velocity distribution over time.

Similarly to the previous snapshots, we followed the same approach to directly fit the mass distribution obtained from the cosmological simulation with the widely recognized Hernquist density profile. We assume that this profile can provide an accurate description of the DM and the density distribution within the galaxy,

potentially offering a more precise explanation for the galaxy's kinematics and dynamics.

We display in Fig. 4.28 the corner plot of the fitted parameters used to describe the density profile of the galaxy. These parameters include the central density of the DM halo, its scale radius, as well as the inner, intermediate, and outer slope of the halo. These values are crucial for accurately characterizing the galaxy's density distribution. The result of the fit is presented in Fig. 4.29.

Utilizing the fitted density profile based on the observed mass distribution, we conducted the dynamical modeling of the galaxy, following the same approach as before. The fitted parameters for the galaxy's dynamics are displayed in Fig. 4.30. These parameters are essential for understanding the kinematics and behavior of the galaxy at this specific stage in its evolution. Our analysis revealed the presence of negative anisotropy in all models, indicating a prolate velocity ellipsoid. This implies that the ordered motion within the galaxy predominantly occurs along the minor axis.

As we can see from the comparison with the other fitted galaxy models we see that the anisotropy of the galaxy is almost the same in all three models, but the central density and the scale radius are very different with the cored and cusped density profile which is demonstrated in Fig. 4.31.

We employed the JAM model with the same observational data and fitting parameters. The model utilizes these parameters as input to determine the line-of-sight velocity and velocity dispersion profiles of the galaxy. Subsequently, we plotted these profiles for visual comparison with the observed data. We compared the fitted first velocity moment with all three different DM halo profiles. The 2D velocity projections of all these different predictions are depicted in Fig. 4.32.

The top-left plot in Fig. 4.32 displays the cosmological simulation, while the others depict the predictions based on cored, cusped, and generalized DM profiles respectively. It's evident from these plots that all three different models provide an excellent fit within the galaxy's half-light radius. However, towards the outskirts of the galaxy, due to higher error counts in the surface brightness data, all three models exhibit relatively less accurate predictions compared to the cosmological simulation.

The cusped density profile model exhibits lower first velocity moments in comparison to the observed data, indicating an underestimation of the line-of-sight velocities. Nevertheless, it performs relatively better within the galaxy's half-light radius, suggesting that the cusped model is more effective at capturing the inner dynamics of the galaxy.

Similarly, the generalised Hernquist halo model preserves the first velocity moments quite well, as shown in the lower panel of Fig. 4.32. This suggests that the generalised Hernquist profile is capable of reproducing the velocity distribution of the galaxy, providing a reasonable fit to the observed line-of-sight velocities.

This is further supported by the 1D plot of the line-of-sight velocity calculated using dynamical modeling and the cosmological simulation shown in Fig 4.32. The dark solid blue line represents the line-of-sight velocity along the rotation axis, while the fainter solid blue lines represent the line-of-sight velocity distribution drawn from the posterior distribution of the MCMC fitting.

In Fig. 4.33, we analyze the second velocity moment, which is related to the velocity dispersion, predicted by the three different models and compare them with the results obtained from the cosmological simulation. Both the cored and cusped density models exhibit a strong agreement with the observed velocity dispersion profile, closely matching the dispersion values derived from the cosmological simulation.

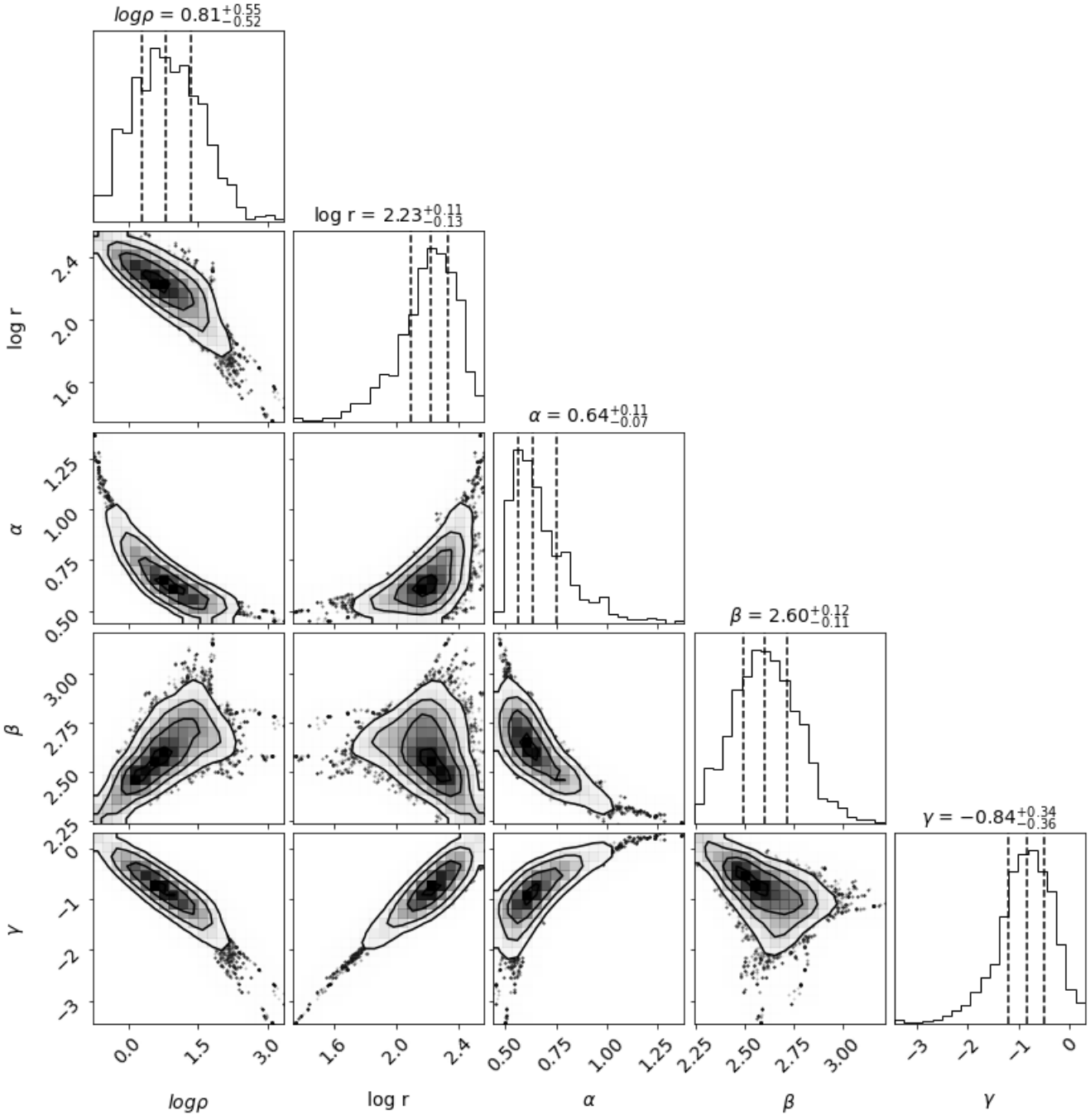

Figure 4.28: Corner plot illustrating the posterior distributions of the derived density profile parameters for the galaxy, acquired via MCMC analysis. The fitted parameters encompass the logarithm of the central density ($\log \rho$), the logarithm of the scale radius ($\log r_s$), and the slopes defining the density profile (α, β, γ) outlined in Equation 4.1. Contours within the plot outline the 1, 2, and 3σ boundaries, showcasing the constraints of the fitted parameters.

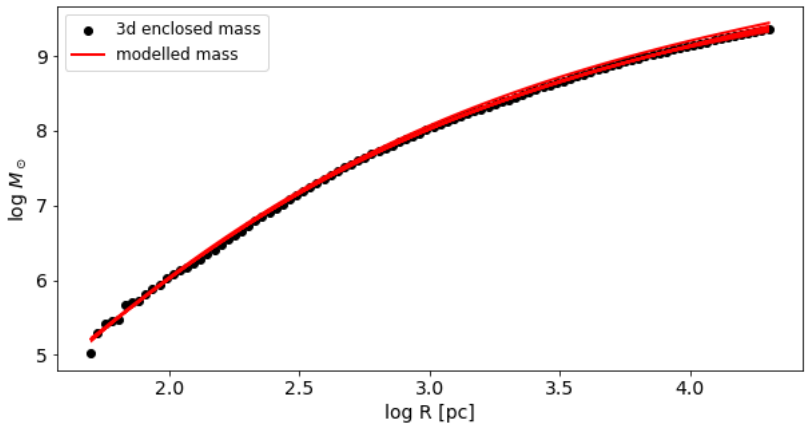

Figure 4.29: A generalized Hernquist profile using the parameters obtained from a direct fit to the simulated mass distribution shown in Fig. 4.28.

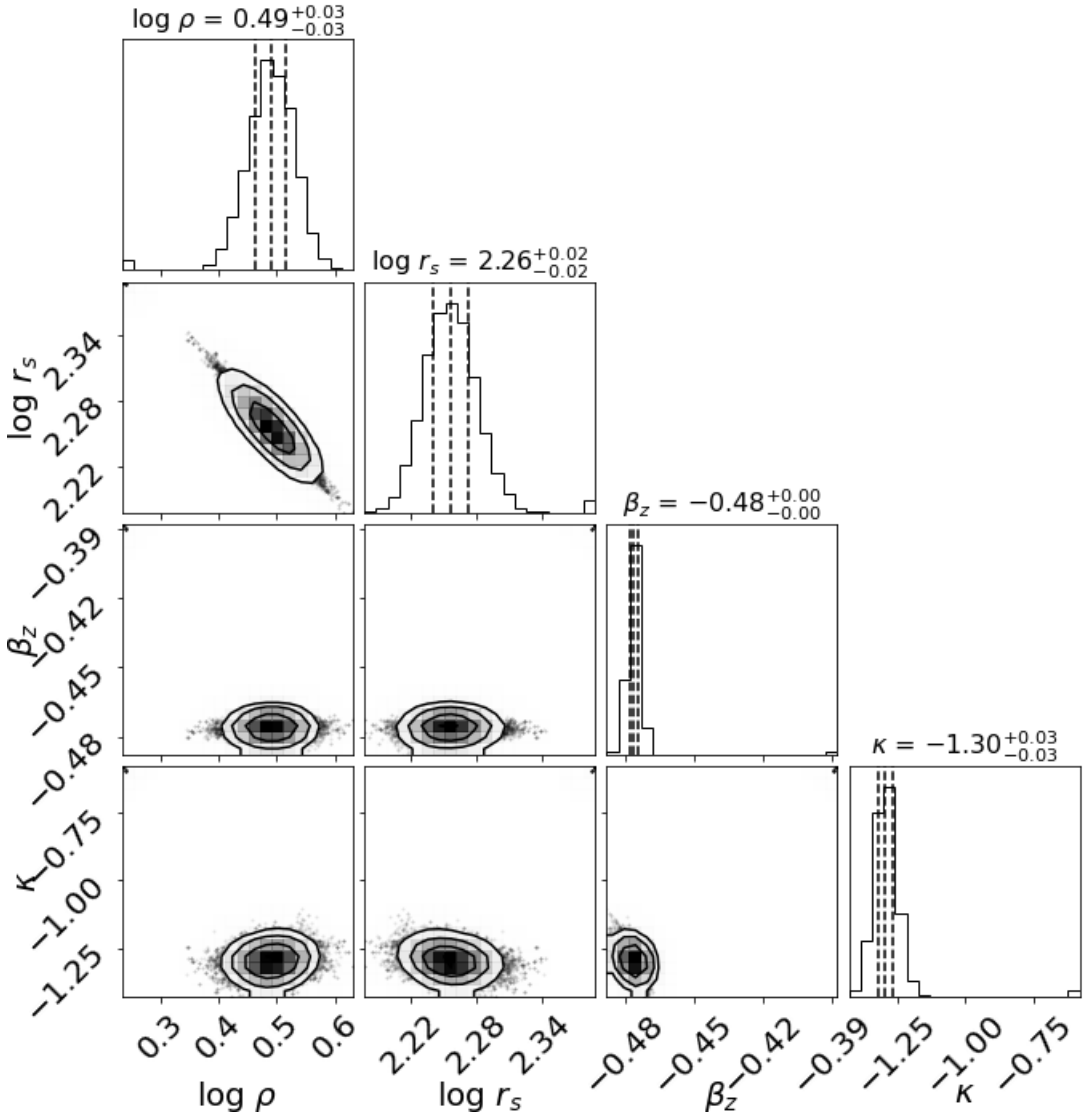

Figure 4.30: We utilize the parameters obtained from Fig. 4.28 to fit the JAM model with a generalized Hernquist profile. Subsequently, the MCMC analysis yields posterior distributions and covariance matrices. These parameters, encompassing the logarithm of the central density and scale radius ($\log \rho$, $\log r$) for the DM halo, in addition to the anisotropy (β_z) and rotation (κ) factors governing the galaxy's dynamics, are shown with their respective 1, 2, and 3σ boundaries in the figures.

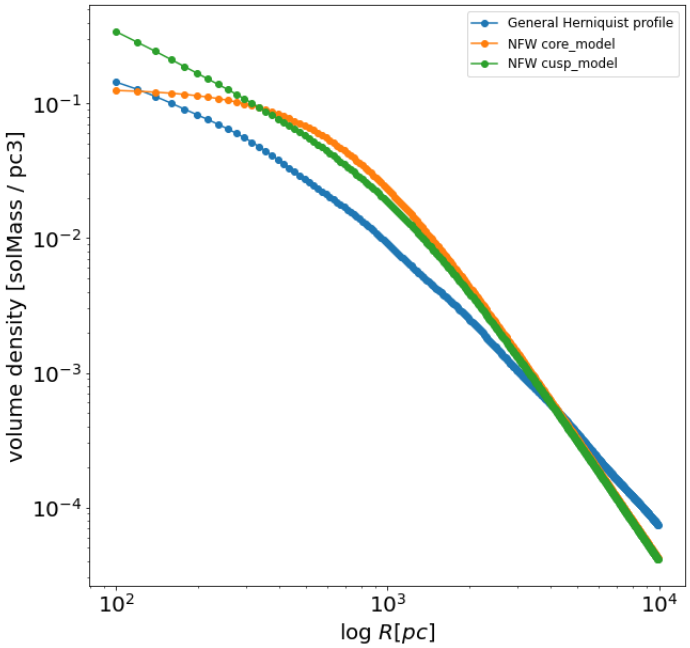

Figure 4.31: Density comparison of the fitted NFW profiles using the parameters obtained from the dynamical modeling, for both the cored and cusped density models.

However, the generalised Hernquist halo model, represented by the lower panel of Fig. 4.33, exhibits a noticeable deviation from the observed velocity dispersion. The predicted velocity dispersion from the generalised NFW profile is relatively lower compared to the simulation results. This discrepancy suggests that the generalised Hernquist model may not be as effective in reproducing the velocity dispersion profile of the galaxy, potentially due to its assumptions or limitations in capturing the true dynamics of the system.

Despite the generalised NFW model showing some deviations in reproducing the velocity dispersion profile, it still demonstrates a notable capability to recover the mass of the galaxy. This suggests that while the generalised NFW model may not be the most widely accepted model for capturing detailed kinematics, it still provides reasonable estimations of the galaxy's mass. This highlights the importance of considering multiple aspects, such as dynamical properties and mass estimates when evaluating the effectiveness of different models in understanding the galaxy's overall dynamics.

A low v_{los}/σ ratio at the center of the galaxy suggests that the galaxy is pressure-dominated, with high-velocity dispersion compared to the line of sight velocity. This could indicate a more elliptical or spheroidal structure in the central region.

As we move outward and the v_{los}/σ ratio increases, this suggests that the rotational motion becomes more significant, approaching the level of the velocity dispersion. This could indicate a transition to a more disk-like structure in the outer regions. The increase in rotational motion could indeed help to stabilize the galaxy and contribute to a prolate rotation shown in Fig. 4.34. As well as here cored NFW DM profile predicts more accurate v_{los}/σ than other JAM models.

Upon comparing the mass predictions from the cored and cusped DM profiles, it becomes evident that the cored density profile provides a more accurate fit for both the outer and inner parts of the galaxy displayed

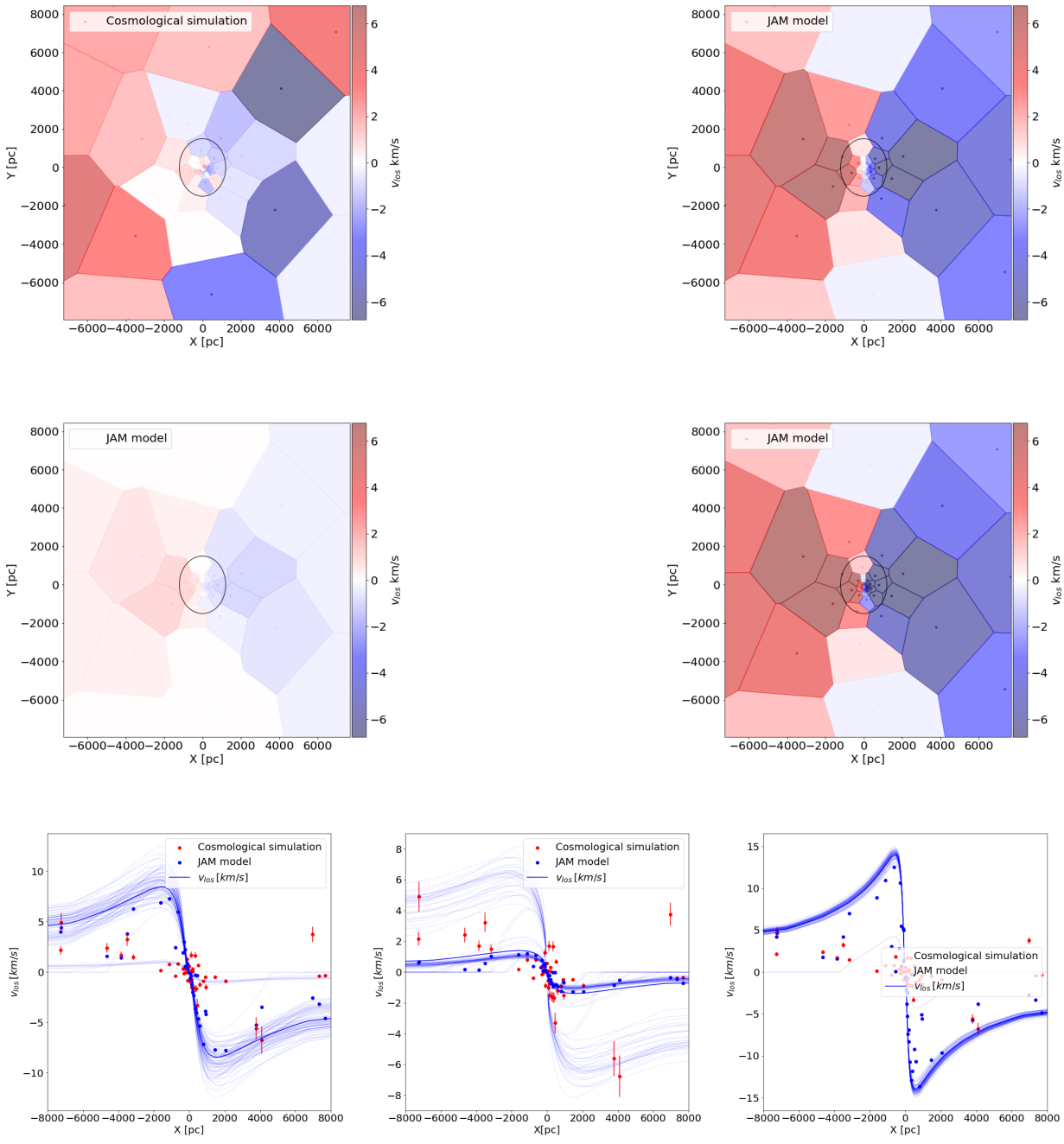

Figure 4.32: Comparison between the 2D line-of-sight velocities of the galaxy derived from the cosmological simulation (top left) and those predicted by the JAM model employing various DM profiles: cored (top right), cusped (middle left), and generalized DM halo (middle right). The black ellipses indicate the galaxy's half-light radius. The lower panel illustrates the 1D line-of-sight velocity profiles across all three models.

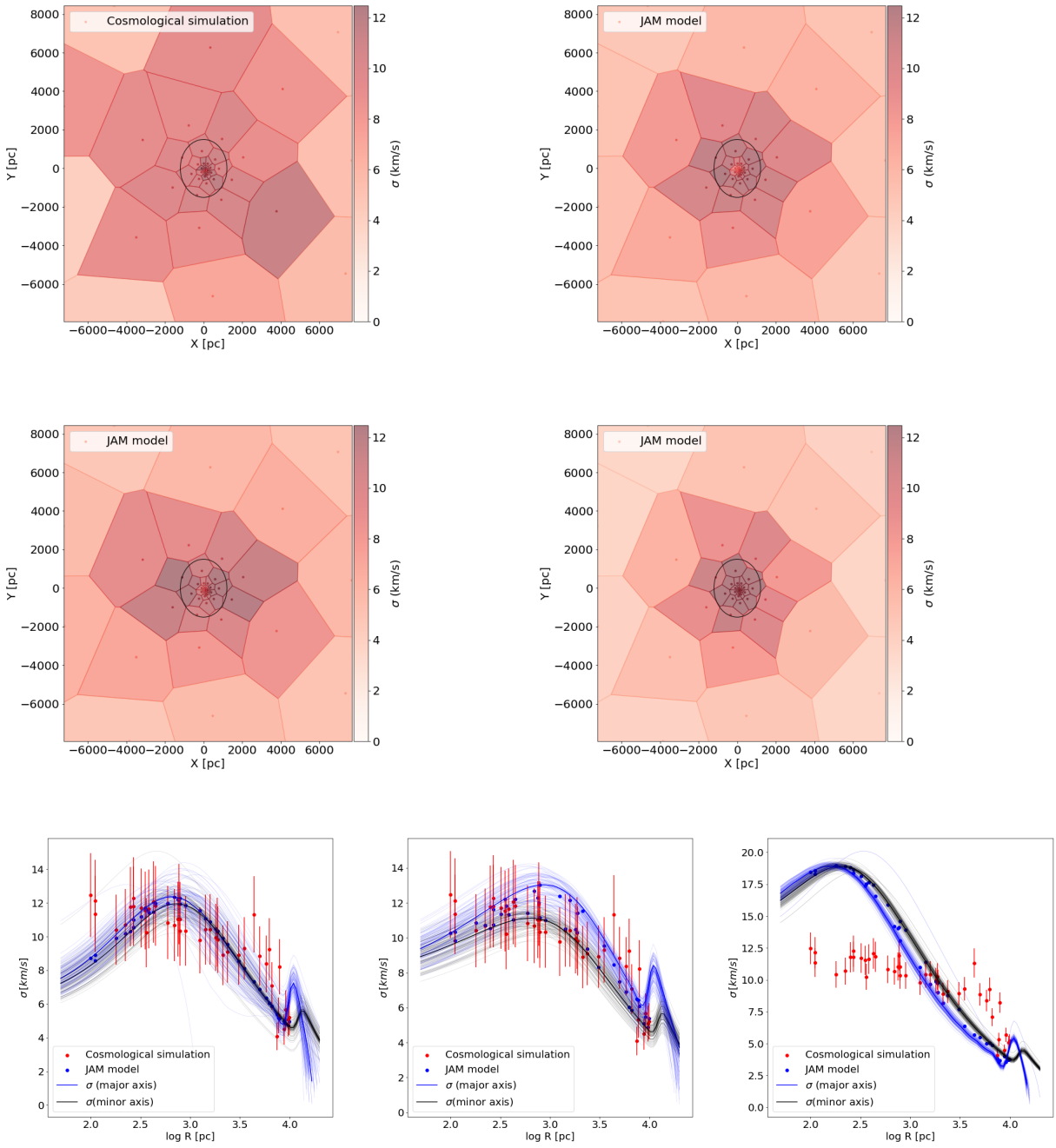

Figure 4.33: The images display 2D velocity dispersion data derived from various models and simulations: the cosmological simulation (top left), line-of-sight velocity dispersion projected by the JAM model using a cored DM profile (top right), a cusped DM profile (middle), and a generalized Hernquist density profile (bottom). The lower panel showcases the 1D velocity dispersion along both major and minor axes.

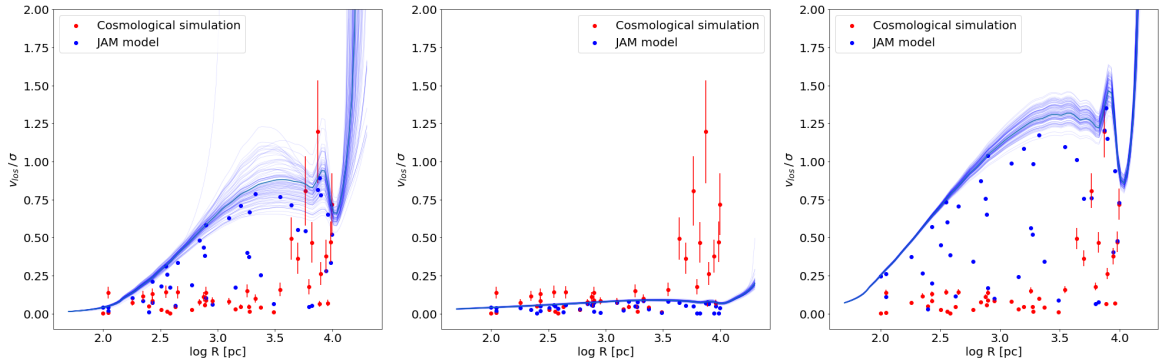

Figure 4.34: v_{los}/σ diagram of the galaxy at $z = 0$ calculated from the JAM models: cored DM (left), cusped DM (middle), and generalised DM (right) . Red and blue dots represent the observed and modeled values, respectively, with the modeled values shown as thick blue lines and their posterior distribution as light blue lines.

in Fig. 4.35. This implies that the cored DM profile is better suited for capturing the underlying mass distribution of the galaxy, as it aligns more closely with the mass profile derived from the cosmological simulation. This suggests that the cusped model may capture the mass distribution more effectively in the outer regions, while the cored model excels in reproducing the mass profile in the inner regions.

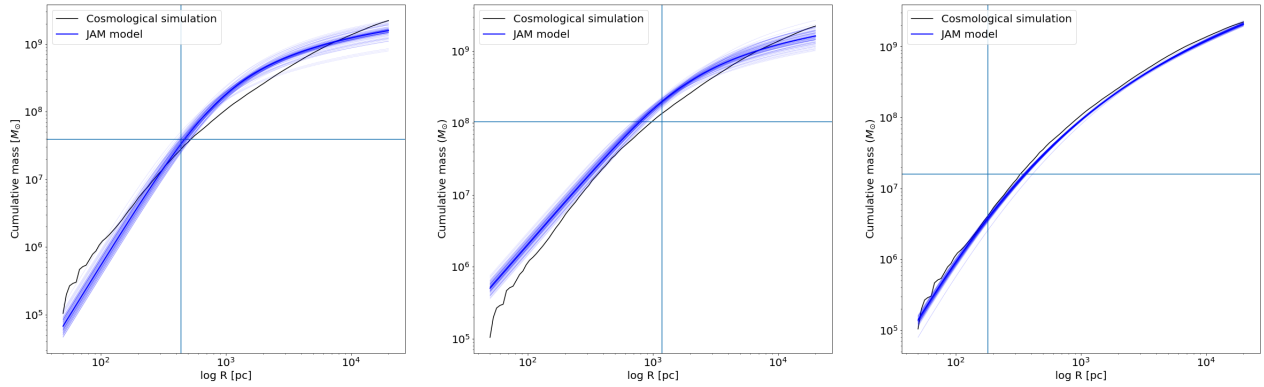

Figure 4.35: Comparison of the calculated dynamical masses from the JAM models with the observational data extracted from the cosmological simulation. The figures illustrate the cored density profile (left), cusped density profile (middle), and a generalized Hernquist halo (right). The blue lines depict the virial mass computed based on the methodology described in Wolf et al. (2010), while the vertical lines indicate the half-light radius of the simulated system.

4.4 *N*-body Simulation

To investigate the evolution of the rotational behavior of the galaxy in the future, we performed an *N*-body simulation. The simulation allows us to track the evolution of the galaxy's dynamics and assess whether it continues to exhibit prolate rotation or undergoes any changes over time.

In the ongoing exploration of the galaxy's dynamics, we closely monitor the stars' orbital angular momentum and velocity distribution within the simulation. This observation aims to discern any shifts in the rotational axis or persistent prolate rotation patterns, contributing significant insights into the galaxy's

long-term stability and evolutionary dynamics.

Moreover, leveraging the fitted Jeans model and the resultant 6D phase space distribution, we undertake *N*-body simulations to follow up the galaxy's phase space distribution's evolution. By simulating the galaxy's dynamics over a defined timeframe (400 Myr after the last snapshot with a time step of 1 Myr), we analyze the potential changes in the phase space distribution and kinematics, providing a comprehensive view of its evolutionary trajectory. Through these simulations, we trace the positions and velocities of individual particles, considering their mutual gravitational interactions and assessing how the galaxy's kinematics evolve, particularly observing the continuity or alteration of the prolate rotation pattern. For this analysis, we utilized the SWIFT code (Schaller et al., 2016), which is a parallel code designed to work in conjunction with the GADGET-2 code (Springel, 2005).

Our *N*-body model has two components - one is the mass distribution of the stars and the other is the DM mass distribution. The first step is to create initial conditions for the *N*-body run.

Creating a mock galaxy for the initial conditions of the *N*-body simulation poses a challenge due to our limited access to only a projected image, which offers solely 2D insights into the galaxy. Deriving the intrinsic 3D density distribution from this 2D image remains a complex task and a crucial step in accurately modeling the galaxy's dynamics.

In our study, we opted not to decompose the galaxy into separate disk and bulge components, instead relying on the Sérsic brightness profile fitted to the surface brightness of the cosmological simulation (equation 3.1; Ciotti and Bertin (1999) and Sérsic (1963)). Utilizing the MGE method outlined in Cappellari (2002), we performed a deprojection process. Initially, we deprojected each Gaussian component individually from the 2D MGE surface brightness to acquire their 3D intrinsic density distributions. Subsequently, we combined the 3D density distributions of all components to represent the entire galaxy.

We used the inverse transform sampling to generate the positions of the star particles according to the de-projected brightness profile.

Inverse Transform Sampling

For a 1D case, let $f(x)$ represent a probability distribution function (PDF) defined on the interval $[a, b]$, with its corresponding cumulative distribution function (CDF) $F_X(x)$ being a strictly increasing function. To generate N samples $(x_1, x_2, \ldots, x_N)$ that follow the distribution described by $f(x)$, the inverse transform sampling method uses the inverse of the CDF:

$$x_j = F_X^{-1}(u_j), \quad \text{where } u_j \text{ is uniform random value in the interval } [0, 1].$$

In practical applications, obtaining the inverse transform F_X^{-1} directly may not be straightforward. Therefore, to find x_j, the equation $F_X(x_j) = u_j$ is solved iteratively to find its roots, as F_X^{-1} might not have a simple analytical expression. Generating N samples using this method involves solving N root-finding problems to obtain the desired random samples following the given PDF $f(x)$ (An et al., 2022).

Stars

The stellar distribution in galaxies is commonly characterized using brightness measurements, often described by generalized exponential profiles like the Sérsic profile given by Equation 3.1. The Sérsic index plays a crucial role in understanding the galaxy's structural properties. In our simulated galaxy, the best-fitted Sérsic index falls within the range ($1 < n < 2$), indicating a low central light concentration similar to the disks of spiral galaxies.

The 3D luminosity density of the galaxy is obtained from the surface brightness ($I(R)$), by de-projection which is done by using the Abel integration (see Tonelli, 1928).

However, in our study, we employ the MGE approach for de-projecting the surface brightness, which offers computational advantages for solving the Jeans equations and obtaining higher velocity moments. The 3D luminosity density profile resulting from the deprojected Sérsic profile in the axisymmetric case is expressed by Equation 4.2, where *N* represents the number of Gaussian functions, L_j represents the surface brightness for each Gaussian, q_j represents the axis ratio.

$$\rho(R,z) = \sum_{j=0}^{N} \frac{L_j}{(\sigma_j\sqrt{2\pi})^3 q_j} \times \exp\left[-\frac{1}{2\sigma_j^2}\left(R^2 + \frac{z^2}{q_j^2}\right)\right] \tag{4.2}$$

Using Equation 4.2, we can compute the cumulative luminosity of each Gaussian component and we employ inverse transform sampling to generate random star positions assuming that the luminosity is a proxy to the stellar density.

Fig. 4.36 compares the 3D number density of the mock galaxy with the volume density derived from the MGE method. The close correspondence between the number density of the test particles and the density profile obtained from the cosmological simulation validates our mock galaxy model.

Through the 1D inverse transform sampling method, we obtained random samples representing the elliptical radial coordinates of our star particles. These samples were then transformed to 3D position coordinates of the test particles by generating the spherical angles θ and ϕ. θ is sampled as the arccos of a uniform random variable between $[-1, +1]$. ϕ is a uniformly sampled in the interval $[0, 2\pi]$. These sample points represent the spherical coordinates. The Cartesian coordinates of the generated points are calculated from the radial distances and the spherical angles, taking into account the galaxy's ellipsoidal shape. The projected 3D position of the galaxy in three coordinates axes are shown in Fig. 4.37

For the construction ICs of the mock galaxy, various methods can be employed, including DF-based, moment-based, orbit-based, and others. Each method offers unique advantages and challenges in creating a stable and realistic galaxy model. In this project we used Jeans equations (moment-based) to get the velocity distribution of the mock galaxy.

The best fit JAM model provides the mean velocity and velocity dispersion for the mock galaxy at the position of each star. Subsequently, we sample the random velocities of each particle by sampling from a normal distribution centered around the mean velocity and the dispersions predicted by the JAM model. The resultant line-of-sight velocity and the velocity dispersion of sampled galaxy and the JAM model is shown in Fig. 4.38.

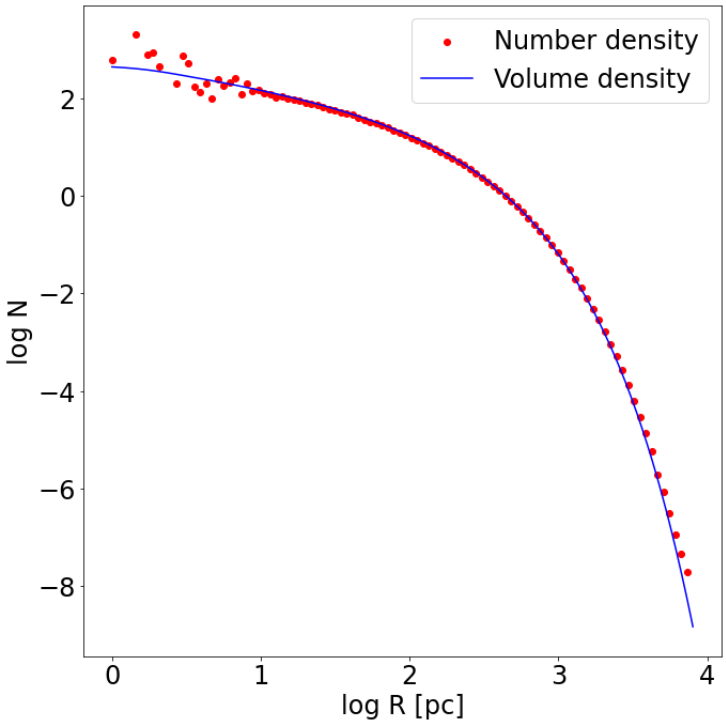

Figure 4.36: Random sample generated from the inverse transform sampling of deprojected density profile.

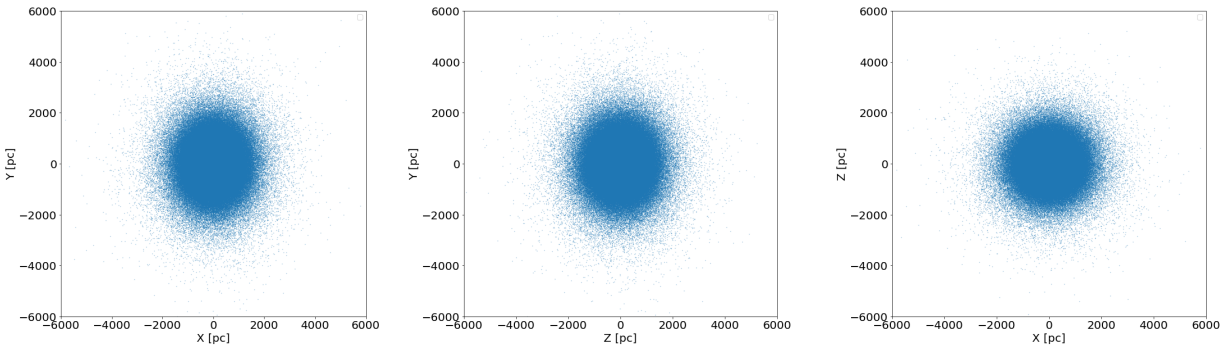

Figure 4.37: Random sample generated from the 3D intrinsic density profile from the deprojection of the 2D brightness profile.

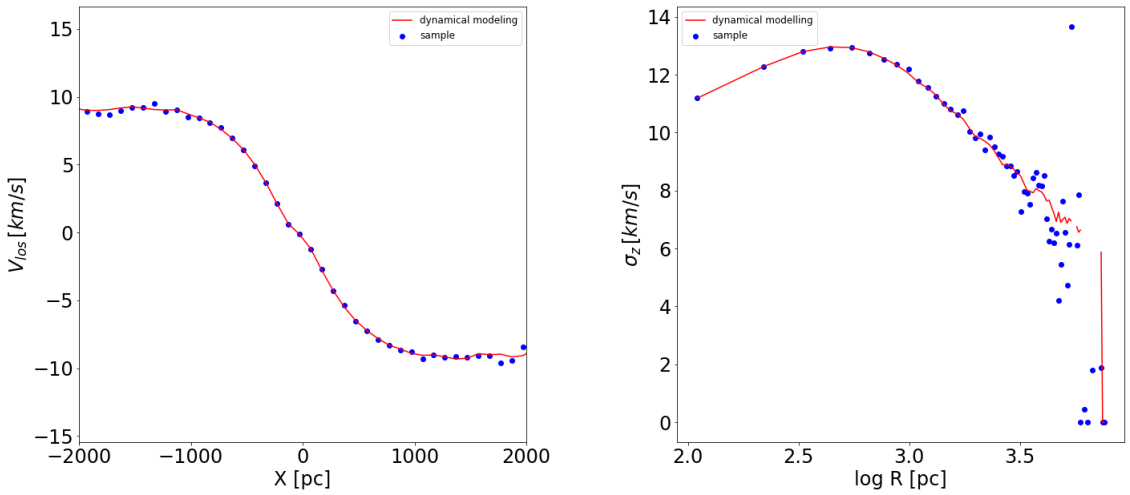

Figure 4.38: Comparision of the sampled galaxy with the JAM model: line of sight velocity (Left), and velocity dispersion along the line of sight (Right). Blue dots represent the binned data points of the random sample, while the solid red line represents the JAM model.

Dark Matter

In our *N*-body simulation, we employ an embedded cored NFW DM profile with parameters according to our best fit JAM model.

The density profile of any halo can be described by the equation (Navarro et al., 1997):

$$\frac{\rho(r)}{\rho_{crit,0}} = \frac{\delta_{char}}{(r/r_s)(1+r/r_s)^2} \tag{4.3}$$

This describes the density profile of any halo with only two parameters, a characteristic density contrast, δ_{char} and the scale radius r_s. In this context, the term "density contrast" refers to the density expressed in terms of the critical density, denoted as $\rho_{\text{crit}} = \frac{3H^2}{8\pi G}$, where $H(z=0) = 70\,\text{km s}^{-1}\,\text{Mpc}^{-1}$ represents the Hubble constant.

By defining the mass of a halo as the mass enclosed within r_{200}, the radius of a sphere with a mean density contrast of 200, we introduce a single adjustable parameter that fully describes the mass profiles of halos with a given mass (Navarro et al., 1997; Power et al., 2003).

The scale radius r_s is defined by r_v/c where r_v is the virial radius and c is the concentration parameter which is related to the characteristic density (Łokas, 2001): $\delta_{char} = 200\,c^3\,g(c)/3$ where,

$$g(c) = \frac{1}{ln(1+c) - \frac{c}{1+c}} \tag{4.4}$$

Assigning the total mass of the DM to match the mass derived from the galaxy's Jeans modeling ensures a consistent framework for the mass distribution within the model. This implies that our star particles reside within a spherical DM structure, with their combined mass matching the value obtained from the JAM model. Here, we set the mass of each star particle as calculated from the galaxy's luminosity, which is

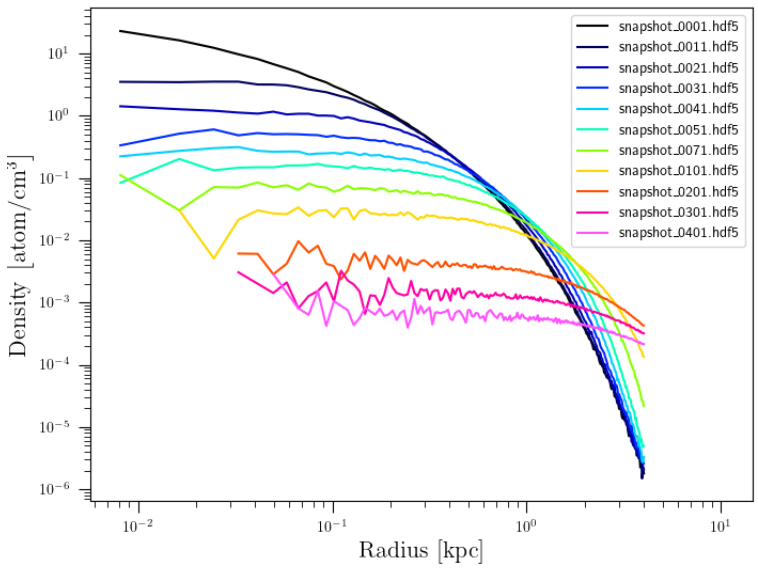

Figure 4.39: Density variation of the galaxy during ongoing evolution over the next 300 Myr.

approximately $11 M_\odot$ for 1000000 test particles.

The softening parameter is crucial in *N*-body simulations as it mitigates the impact of gravity between closely positioned gravitational bodies. To determine this parameter, we consider the maximum stochastic acceleration caused by close approaches to a single particle, $a_{\text{max}} = Gm/\epsilon^2$, which should be less than the minimum mean-field acceleration in a virial halo, $a_{\text{min}} = GM_{200}/r_{200}^2$. This argument sets a lower limit for the softening length necessary to avoid strong discreteness effects, $\epsilon > \epsilon_{\text{acc}} \sim r_{200}/\sqrt{N_{200}}$, where N_{200} is the number of particles within the virial radius. This criterion ensures that discreteness effects are effectively managed within the simulation (Dehnen & Read, 2011; Power et al., 2003; T. Zhang et al., 2019).

We employed the SWIFT hydrodynamical simulation code, which is a parallel code built upon the foundation of GADGET-2. This newly developed open-source cosmological code is specifically designed to solve the equations of hydrodynamics using a particle-based approach (Schaller et al., 2023; Schaller et al., 2016).

In our straightforward *N*-body simulation, we employed 1000000 particles to represent the galaxy. We chose a softening length of 0.001 kpc and set the virial mass of the galaxy to $1 \times 10^9 M_\odot$ in accordance to our JAM model. This configuration yielded a concentration parameter for the DM halo of $c = 25$, with a scale radius of 0.8 kpc. The *N*-body simulation was conducted over a duration of 400 Myr with a step of 1 Myr.

Fig. 4.39, illustrate the spherically averaged density profiles along galaxy's radius, when evolved with time. The distinct drop in density suggest that after 200 Myr, the galaxy is primarily influenced by the DM density, potentially leading to a loss of its prolate nature.

Indeed, the extended nature of the DM profile, which dominates the galactic potential, has a profound effect on the behavior of the star particles within the galaxy. As the DM distribution extends far beyond the stellar component, the central compactness of the galaxy diminishes. Consequently, the influence of random motion within the galaxy increases, leading to a reduction in the rotational velocity of the galaxy. This can be clearly illustrated in the 2D projection plot of the galaxy with the color-coded line-of-sight velocity in Fig. 4.40.

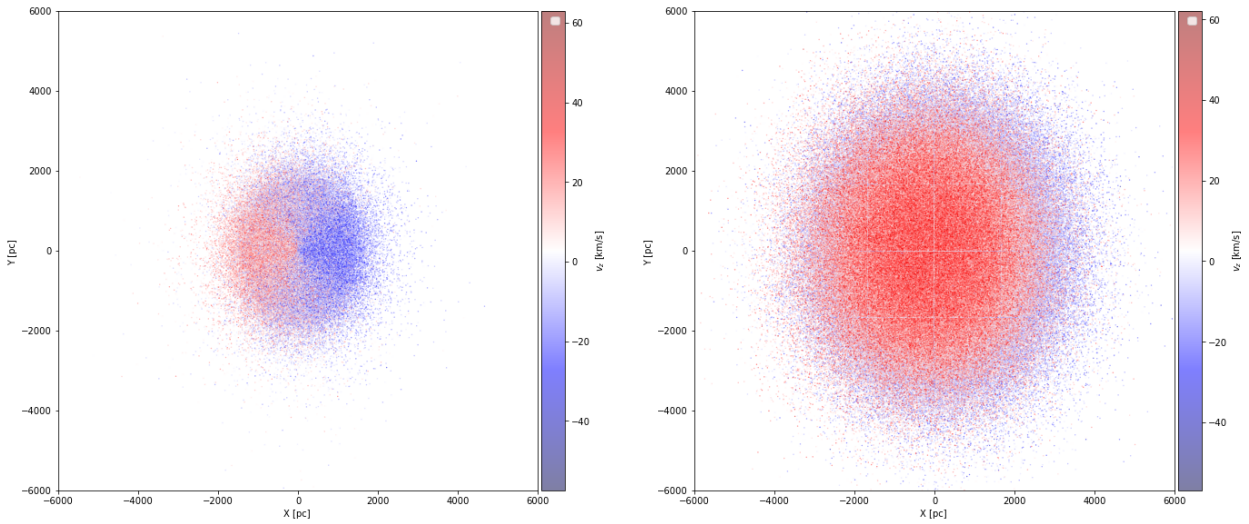

Figure 4.40: 2D plot illustrating the projected line-of-sight stellar velocity field. The left panel displays the galaxy's initial phase, while the right panel depicts its state after 100 Myr.

The projected 2D positions of the stars in the *N*-body galaxy provide valuable insights into the distribution of ordered motion. We observe a rapid loss of ordered motion, and the velocity distribution becomes randomized due to the pressure forces. This randomization contributes to the overall stability of the system, allowing the galaxy to maintain its dynamic equilibrium.

Fig. 4.41 shows the radial profiles of the velocity dispersion along the line-of-sight (upper) and the mass profiles (lower) produced by SWIFT both at the initial time and after different times of evolution. Upon the time evolution, the velocity dispersion profiles decrease at the center, while increasing at the outer radius. This trend may be influenced by presence of the DM halo, with its gravitational effects causing the outer edges of the galaxy to move faster, as expected. Which can also be observed from the lower panel of Fig. 4.41, where the spherically averaged mass of the galaxy is dominated at the outer radius after 200 Myr, sufficiently suppressing the inner velocity dispersion and the rotational velocity of the galaxy.

The initialization of the initial conditions could significantly impact the equilibrium state of the galaxy. For instance, in the prolate rotation scenario of the galaxy, our assumption of a spherical DM potential might influence the transition of stars from a prolate to a spherical nature, as indicated in the right panel of Fig. 4.40. This suggests that a prolate DM halo might be possible explanation of the prominent prolate nature of the galaxy's shape.

On the other hand, in this simplified scenario, the rotation of the galaxy diminishes after approximately 100-200 Myr. This implies that the initialization approach may not be accurate, as it does not account for gas dynamics, molecular clouds, and potentially a central DM component. The exclusion of these components directly impact the rotational dynamics of the galaxy.

We aim to explore alternative methods for generating more accurate ICs for *N*-body simulations in future projects. One approach involves sampling the DM halos to better capture the shape of the galaxy. Additionally, we plan to create ICs using GalIC, a method that offers more sophisticated techniques for constructing galaxy models. These endeavors will contribute to refining our understanding of galaxy dynamics and evolution in *N*-body simulations, especially in a prolate rotating system.

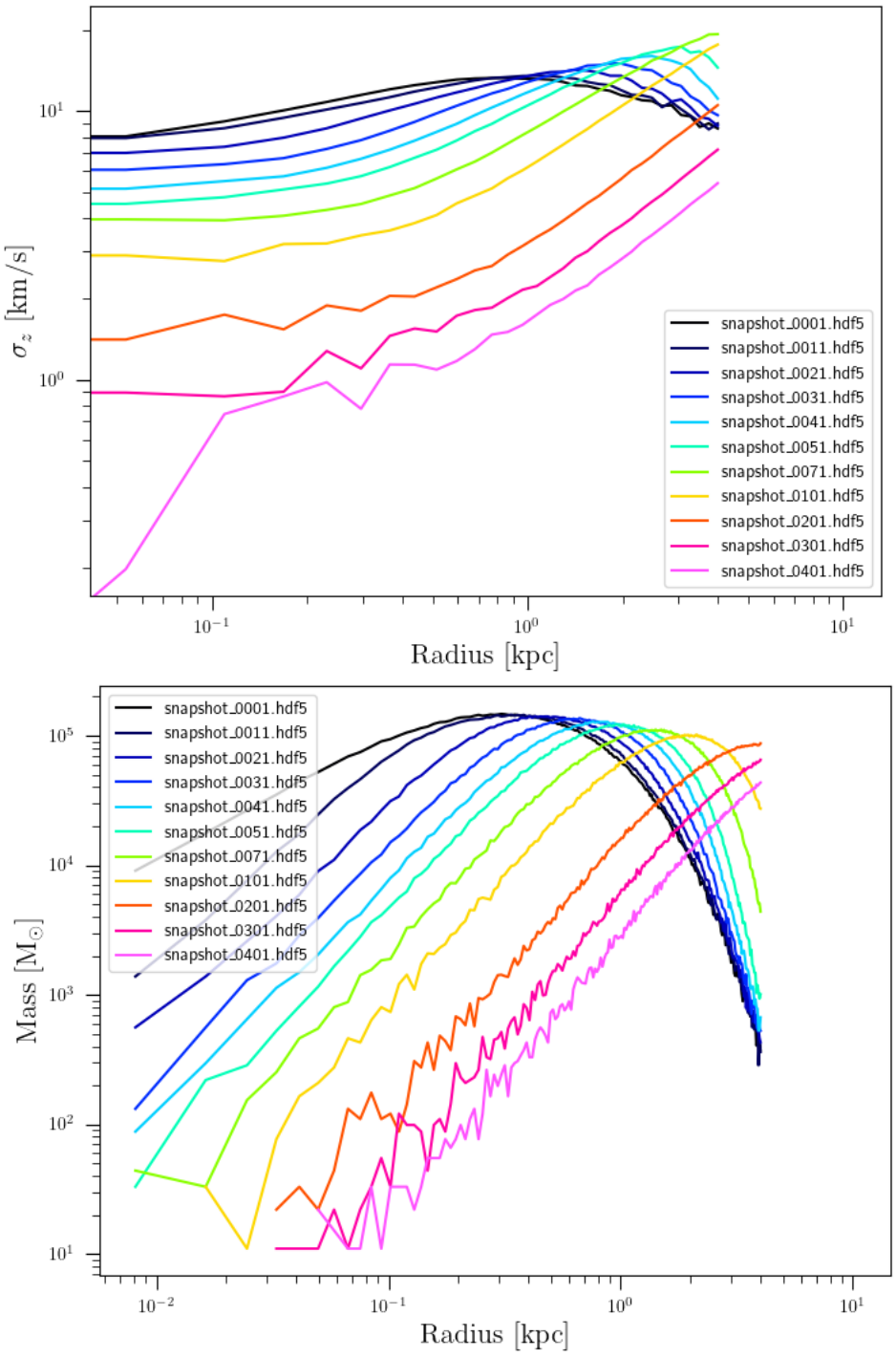

Figure 4.41: Variation of the velocity dispersion along line-of-sight velocity (Upper panel), and the cumulative mass of the galaxy (Lower panel) over next 400 Myr.

Chapter 5

CONCLUSION

This work presents the study of an equilibrium modeling of a cosmologically simulated galaxy at the different times of its evolution. The interesting thing about this particular galaxy is that it transforms into a prolate rotator after a major merger event. We summarize the obtained results in this section, along with highlighting the caveats of the study and suggesting avenues for future research.

First of all, we used the data generated by a hydrodynamical cosmological simulation of the dwarf galaxy which shows the rotation around the major axis (Cardona-Barrero et al., 2021). The main goal of this work is to perform the equilibrium Jeans Axisymmetric Modeling (JAM), for all the different evolutionary stages of the galaxy assuming it is at quasi-equilibrium state. JAM was extensively used to understand the dynamics of equilibrium systems, mostly for oblate rotators ($q < 1$). But this work is entirely new as this is the first attempt to do the JAM modeling for a prolate rotating system ($q > 1$) and the results are encouraging.

As a first step, we utilized the Voronoi binned data of the galaxy's luminosity to calculate its luminosity density profile. This profile was then fitted to a Multi-Gaussian Expansion MGE model, which facilitated the analytical solution of the Jeans equations. Additionally, we incorporated the kinematics, specifically the velocity moments of the galaxy, as the second input for the JAM model. The gravitational potential of the galaxy was a crucial component, modeled using an NFW spherical halo, as the majority of the galaxy's mass is composed of DM. We examined cored, cusped, and generalised DM density profiles to determine which best aligned with the simulated data. During the kinematic analysis, we fitted the velocity anisotropy parameter (β_z) and the rotation parameter (κ) of the galaxy. These parameters provide insights into the distribution of velocity ellipsoids and the deviation of the velocity field with respect to an isotropic rotator.

We initiated our modeling process from the early stage of the galaxy's evolution, specifically at $z = 1.58$, when the simulated galaxy exhibited clear oblate rotation. This initial phase served as a benchmark for further analysis, as the JAM model has been successfully applied to galaxies with similar rotation characteristics in previous studies. The result of the JAM model suggests that it can regenerate the kinematics of the galaxy as assumed by the simulation. But we saw that the cored NFW DM profile is more favored than the cusped NFW DM in recovering the kinematics and the mass of the galaxy. During the initial phase of the galaxy's evolution, we observed a positive velocity anisotropy ($0 < \beta_z < 1$), indicating that the velocity ellipsoids are not perfectly spherical but slightly oblate in nature. Similarly, the rotation parameter ($\kappa \neq 1$), implying that the velocity ellipsoid is not spherical everywhere and exhibits specific rotation. This suggests that rotational support plays a significant role in the galaxy's dynamics during this phase.

Moreover, we extended our study to evaluate whether the JAM model could explain the dynamics of the galaxy at various time intervals. We tested the JAM model at different stages of the galaxy's evolution, but here we focused on two significant steps: shortly after the major merger ($z = 0.58$), when the galaxy begins rotating around its major axis, and at the present time ($z = 0$), which is a crucial stage as the galaxy continues to exhibit rotation around its major axis.

The results indicate that the JAM model also successfully recovered the prolate kinematics of the galaxy at $z = 0.58$ and its mass with the cored NFW DM profile, which provided more accurate dynamics than the cusped profile.

Furthermore, when fitting the velocity anisotropy and rotation parameter, we obtained $\beta_z < 0$, indicating a prolate velocity ellipsoid, and $\kappa \neq 1$, suggesting the galaxy is not an isotropic rotator. In this case, we found that only prolate velocity ellipsoids can solve the Jeans equations, strongly favoring the orientation of the velocity ellipsoid to be prolate. In contrast, we remind the reader that both prolate and oblate velocity ellipsoids are viable solutions to the Jeans equations for oblate rotating systems.

Additionally, we introduced the generalized NFW DM profile, which better matched the mass obtained from the hydrodynamical cosmological simulation. However, this model couldn't accurately reproduce the actual velocity moments predicted in the simulation.

In the third JAM model, we explored the present stage of the evolution ($z = 0$). Here also, we compared the dynamics obtained from the model with the simulated data. We obtained results similar to those when the galaxy was at $z = 0.58$. One important finding was that the mass profile predicted by the JAM model almost matched even better with the simulation. In this case also, the dynamical parameters $\beta_z < 0$ and $\kappa \neq 1$, indicating a prolate velocity ellipsoid.

We also evaluated the dynamical stability of the JAM model through *N*-body simulations, as the last stage of the cosmological simulation appears to be time enduring. To accomplish this, we employed the de-projected luminosity density to generate 3D positions of a corresponding mock galaxy. Then we utilized the Jeans equations to obtain the 3D velocity field for our *N*-body system. For the *N*-body simulation, we used the SWIFT code, which is a derivation of the GADGET-2 code.

We assigned a stellar mass of each *N*-body particle, obtained from the luminosity profile of the galaxy, which is embedded within the spherical NFW DM halo. We ran our *N*-body model for the next 400 Myr, but the results were not entirely surprising. The prolonged prolate rotation observed in the cosmological simulation suddenly disappeared after 100-200 Myr in contrast to its longevity in the cosmological simulation. This discrepancy could stem from various factors. One possibility is that the initial conditions (IC) of the *N*-body model were not as accurate as those in the cosmological simulation. Another factor could be the influence of the DM halo, which might increase the random motion within the galaxy, thereby suppressing the ordered motion.

Overall, it remains an open question what are the main factors responsible for the time endurance of the prolate rotation in the cosmological simulation.

Caveats and Future work

It is worth noting that the dynamics of galaxies are influenced by a multitude of factors, including the interplay between dark matter, baryonic matter, and the hierarchical merging processes that shape galaxy formation and evolution. Therefore, further investigations and refinements in the simulation setup, such as incorporating more detailed baryonic physics or exploring alternative merger scenarios, may also contribute to a better understanding of the behavior and persistence of prolate rotation in galaxies.

The rotational velocity of the galaxy at the cosmological simulation is low, with the average slope of the rotational velocity being $dv_{rot}/dr = 0.88 \pm 0.12\,\mathrm{km\ s^{-1}\ kpc^{-1}}$ at $z = 0$ (Cardona-Barrero et al., 2021). It is noteworthy that despite the caveat of a low $V_{rot}^{max}/\sigma_{3D}$ ratio observed in the galaxy, the overall test was successful.

However, it is important to acknowledge that there are certain discrepancies in the early stage of the galaxy with the best fit model. It can be attributed to several factors. Firstly, the lack of detailed information at the outer scale of the galaxy can limit the accuracy of model predictions. Outer regions of galaxies often have sparse data, making it challenging to constrain the dynamical models effectively.

Additionally, the accuracy of the kinematic estimates heavily relies on the surface brightness profile, which is used as a crucial tracer. Errors or uncertainties in the surface brightness measurements can propagate into the estimation of kinematics and potentially introduce discrepancies in the results.

During the fitting process of the JAM model with the available data, we encountered some intricacies. We found that there is a narrow β_z and κ space of the valid model. This can make it harder to find a model that fits the data well while also satisfying the physical constraints of the system.

In the future, we plan to conduct observational studies to measure the proper motion and positions of the majority of stars in the Phoenix dwarf galaxy. This galaxy exhibits characteristics similar to those of our simulated galaxy. Through this observational endeavor, we aim to evaluate the reliability and accuracy of our model in capturing the dynamics and kinematics of real-world celestial objects. Such observations will provide valuable insights into the behavior of galaxies and help refine our understanding of their evolutionary processes.

We also intend to perform more dynamic modeling, such as the orbit-based Schwarzschild model, which is comparable to our fitted JAM model and takes into account the galaxy's triaxial structure. This comparison analysis is helpful in determining if the two equilibrium models can realistically fit the simulated data.

Additionally, our *N*-body simulation reveals that the prolate rotation diminishes prematurely. We can consider alternative approaches to investigate potential errors during the *N*-body simulation. One option is to introduce an external prolate dark matter halo, while another involves sampling the halo from the mass predicted by the Jeans model. These strategies will help us identify and address the factors contributing to the observed discrepancy.

Indeed, the JAM models have provided valuable insights into the velocity anisotropy, rotation, mass profile, and kinematics of the galaxy. They have successfully reproduced the observed data and yielded meaningful results.

The utilization of data from the cosmological simulation in this study has provided valuable insights and

benefits. By testing the viability of the dynamical models on simulated data, this study offers a robust assessment of the models' performance and their ability to reproduce the observed kinematics and mass profile of a prolate rotating galaxy.

The test results analysed using the cosmological simulation provide a valuable benchmark for evaluating the accuracy and effectiveness of the dynamical models. This study validates the use of simulated data, increasing confidence in the analysis and interpretation of observational data from galaxies.

References

Abraham, R. G., Valdes, F., Yee, H., & van den Bergh, S. (1994). The morphologies of distant galaxies. 1: An automated classification system. *Astrophysical Journal, Part 1 (ISSN 0004-637X), vol. 432, no. 1, p. 75-90*, *432*, 75–90.

Abraham, R. G., Van Den Bergh, S., & Nair, P. (2003). A new approach to galaxy morphology. i. analysis of the sloan digital sky survey early data release. *The Astrophysical Journal*, *588*(1), 218.

Ade, P. A., Aghanim, N., Arnaud, M., Ashdown, M., Aumont, J., Baccigalupi, C., Banday, A., Barreiro, R., Bartlett, J., Bartolo, N., et al. (2016). Planck 2015 results-xiii. cosmological parameters. *Astronomy & Astrophysics*, *594*, A13.

Amorisco, N. C., Evans, N. W., & van de Ven, G. (2014). The remnant of a merger between two dwarf galaxies in andromeda ii. *Nature*, *507*(7492), 335–337.

An, X., Artemyev, A., Angelopoulos, V., Lu, S., Pritchett, P., & Decyk, V. (2022). Fast inverse transform sampling of non-gaussian distribution functions in space plasmas. *Journal of Geophysical Research: Space Physics*, *127*(5), e2021JA030031.

Bertin, G. (2014). *Dynamics of galaxies*. Cambridge University Press.

Binney, J., & Mamon, G. A. (1982). M/l and velocity anisotropy from observations of spherical galaxies, or must m87 have a massive black hole? *Monthly Notices of the Royal Astronomical Society*, *200*(2), 361–375.

Binney, J., & Merrifield, M. (1998). *Galactic astronomy*. Princeton University Press.

Binney, J., & Tremaine, S. (2011). *Galactic dynamics* (Vol. 20). Princeton university press.

Bovy, J., & Rix, H.-W. (2013). A direct dynamical measurement of the milky way's disk surface density profile, disk scale length, and dark matter profile at 4 kpc $\leq$ r $\leq$ 9 kpc. *The Astrophysical Journal*, *779*(2), 115.

Bovy, J., & Tremaine, S. (2012). On the local dark matter density. *The Astrophysical Journal*, *756*(1), 89.

Brown, A. G., Vallenari, A., Prusti, T., De Bruijne, J., Babusiaux, C., Biermann, M., Creevey, O., Evans, D., Eyer, L., Hutton, A., et al. (2021). Gaia early data release 3-summary of the contents and survey properties. *Astronomy & Astrophysics*, *649*, A1.

Bullock, J. S., & Boylan-Kolchin, M. (2017). Small-scale challenges to the Λ cdm paradigm. *Annual Review of Astronomy and Astrophysics*, *55*, 343–387.

Cappellari, M. (2002). Efficient multi-gaussian expansion of galaxies. *Monthly Notices of the Royal Astronomical Society*, *333*(2), 400–410.

Cappellari, M. (2008). Measuring the inclination and mass-to-light ratio of axisymmetric galaxies via anisotropic jeans models of stellar kinematics. *Monthly Notices of the Royal Astronomical Society*, *390*(1), 71–86.

Cappellari, M. (2016). Structure and kinematics of early-type galaxies from integral field spectroscopy. *Annual review of astronomy and astrophysics*, *54*, 597–665.

Cappellari, M. (2020). Efficient solution of the anisotropic spherically aligned axisymmetric jeans equations of stellar hydrodynamics for galactic dynamics. *Monthly Notices of the Royal Astronomical Society*, *494*(4), 4819–4837.

Cappellari, M., & Copin, Y. (2003). Adaptive spatial binning of integral-field spectroscopic data using voronoi tessellations. *Monthly Notices of the Royal Astronomical Society*, *342*(2), 345–354.

Cappellari, M., Emsellem, E., Bacon, R., Bureau, M., Davies, R. L., De Zeeuw, P., Falcón-Barroso, J., Krajnović, D., Kuntschner, H., McDermid, R. M., et al. (2007). The sauron project–x. the orbital anisotropy of elliptical and lenticular galaxies: Revisiting the (v/σ, ϵ) diagram with integral-field stellar kinematics. *Monthly Notices of the Royal Astronomical Society*, *379*(2), 418–444.

Cardona-Barrero, S., Battaglia, G., Di Cintio, A., Revaz, Y., & Jablonka, P. (2021). Origin of stellar prolate rotation in a cosmologically simulated faint dwarf galaxy. *Monthly Notices of the Royal Astronomical Society: Letters*, *505*(1), L100–L105.

Chaisson, E. J., et al. (2014). The natural science underlying big history. *The Scientific World Journal*, *2014*.

Cimatti, A., Fraternali, F., & Nipoti, C. (2019). *Introduction to galaxy formation and evolution: From primordial gas to present-day galaxies*. Cambridge University Press.

Ciotti, L., & Bertin, G. (1999). Analytical properties of the r^(1/m) luminosity law. *arXiv preprint astro-ph/9911078*.

Courteau, S., Cappellari, M., de Jong, R. S., Dutton, A. A., Emsellem, E., Hoekstra, H., Koopmans, L., Mamon, G. A., Maraston, C., Treu, T., et al. (2014). Galaxy masses. *Reviews of Modern Physics*, *86*(1), 47.

Crnojević, D., & Mutlu-Pakdil, B. (2021). Dwarf galaxies yesterday, now and tomorrow. *Nature Astronomy*, *5*(12), 1191–1194.

Dalcanton, J. J., & Stilp, A. M. (2010). Pressure support in galaxy disks: Impact on rotation curves and dark matter density profiles. *The Astrophysical Journal*, *721*(1), 547.

Deason, A., Wetzel, A., & Garrison-Kimmel, S. (2014). Satellite dwarf galaxies in a hierarchical universe: The prevalence of dwarf–dwarf major mergers. *The Astrophysical Journal*, *794*(2), 115.

Dehnen, W., & Read, J. I. (2011). N-body simulations of gravitational dynamics. *The European Physical Journal Plus*, *126*, 1–28.

de Vaucouleurs, G. (1948). Research on extragalactic nebulae. *Annals of Astrophysics, Vol. 11, p. 247*, *11*, 247.

Ebrová, I., & Łokas, E. L. (2015). The origin of prolate rotation in dwarf spheroidal galaxies formed by mergers of disky dwarfs. *The Astrophysical Journal*, *813*(1), 10.

Ebrová, I., & Łokas, E. L. (2017). Galaxies with prolate rotation in illustris. *The Astrophysical Journal*, *850*(2), 144.

El-Badry, K., Wetzel, A. R., Geha, M., Quataert, E., Hopkins, P. F., Kereš, D., Chan, T., & Faucher-Giguère, C.-A. (2017). When the jeans do not fit: How stellar feedback drives stellar kinematics and complicates dynamical modeling in low-mass galaxies. *The Astrophysical Journal*, *835*(2), 193.

Emsellem, E., Monnet, G., & Bacon, R. (1994). The multi-gaussian expansion method: A tool for building realistic photometric and kinematical models of stellar systems i. the formalism. *Astronomy and Astrophysics, Vol. 285, p. 723-738 (1994)*, *285*, 723–738.

Fattahi, A., Navarro, J. F., & Frenk, C. S. (2020). The missing dwarf galaxies of the local group. *Monthly Notices of the Royal Astronomical Society*, *493*(2), 2596–2605.

Fouquet, S., Łokas, E. L., del Pino, A., & Ebrová, I. (2017). Formation of andromeda ii via a gas-rich major merger and an interaction with m31. *Monthly Notices of the Royal Astronomical Society*, *464*(3), 2717–2729.

Freeman, K. C. (1970). On the disks of spiral and s0 galaxies. *Astrophysical Journal, vol. 160, p. 811*, *160*, 811.

Gaia, C., Brown, A., Vallenari, A., Prusti, T., De Bruijne, J., Babusiaux, C., Juhász, Á., Marschalkó, G., Marton, G., Molnár, L., et al. (2018). Gaia data release 2 summary of the contents and survey properties. *Astronomy & Astrophysics*, *616*(1).

Goodman, J., & Weare, J. (2010). Insem le mplers with 0ne inv ri ne. *Comm. App. Math. Comp. Sci*, *5*, 65–80.

Gregory, A. L., Collins, M. L., Read, J. I., Irwin, M. J., Ibata, R. A., Martin, N. F., McConnachie, A. W., & Weisz, D. R. (2019). Kinematics of the tucana dwarf galaxy: An unusually dense dwarf in the local group. *Monthly Notices of the Royal Astronomical Society*, *485*(2), 2010–2025.

Hammer, F., Puech, M., Chemin, L., Flores, H., & Lehnert, M. (2007). The milky way, an exceptionally quiet galaxy: Implications for the formation of spiral galaxies. *The Astrophysical Journal*, *662*(1), 322.

Harris, W. E., Harris, G. L., & Alessi, M. (2013). A catalog of globular cluster systems: What determines the size of a galaxy's globular cluster population? *The Astrophysical Journal*, *772*(2), 82.

Hayashi, K., Chiba, M., & Ishiyama, T. (2020). Diversity of dark matter density profiles in the galactic dwarf spheroidal satellites. *The Astrophysical Journal*, *904*(1), 45.

Hernquist, L. (1990). An analytical model for spherical galaxies and bulges. *Astrophysical Journal, Part 1 (ISSN 0004-637X), vol. 356, June 20, 1990, p. 359-364.*, *356*, 359–364.

Hofmeister, A. M., & Criss, R. E. (2020). Debated models for galactic rotation curves: A review and mathematical assessment. *Galaxies*, *8*(2), 47.

Jeans, J. H. (1922). The motions of stars in a kapteyn universe. *Monthly Notices of the Royal Astronomical Society, Vol. 82, p. 122-132*, *82*, 122–132.

Kacharov, N., Alfaro-Cuello, M., Neumayer, N., Lützgendorf, N., Watkins, L. L., Mastrobuono-Battisti, A., Kamann, S., van de Ven, G., Seth, A. C., Voggel, K. T., et al. (2022). A deep view into the nucleus of the sagittarius dwarf spheroidal galaxy with muse. iii. discrete multicomponent population-dynamical models based on the jeans equations. *The Astrophysical Journal*, *939*(2), 118.

Kacharov, N., Battaglia, G., Rejkuba, M., Cole, A. A., Carrera, R., Fraternali, F., Wilkinson, M. I., Gallart, C. G., Irwin, M., & Tolstoy, E. (2017). Prolate rotation and metallicity gradient in the transforming dwarf galaxy phoenix. *Monthly Notices of the Royal Astronomical Society*, *466*(2), 2006–2023.

Kado-Fong, E., Greene, J. E., Greco, J. P., Beaton, R., Goulding, A. D., Johnson, S. D., & Komiyama, Y. (2020). Star formation in isolated dwarf galaxies hosting tidal debris: Extending the dwarf–dwarf merger sequence. *The Astronomical Journal*, *159*(3), 103.

Katz, N., Weinberg, D. H., & Hernquist, L. (1995). Cosmological simulations with treesph. *arXiv preprint astro-ph/9509107*.

Kharchenko, N., Piskunov, A., Schilbach, E., Röser, S., & Scholz, R.-D. (2013). Global survey of star clusters in the milky way-ii. the catalogue of basic parameters. *Astronomy & Astrophysics*, *558*, A53.

Klimentowski, J., Łokas, E. L., Knebe, A., Gottlöber, S., Martinez-Vaquero, L. A., Yepes, G., & Hoffman, Y. (2010). The grouping, merging and survival of subhaloes in the simulated local group. *Monthly Notices of the Royal Astronomical Society*, *402*(3), 1899–1910.

Koch, A., Hanke, M., & Kacharov, N. (2018). Kinematics of outer halo globular clusters: M 75 and ngc 6426. *Astronomy & Astrophysics*, *616*, A74.

Krajnović, D., Emsellem, E., Cappellari, M., Alatalo, K., Blitz, L., Bois, M., Bournaud, F., Bureau, M., Davies, R. L., Davis, T. A., et al. (2011). The atlas3d project $--II$. morphologies, kinemetric

features and alignment between photometric and kinematic axes of early-type galaxies. *Monthly Notices of the Royal Astronomical Society*, *414*(4), 2923–2949.

Krajnović, D., Emsellem, E., den Brok, M., Marino, R. A., Schmidt, K. B., Steinmetz, M., & Weilbacher, P. M. (2018). Climbing to the top of the galactic mass ladder: Evidence for frequent prolate-like rotation among the most massive galaxies. *Monthly Notices of the Royal Astronomical Society*, *477*(4), 5327–5337.

Lelli, F. (2022). Gas dynamics in dwarf galaxies as testbeds for dark matter and galaxy evolution. *Nature Astronomy*, *6*(1), 35–47.

Leung, G. Y., Leaman, R., van de Ven, G., Lyubenova, M., Zhu, L., Bolatto, A. D., Falcón-Barroso, J., Blitz, L., Dannerbauer, H., Fisher, D. B., et al. (2018). The edge–califa survey: Validating stellar dynamical mass models with co kinematics. *Monthly Notices of the Royal Astronomical Society*, *477*(1), 254–292.

Li, H., Mao, S., Emsellem, E., Xu, D., Springel, V., & Krajnović, D. (2018). The origin and properties of massive prolate galaxies in the illustris simulation. *Monthly Notices of the Royal Astronomical Society*, *473*(2), 1489–1511.

Łokas, E. L. (2001). Velocity dispersions of dwarf spheroidal galaxies: Dark matter versus mond. *Monthly Notices of the Royal Astronomical Society*, *327*(2), L21–L26.

Łokas, E. L., Ebrová, I., Pino, A. d., & Semczuk, M. (2014). Andromeda ii as a merger remnant. *Monthly Notices of the Royal Astronomical Society: Letters*, *445*(1), L6–L10.

Magorrian, J. (1999). Kinematical signatures of hidden stellar discs. *Monthly Notices of the Royal Astronomical Society*, *302*(3), 530–536.

Martin, G., Jackson, R., Kaviraj, S., Choi, H., Devriendt, J., Dubois, Y., Kimm, T., Kraljic, K., Peirani, S., Pichon, C., et al. (2021). The role of mergers and interactions in driving the evolution of dwarf galaxies over cosmic time. *Monthly Notices of the Royal Astronomical Society*, *500*(4), 4937–4957.

Mateo, M. (1998). Dwarf galaxies of the local group. *Annual Review of Astronomy and Astrophysics*, *36*(1), 435–506.

McKee, C. F., Parravano, A., & Hollenbach, D. J. (2015). Stars, gas, and dark matter in the solar neighborhood. *The Astrophysical Journal*, *814*(1), 13.

McMillan, P. J. (2016). The mass distribution and gravitational potential of the milky way. *Monthly Notices of the Royal Astronomical Society*, stw2759.

Milgrom, M. (2001). Mond a pedagogical review. *arXiv preprint astro-ph/0112069*.

Milgrom, M. (2014). Mond laws of galactic dynamics. *Monthly Notices of the Royal Astronomical Society*, *437*(3), 2531–2541.

Mo, H., Van den Bosch, F., & White, S. (2010). *Galaxy formation and evolution*. Cambridge University Press.

Navarro, J. F., Frenk, C. S., & White, S. D. (1997). A universal density profile from hierarchical clustering. *The Astrophysical Journal*, *490*(2), 493.

Nevin, R., Blecha, L., Comerford, J., Greene, J., Law, D., Stark, D., Westfall, K., Vazquez-Mata, J., Smethurst, R., Argudo-Fernández, M., et al. (2021). Accurate identification of galaxy mergers with stellar kinematics. *The Astrophysical Journal*, *912*(1), 45.

Nipoti, C., Londrillo, P., & Ciotti, L. (2003). Galaxy merging, the fundamental plane of elliptical galaxies and the m bh—σ0 relation. *Monthly Notices of the Royal Astronomical Society*, *342*(2), 501–512.

Oñorbe, J., Garrison-Kimmel, S., Maller, A. H., Bullock, J. S., Rocha, M., & Hahn, O. (2014). How to zoom: Bias, contamination and lagrange volumes in multimass cosmological simulations. *Monthly Notices of the Royal Astronomical Society*, *437*(2), 1894–1908.

Power, C., Navarro, J. F., Jenkins, A., Frenk, C. S., White, S. D., Springel, V., Stadel, J., & Quinn, T. (2003). The inner structure of Λcdm haloes—i. a numerical convergence study. *Monthly Notices of the Royal Astronomical Society*, *338*(1), 14–34.

Revaz, Y., & Jablonka, P. (2018). Pushing back the limits: Detailed properties of dwarf galaxies in a Λcdm universe. *Astronomy & Astrophysics*, *616*, A96.

Revaz, Y., Jablonka, P., Sawala, T., Hill, V., Letarte, B., Irwin, M., Battaglia, G., Helmi, A., Shetrone, M. D., Tolstoy, E., et al. (2009). The dynamical and chemical evolution of dwarf spheroidal galaxies. *Astronomy & Astrophysics*, *501*(1), 189–206.

Ricotti, M., & Gnedin, N. Y. (2005). Formation histories of dwarf galaxies in the local group. *The Astrophysical Journal*, *629*(1), 259.

Rodriguez-Gomez, V., Genel, S., Vogelsberger, M., Sijacki, D., Pillepich, A., Sales, L. V., Torrey, P., Snyder, G., Nelson, D., Springel, V., et al. (2015). The merger rate of galaxies in the illustris simulation: A comparison with observations and semi-empirical models. *Monthly Notices of the Royal Astronomical Society*, *449*(1), 49–64.

Romano, D. (2022). The evolution of cno elements in galaxies. *The Astronomy and Astrophysics Review*, *30*(1), 7.

Schaller, M., Borrow, J., Draper, P. W., Ivkovic, M., McAlpine, S., Vandenbroucke, B., Bahé, Y., Chaikin, E., Chalk, A. B., Chan, T. K., et al. (2023). Swift: A modern highly-parallel gravity and smoothed particle hydrodynamics solver for astrophysical and cosmological applications. *arXiv preprint arXiv:2305.13380*.

Schaller, M., Gonnet, P., Chalk, A. B., & Draper, P. W. (2016). Swift: Using task-based parallelism, fully asynchronous communication, and graph partition-based domain decomposition for strong scaling on more than 100,000 cores. *Proceedings of the platform for advanced scientific computing conference*, 1–10.

Schulze, F., Remus, R.-S., Dolag, K., Burkert, A., Emsellem, E., & van de Ven, G. (2018). Kinematics of simulated galaxies–i. connecting dynamical and morphological properties of early-type galaxies at different redshifts. *Monthly Notices of the Royal Astronomical Society*, *480*(4), 4636–4658.

Sérsic, J. (1963). Influence of the atmospheric and instrumental dispersion on the brightness distribution in a galaxy. *Boletin de la Asociacion Argentina de Astronomia La Plata Argentina*, *6*, 41–43.

Sparre, M., & Springel, V. (2016). Zooming in on major mergers: Dense, starbursting gas in cosmological simulations. *Monthly Notices of the Royal Astronomical Society*, *462*(3), 2418–2430.

Springel, V. (2005). The cosmological simulation code gadget-2. *Monthly notices of the royal astronomical society*, *364*(4), 1105–1134.

Springel, V., White, S. D., Jenkins, A., Frenk, C. S., Yoshida, N., Gao, L., Navarro, J., Thacker, R., Croton, D., Helly, J., et al. (2005). Simulations of the formation, evolution and clustering of galaxies and quasars. *nature*, *435*(7042), 629–636.

Tolstoy, E., Hill, V., & Tosi, M. (2009). Star-formation histories, abundances, and kinematics of dwarf galaxies in the local group. *Annual Review of Astronomy and Astrophysics*, *47*, 371–425.

Tonelli, L. (1928). Su un problema di abel. *Mathematische Annalen*, *99*(1), 183–199.

Tsatsi, A., Lyubenova, M., van de Ven, G., Chang, J., Aguerri, J. A. L., Falcón-Barroso, J., & Macciò, A. V. (2017). Califa reveals prolate rotation in massive early-type galaxies: A polar galaxy merger origin? *Astronomy & Astrophysics*, *606*, A62.

Vika, M., Vulcani, B., Bamford, S. P., Häußler, B., & Rojas, A. L. (2015). Megamorph: Classifying galaxy morphology using multi-wavelength sérsic profile fits. *Astronomy & Astrophysics*, *577*, A97.

Vogelsberger, M., Genel, S., Sijacki, D., Torrey, P., Springel, V., & Hernquist, L. (2013). A model for cosmological simulations of galaxy formation physics. *Monthly Notices of the Royal Astronomical Society*, *436*(4), 3031–3067.

Vogelsberger, M., Genel, S., Springel, V., Torrey, P., Sijacki, D., Xu, D., Snyder, G., Nelson, D., & Hernquist, L. (2014). Introducing the illustris project: Simulating the coevolution of dark and visible matter in the universe. *Monthly Notices of the Royal Astronomical Society*, *444*(2), 1518–1547.

Vogelsberger, M., Marinacci, F., Torrey, P., & Puchwein, E. (2020). Cosmological simulations of galaxy formation. *Nature Reviews Physics*, *2*(1), 42–66.

Wang, W., Zhu, L., Li, Z., Chen, Y., Han, J., He, F., Yang, X., Jing, Y., Frenk, C., Nie, J., et al. (2022). Is the core-cusp problem a matter of perspective? jeans anisotropic modeling against numerical simulations. *The Astrophysical Journal*, *941*(2), 108.

Watkins, L. L., van de Ven, G., den Brok, M., & van den Bosch, R. C. (2013). Discrete dynamical models of ω centauri. *Monthly Notices of the Royal Astronomical Society*, *436*(3), 2598–2615.

Wetzel, A. R., Deason, A. J., & Garrison-Kimmel, S. (2015). Satellite dwarf galaxies in a hierarchical universe: Infall histories, group preprocessing, and reionization. *The Astrophysical Journal*, *807*(1), 49.

Wolf, J., Martinez, G. D., Bullock, J. S., Kaplinghat, M., Geha, M., Munoz, R. R., Simon, J. D., & Avedo, F. F. (2010). Accurate masses for dispersion-supported galaxies. *Monthly Notices of the Royal Astronomical Society*, *406*(2), 1220–1237.

Zahid, H. J., & Geller, M. J. (2017). Velocity dispersion, size, sérsic index, and dn4000: The scaling of stellar mass with dynamical mass for quiescent galaxies. *The Astrophysical Journal*, *841*(1), 32.

Zhang, H., Primack, J. R., Faber, S., Koo, D. C., Dekel, A., Chen, Z., Ceverino, D., Chang, Y.-Y., Fang, J. J., Guo, Y., et al. (2019). The evolution of galaxy shapes in candels: From prolate to discy. *Monthly Notices of the Royal Astronomical Society*, *484*(4), 5170–5191.

Zhang, T., Liao, S., Li, M., & Gao, L. (2019). The optimal gravitational softening length for cosmological N-body simulations. *Monthly Notices of the Royal Astronomical Society*, *487*(1), 1227–1232.

Zhang, W., Li, C., Kauffmann, G., Zou, H., Catinella, B., Shen, S., Guo, Q., & Chang, R. (2009). Estimating the h i gas fractions of galaxies in the local universe. *Monthly Notices of the Royal Astronomical Society*, *397*(3), 1243–1253.